NMR AND DFT STUDY OF TETRAHEDRITE THERMOELECTRIC COMPOUNDS

A Dissertation

by

NADER GHASSEMI

Submitted to the Office of Graduate and Professional Studies of
Texas A&M University
in partial fulfillment of the requirements for the degree of

DOCTOR OF PHILOSOPHY

Chair of Committee,	Joseph H. Ross, Jr.
Committee Members,	Donald G. Naugle
	Artem G. Abanov
	Xiaofeng Qian
Head of Department,	Grigory Rogachev

December 2020

Major Subject: Physics

ABSTRACT

Thermoelectric (TE) materials offer interconversion of thermal and electrical energy through the presence of a heat gradient and thus constitute an attractive option for the recovery of waste heat. Low conversion efficiency and high cost have been major limiting factors in the industrial success of TE materials, and, therefore, a race toward practical materials with enhanced physical properties has emerged to meet the increasing demands. The tetrahedrite-tennantite series is an important family of copper natural ore mineral and also one of most widespread sulfosalts on the earth. Very low lattice thermal conductivities, less than 0.5 W/m K, were observed in this system, attributed to the unique crystal structure of the tetrahedrite $Cu_{12}Sb_4S_{13}$. In these materials, half of the Cu atoms occupy four-coordinate sites Cu-I and half occupy three-coordinate sites Cu-II. Due to the an-harmonic force introduced by the Sb lone pairs, the equivalent isotropic atomic displacement parameter for the Cu-II atoms is found to be very large, an indication that the Cu-II atoms vibrate with low energy in the stiff framework. Thus, they may strongly interact with heat-carrying phonons similar to other caged TE compounds, e.g. skutterudites and clathrates.

In this work, the origin of the intrinsic low thermal conductivity and electronic behavior is investigated by both theoretical and experimental NMR studies. The effects of additional atom substitution on phase transition and magnetic properties of tetrahedrite are studied with the conclusion that electronic and magnetic characteristics of this compound are not as sensitive to impurities as is typically the case for TE materials. We use NMR technique as a flexible tool to investigate chemical structures and determine symmetries, atomic motion, along with hyperfine interactions. We also applied NMR technique to better understand the anharmonic phonon behavior of undoped $Cu_{12}Sb_4S_{13}$.

We found spin-lattice relaxation rates ($1/T_1$) are dominated by a quadrupolar process indicating anharmonic vibrational dynamics both above and below T_c. We used a quasiharmonic approximation for localized anharmonic oscillators to analyze the impact of Cu rattling. The results demonstrate that Cu-atom rattling dynamics extend unimpeded in the distorted structural configuration below Tc and provide a direct measure of the anharmonic potential well.

We further report ^{63}Cu NMR measurements for the Cu-rich phase of $Cu_{12+x}Sb_4S_{13}$($x \leq 2$) and compared to $Cu_{12}Sb_4S_{13}$. We identify the NMR signatures of phase segregation into Cu-poor ($x \approx 0$) and Cu-rich ($x \approx 2$) phases, with the metal-insulator transition observed in $Cu_{12}Sb_4S_{13}$ suppressed in the Cu-rich phase. Based on NMR T_1 and T_2 measurements, the results demonstrate Cu-ion hopping below room temperature with an activation energy of $\sim$150 meV for the Cu-rich phase, consistent with superionic behavior. The NMR results also demonstrate the effects of Cu-ion mobility in the $Cu_{12}S_4S_{13}$ phase, but with a larger activation barrier. We identify a small difference in NMR Knight shift for the metallic phase of $Cu_{12}Sb_4S_{13}$ compared to the Cu-rich phase, and when compared to density functional theory calculations, the results indicate a mix of hyperfine contributions to the metallic shift.

We carried out material characterization as well as ^{63}Cu NMR measurement of various substituted tetrahedrites including $Cu_{10.6}Zn_{0.5}Ni_{0.9}Sb_4S_{13}$, $Cu_{10}ZnNiSb_4S_{13}$, $Cu_{10}Ni_2Sb_4S_{13}$, $Cu_{10}Zn_2Sb_4S_{13}$, $Cu_{11}MnSb_4S_{13}$, $Cu_{10}Mn_2Sb_4S_{13}$, and $Cu_{12}Sb_{4-x}Te_xS_{13}$ compositions. DFT calculations were also used to model chemical shifts and explore changes in partial DOS for analyzing the results. By modeling the spectra of Zn and Ni substituted materials we found information about the changes in symmetry and electronic behavior in these materials. We observed that all substituted materials have similar chemical shift for the Cu-I site which indicates distinct behavior from undoped $Cu_{12}Sb_4S_{13}$. We discussed the results in terms of random local distortions. Lack of Knight shift for most of the substituted tetrahedrites observed which indicates the importance of native defects or generation of a pseudo gap structure.

We observed that most of the lineshapes exhibit magnetic broadening at low temperatures. Magnetic moment analysis based on the NMR lineshapes agrees with the previously proposed

local moment for Ni substitution in low concentrations. On the other hand, Ni_2 spectra analysis indicates more strongly interacting moments with a distinct electronic behavior. We also found that rattling is the main effect controlling the scattering of phonons in Zn-Ni substituted materials and this was confirmed by largest rattling behavior observed in Zn, Ni co-doped sample. Our results indicate that this is not simply tied to expansion of lattice. A lack of Cu-ionic motion was observed in all substituted materials except in $Cu_{12}Sb_3TeS_{13}$, and the MST is suppressed in almost all of the doped materials.

DEDICATION

To my mother Maral Kurhasanlou, my father Gheydarali Ghassemi.

ACKNOWLEDGMENTS

I would like to deeply thank all whom assisted me in this research project. It is my great honor and luck to work in Professor Ross lab. He was always kind and patient with me, guiding me to achieve the skills required in the field of NMR spectroscopy and teaching me experimental skills and the physics hidden behind the data. I am also very grateful to my other committee members for their insightful suggestions to improve my research.

Many thanks go to my colleagues Yefan Tian and Dr. Shayan Hemmatiyan who shared their valuable experience with me. The help from other group members Dr. Ali Sirusi Arvij, Dr. Jing-Han Chen, Emily Conant, Laziz Saribaev, Rui Li are greatly appreciated.

Last but not least, I would like to thank my parents, who believed in me and gave their unconditional love and support to me when I needed it most. I also want to thank all my friends home and abroad specially Christina Cochran, Roman Chyzh and Dustin Scriven, who encouraged me to work hard and achieve my final goal.

CONTRIBUTORS AND FUNDING SOURCES

Contributors

This work was supported by a dissertation committee consisting of Professors Joseph Ross, Donald Naugle, and Artem Abanov of the Department of Physics & Astronomy and Professor Xiaofeng Qian of the Department of Materials Science & Engineering.

The analyses depicted in Chapter X were conducted in part by Yefan Tian of the Department of Physics & Astronomy and were published in 2018-2020 in an articles listed in the ACS Appl. Mater. Interfaces, J. Phys. Chem, and Phys. Rev. B.

All other work conducted for the dissertation was completed by the student independently.

Funding Sources

Graduate study was supported by a fellowship from Texas A&M University and a dissertation research grant from the Robert A. Welch Foundation.

NOMENCLATURE

NMR	Nuclear Magnetic Resonance
TE	Thermoelectric
MST	Metal Semiconductor Transition
MIT	Metal Insulator Transition
FFT	Fast Fourier Transform
DFT	Density Functional Theory
PBE	Perdew-Burke-Ernzerhof
APW	Augmented Plane Wave
NQR	Nuclear Quadrupole Resonance
EFG	Electric Field Gradient
H_{CS}	Chemical Shift Hamiltonian
H_Z	Zeeman Hamiltonian
H_Q	Quadrupole Hamiltonian
PGEC	Phonon Glass Electron Crystal
PAS	Principal Axis System
XRD	X-Ray Diffraction
Rw	Residual work
WDS	Wavelength Dispersive Spectroscopy
CVD	Chemical Vapor Deposition
H_D	Dipole Hamiltonian
K	Knight Shift

TABLE OF CONTENTS

Page

LIST OF FIGURES

FIGURE Page

LIST OF TABLES

TABLE Page

1. INTRODUCTION

1.1 Thermoelectric Generators

Based on the Energy Information Administration of the Department of Energy (DOE), the total yearly energy world electric power production in 2008 was around 2×10000TWh. This number is predicated to be raised to around 3×10000 TWh by 2030. From this global energy consumption, the U.S. forecasted to use about 5300 TWh. We are depending on fossil fuel for a majority of the energy consumption and the demand is still rising rapidly. On the other hand, the unbalanced distribution of resources geographically centralizes energy supplies in a very low number of regions, some of them politically unstable. Moreover, ejection of greenhouse gases from burning fossil fuels has been a severe problem for decades. In exchange, the climate change has been exacerbated due to our growing fuel utilization. Therefore, the demand for an alternative source of energy is a necessity. Demand for clean and renewable energy sources is increasing everyday. We need a new source of energy that can be obtained cheaply. To solve this problem, there have been several proposals. In some specific areas, wind as well as hydropower as a source of power has been put into great use. Even though nuclear energy has always been suggested as a future source of energy and achieved so much, the few catastrophes resulted in public concern with this form of energy resource. On the other hand, significant efforts need to be made to develop renewable energy technologies. Solar energy has the ultimate potential of providing $120\,000$ TW globally. The solar radiation intercepted in an hour by the earth, therefore, equals to the world power needs for a year. In practice, however, perhaps as much as 600 TW of solar energy can be converted to electricity. This leads us to look for new methods to convert heat to electric form of energy.

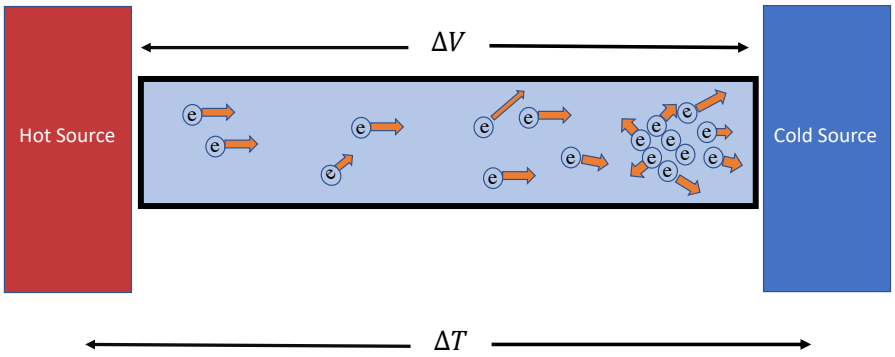

Figure 1.1: Sketch demonstrating the underlying principle of the Seebeck effect. The temperature gradient across the TE material causes charge carriers on the warm side to move with higher velocities in average.

The thermoelectric effect is based on the Seebeck effect discovered by Thomas Seebeck[11] in 1823 and its reverse effect (by Jean C. A Peltier) in 1834 [12]. As schematically shown in figure 1.1, the Seebeck effect can generate electricity through a temperature gradient and thus has the potential use for waste heat recovery and power generation. This potential difference can be written in the following form:

$$\Delta V = S\Delta T \tag{1.1}$$

where S is the Seebeck coefficient. Normally, this Seebeck coefficient is a positive (negative) number in materials with hole (electron) charge carriers. For instance, in the p-type semiconductors, the Seebeck coefficient is a positive number since holes are the primary carriers.

When discussing TE behavior of materials, it is often convenient to refer to the product of Z (figure of merit) and T since the material properties that comprise Z are temperature dependent. The efficiency of thermoelectric materials is normally parametrized by the figure of merit, ZT, defined as:

$$ZT = \frac{S^2\sigma T}{\kappa} \tag{1.2}$$

where σ is the electrical conductivity, and κ the thermal conductivity. The thermal conductivity is $\kappa = \kappa_{ph} + \kappa_{el}$, where κ_{ph} and κ_{el} are the phonon and electron contributions, respectively. In addition, ZT is explicitly used in the calculation of a material's thermoelectric conversion efficiency (η) as shown as follows.

The efficiency of a TE material is defined by the ratio $\eta = \frac{W}{Q_H}$, where W is the work delivered to the external load and Q_H is the heat (Both measured in J) leaving the hot junction (source) toward the cold junction (sink) [13]. And this can be defined [14] with $W = R_L I^2 = \frac{S^2 \Delta T^2 R_L}{(R+R_L)^2}$ and $Q_H = \kappa \Delta T + S T_H I + \frac{I^2 R}{2}$ as,

$$\eta = \frac{W}{Q_H} = \frac{\Delta T}{T_H} \frac{\sqrt{1+ZT}-1}{\sqrt{1+ZT}+T_C/T_H}. \tag{1.3}$$

In the above equations, T_H is the hot-side temperature, T_C is the cold-side temperature and R_L is the external load resistance. It is immediately apparent that η will rise as the temperature difference ΔT rises. Additionally, note that the first term is the Carnot [15] efficiency ($\eta_c = \frac{\Delta T}{T} = \frac{(T_H - T_C)}{T_H}$) which describes the maximum theoretical efficiency of a heat engine. In application, thermoelectric materials can be used as thermoelectric generators and refrigerators. They require both n- and p-type semiconductors.

1.1.1 Transport Theory of Thermoelectrics

When the system is at equilibrium, there is no transport of charge or energy in the distribution function f. The distribution function $f(\vec{r}, \vec{k}, t)$ describes the probability of a particle with wave vector $\vec{k}$ to be at position $\vec{r}$ at a given time t. Therefore, if $f(k)$ is symmetric in k space given that there are equivalent amounts of carriers with momentum that are equal but opposite, the current becomes zero. If there is an external force $\vec{F} = \hbar d\vec{k}/dt$ acting on the particle (assumed be an electron) the total change in the distribution function will be given by

$$\frac{df}{dt} = \frac{\partial f}{\partial t} + \frac{1}{\hbar}\vec{F} \cdot \vec{\nabla}_{\vec{k}} f + \vec{v} \cdot \vec{\nabla} f. \tag{1.4}$$

In the case that f is at a local equilibrium due to the collision, normally the relaxation by collisions occurs at a rate proportional to the derivative of the distribution function. The time constant to reach equilibrium is termed the relaxation time τ, and is defined by the following equation:

$$\frac{df}{dt}|_{collision} = -\frac{f - f_0}{\tau} \tag{1.5}$$

where f_0 is the equilibrium distribution function. If we assume that the difference between f and f_0 is small, then f can be replaced by f_0. In the time-independent case we have

$$f = f_0 - \frac{\tau}{\hbar}\vec{F} \cdot \vec{\nabla}_{\vec{k}} f_0 - \tau \vec{v} \cdot \vec{\nabla} f_0. \tag{1.6}$$

If there are thermal gradients, we can always break down the space derivatives as:

$$\frac{\partial f_0}{\partial x} = \frac{\partial f_0}{\partial T}\frac{\partial T}{\partial x} \tag{1.7}$$

Given equation (1.7), reconfiguring equation (1.6) by considering electrical field $\vec{E}$ will give

$$f = f_0 + \tau e|\vec{E}|v_x \frac{\partial f_0}{\partial \varepsilon} - \tau v_x \frac{\partial f_0}{\partial x} \tag{1.8}$$

Now, we will compute various electric transport quantities using the above equations.

1.1.1.1 Seebeck effect

In a system with the distribution function $f(\varepsilon)$ the current density associated with charge carriers is given by

$$\vec{J} = -e \int N(\varepsilon)\vec{v} f(\varepsilon) d\varepsilon. \tag{1.9}$$

By inserting the distribution function (1.9) component along the x-axis in the expression for the current density and setting $N(\varepsilon)$ equal to $V/8\pi^3$, where V is the volume of the crystal, we find

$$J_x = \frac{ne}{m_e}\Big(\big[eE_x + T\frac{d}{dT}\big(\frac{\varepsilon_F}{T}\big)\frac{dT}{dx}\big]\langle\tau\rangle + \frac{1}{T}\frac{dT}{dx}\langle\varepsilon\tau\rangle \Big). \tag{1.10}$$

If we consider the case that no electric current flows, that is where Eq. (1.10) is set to zero, then we will have an electric field established in the material as a result of the thermal gradient,[16]

$$E_x = T\frac{d}{dT}\Big[\frac{\langle\tau\varepsilon\rangle}{eT\langle\tau\rangle} - \big(\frac{\varepsilon_F}{eT}\big)\Big]\frac{dT}{dx} = -S\frac{dT}{dx}. \tag{1.11}$$

The Seebeck coefficient, S, is defined in Eq. (1.11) as

$$S = -\frac{dV_x}{dT}, \tag{1.12}$$

where V_x is the potential developed by the electric field E_x along the sample distance dx as a result of the thermal gradient dT. Formally, the Seebeck coefficient may be expressed as

$$S = -\frac{T}{e}\frac{d}{dT}\Big[\frac{\langle\tau\varepsilon\rangle}{T\langle\tau\rangle} - \frac{\varepsilon_F}{T}\Big]. \tag{1.13}$$

The first term is the kinetic energy term and normally for doped semiconductors, the Fermi energy is much larger than the kinetic energy for the electrons, so the second term of Eq. (1.13) will dominate the Seebeck coefficient. The Seebeck quantity can also be connected to a coefficient often explained as the thermoelectric power with notation P,

$$S = T\frac{dP}{dT}. \tag{1.14}$$

Therefore, for P we find

$$P = \frac{\varepsilon_F\langle\tau\rangle - \langle\tau\varepsilon\rangle}{eT\langle\tau\rangle} = \frac{1}{k_BT}\Big[\varepsilon_F + \frac{\langle\tau\varepsilon\rangle}{\langle\tau\rangle}\Big]. \tag{1.15}$$

The momentum relaxation time τ_e is frequently of the form $\tau_e = A\varepsilon^{-s}$, therefore

$$\varepsilon_F\langle\tau_e\rangle/\langle\tau\rangle = (5/2 - s)k_BT, \tag{1.16}$$

giving,

$$P = -\frac{k_B}{e}\Big[(5/2 - s) - \frac{\varepsilon_F}{k_B T}\Big]. \tag{1.17}$$

1.1.1.2 Electric Conductivity

Considering the Fermi-Dirac distribution for electrons in the conduction band, the electric conductivity for parabolic band can be given by [17]

$$\sigma = 2\frac{8\sqrt{2m^\star}\pi e^2}{3h^3}\int_0^\infty \frac{df(E)}{dE}\sqrt{E^3}\tau(E)dE \tag{1.18}$$

where $f(E)$ is Fermi-Dirac function and $m^\star$ is the effective mass. Charge carriers that are thermally activated will be excited across the energy gap in semiconductors. In the case that this dimmates the conductivity could simplify to

$$\sigma \simeq \sigma_0 e^{\frac{-E_g}{2k_B T}}, \tag{1.19}$$

where k_B is the Boltzmann constant and E_g is the energy of the gap in semiconductors. On the other hand, the $\sigma_0 = \frac{ne^2\tau}{m^\star}$ describes that electric transport depends on charge carriers density n and $\frac{e\tau}{m^\star}$ which is considered to be charge mobility. In a number of semiconductors for which their structures are disordered, the conductivity mechanism is variable range hopping at low temperatures. This type of semiconductor contains charge carrier states for which the conduction takes place when the charge carriers hop within these states. For this hopping the conductivity [18] is described by $\sigma \approx \sigma_0 e^{-(T_0/T)^{\frac{1}{4}}}$. The characteristic temperature T_0 is proportional to DOS ($g(E)$) and localization radius r_L as

$$T_0 = \frac{17.6}{k_B g(E_f) r_L^3}. \tag{1.20}$$

1.1.1.3 Thermal Conductivity

The overall thermal conductivity has two contributions, that of phonons and that of electron transport. Therefore it can be divided into two parts: the phonon thermal conductivity and the electronic thermal conductivity:

$$\kappa_{total} = \kappa_{ph} + \kappa_{el}. \tag{1.21}$$

For most metallic materials, the electronic thermal conductivity contribution is much higher than the lattice contribution. The electronic part of equation (1.21) often embodies the Wiedemann-Franz law which states that the ratio of the thermal conductivity to the electrical conductivity is the same for all metals, at any given temperature:

$$\frac{\kappa_e}{\sigma T} = \frac{\pi^2}{3}\left(\frac{k_B}{e}\right)^2 \tag{1.22}$$

where the ratio $\frac{\pi^2}{3}\left(\frac{k_B}{e}\right)^2$ stands for the Lorenz number, L.

The phonon contribution to the thermal conductivity κ_{ph}, involves the lattice vibrational modes in crystals. It relies on the crystal structure, pattern of elements and bond strength among atoms. In contemporary quantum theory, the vibrational modes could be regarded as quasi-particles-phonons that contain quantized pockets of energy [19]. The most general form of the Debye lattice conductivity is presented by

$$\kappa_{ph} = \frac{1}{2\pi^2\nu}\int_0^{\omega_{max}} \hbar\omega^3\tau(\omega)\frac{(\frac{\hbar\omega}{k_BT^2})e^{\frac{\hbar\omega}{k_BT}}}{(1-e^{\frac{\hbar\omega}{k_BT}})^2}d\omega \tag{1.23}$$

where τ is the phonon's average scattering time, ω_{max} is the phonons maximum angular frequency and ν is the phonon's velocity where Debye's model proposes $\nu = \frac{\omega}{k}$ (k is the wave vector).

1.1.1.4 The phonon scattering time

The phonon scattering time is a sum over contributions from all of the phonon scattering mechanisms. For most materials in insulating or semiconductors states, the phonon-phonon scattering

dominates. Also, acoustic phonons contribute significantly in heat transfer due to their larger velocities. For phonon-phonon scattering, one must consider two scattering processes. At very low temperatures, where the Debye model fits well, only phonons with short wave vector are available. In this temperature range, the collisions of two phonons will produce a third phonon with its momentum still in the first Brillouin zone. This process in which the momentum of phonons after scattering is conserved, is called the N-process. This mechanism just alters the phonon's momentum distribution and does not affect the heat transfer. Hence, this process has no effect on the thermal current.

At temperatures close to or above the Debye temperature, the number of phonons with large wave vector near the border of the first Brillouin zone grows. Therefore, it is more likely that the collisions between them give rise to a third phonon with wave vector out of first Brillouin zone. This mechanism in which the phonon's momentum after scattering is not conserved, resulting in a divergence in the direction of phonon momentum is called an Umklapp process. The scattering rate for this process is given by [20]

$$\tau(x) = \frac{M\nu^2\hbar\theta_D}{(\gamma k_B x)^2 T^3} e^{\frac{\theta_D}{3T}} \tag{1.24}$$

where M is the average mass of atoms, γ is the Gruneisen parameter (measure of anharmonicity of lattice vibrations), $x = \hbar\omega/k_B T$ and ω is phonon frequency, and θ_D Debye temperature.

The scattering relaxation rate for phonon-impurity scattering is given by

$$\tau(x) = \frac{4\pi\hbar^4 v^3}{(k_B x T)^4 \Gamma V} \tag{1.25}$$

where V is the average volume per atom and Γ is the defect scattering parameter.

1.2 Approaches to enhance ZT in bulk materials

Beginning in the 1990s a renewed approach to TE materials began after the several decades of slowdown in the research. The new studies opened various strategies to enhance ZT.

One of the commonly accepted methods to enhance figure of merit is to reduce the lattice ther-

mal conductivity. In order to do this, three general methods are mainly implemented to decrease κ. The first adopted method is scattering phonons. Reduction in thermal conductivity is obtained by scattering phonons in diverse frequency ranges using a variety of means namely mass fluctuation scattering (a combined crystal in ternary and quaternary doped materials), grain boundary scattering due to the volume of the grains and interface scattering in thin films or multilayer systems.

As a general rule of thumb, a good TE material [21] is a semiconductor with $6k_BT \leq E_g \leq 9k_BT$ where the lattice thermal conductivity is reduced, while the mobility of carriers are large.There are two primary methods to enhance the ZT in thermoelectric materials based on aforementioned transport theory which are described in the next sections.

1.2.1 Band structure engineering to improve power factor

For the Seebeck coefficient , the first typical example is the density-of-states (DOS) distortion through Tl doping in PbTe [22]. This enhancement occurs when the valence or conduction band of the host semiconductor resonates with the localized impurity energy level. Tl doped PbTe, in contrast with Na doped PbTe with the same carrier concentration, shows larger effective mass and is considered to have the greater Seebeck coefficient. Deforming the DOS leads to ZT as large as 1.5 at around 750 K, which is a notable improvement by merely adding Tl to PbTe. Combination of this principle with the methods used to reduce the thermal conductivity could further improve ZT in the PbTe system, and have been established to be equally applicable in other TE systems, in particular Al-doped PbSe [23].

Another well understood example is the improvement of the Seebeck coefficient by adjusting the energy offsets between heavy and light valence bands in PbTe. PbTe has a interesting valence band; in this band structure, there is a valence band (with a heavy effective the mass, thus called heavy hole band) at Σ which lies energetically below the upper light hole band at the L point, as illustrated in figure 1.2. The energy distance between L and Σ band edges is around 0.15 eV. If the Σ and L bands shift closer in energy, then it is predictable that the carriers redistribute between these two valence bands with different effect masses.

The net effective mass can be raised by injecting carriers from the Σ band to L band edges

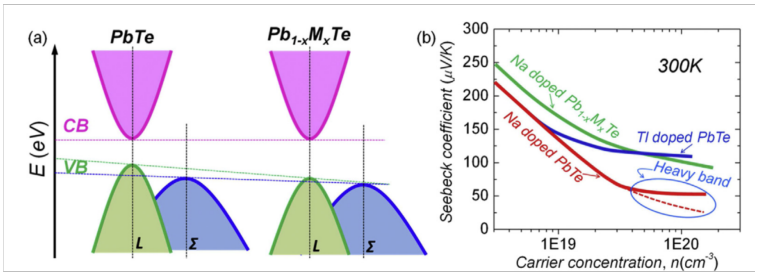

Figure 1.2: a) Diagram demonstrating the relative energy of the valence bands in PbTe system, with rising solid solution fraction M. Solid solution alloying within the solubility limit modifies the valence band structure pushing both L and Σ bands down but make the two valence bands closer in energy. b) The improvement on Seebeck coefficient at a similar Hall carrier concentration in PbTe is because of resonant doping (Tl) or band convergence at room temperature. Reprinted with permission from [1].

with a factor of $N_\nu^{2/3}$, where N_ν is the total number of degenerate valleys, which is 4 for L band and 12 for the Σ bands. Namely, $m^\star = N_\nu^{2/3} m_b^\star$, where $m_b^\star$ is the effective mass [24] just for one valley. Alloying could also lead to diminishing the energy gap between Σ and L bands. Several studies, for instance show that Mg[25] added to PbTe decreases the gap between L and Σ as the alloying fraction increases. Enhancing the doping fraction lowers both L and Σ bands, however, the L band reduces faster than Σ, so that eventually they get closer figure (1.2 .a). This form of Mg solution doping boosts the Seebeck coefficients in the entire carrier concentrations, figure (1.2(b)). The Seebeck coefficient improvement is comparable in nature to that produced by resonant states in PbTe by Tl doping. In fact, Mg and Mn doping into PbTe have generated a high ZT of around 2.0 at 873 K and 1.6 at around 700 K, respectively. Nevertheless, this method is challenged by the reduction of carrier mobility, clearly this needs to be settled with future experimentation. The band engineering outlined above has also been successfully employed to other compositions such as the PbSe-SrSe [26], Mg_2Si-Mg_2Sn [27].

1.2.2 Thermal conductivity reduction to improve the PF

In practice, a more simple and straightforward way to enhance the figure of merit is reducing the lattice thermal conductivity, which is primarily independent of the electrical features. A stan-

dard method to reduce the lattice thermal conductivity is developing a bulk solid solution, which is generated by combining two compounds with identical crystal structure. This method can generate point defects in a binary mixture without altering the crystal structure. This process will explicitly increase the phonon-defect scattering as described in equation (1.25). The solid solution technique normally reduces the lattice contribution of thermal conductivity κ_{ph} more than the κ_{el}, as mentioned in [28]. As examples, $Bi_{2-x}Sb_xTe_3$ is a decent solid solution convenient at low range temperature [29] application and $Si_{1-x}Ge_x$ is another solid solution suitable at high range temperature applications.

Slack suggested a new approach for finding better TE in which cage compounds with an enlarged unit cells containing encapsulated atoms that could "rattle" inside the voids and will have a small thermal conductivity [30]. In comparison to the solid solution approach, these foreign atoms occupy vacant interstitial sites of compound, instead of replacing atoms in host compound structure. The benefit of this method stems from the reality that these rattling elements will successfully scatter phonons without impacting the transport characteristics controlled by the host compound structure. The skutterudites [31, 32] are excellent illustrations of the rattling behavior in TE materials. Adding extra rare earth elements into the vacant sites of $CoSb_3$ or $CoAs_3$ will reduce their lattice thermal conductivity by more than one order of magnitude. The reduced lattice thermal conductivity makes partial/fully filled skutterudites amongst the finest of both n and p-type TE power generator materials [33].

A familiar circumstance for applying TE power generator technology is when power is generated in automobiles by extracting heat from the exhaust. [34] High efficiency demands a high-power factor ($P = \sigma S^2$) and low thermal conductivity. Hence, several ideas for scattering the phonons and decreasing total thermal conductivity κ_{tot} which have been proposed. Nano-inclusions and nano-structuring can produce ZT of 1.4-1.8 at 750-900K [35, 36, 37, 38, 39] in BiSbTe and Nb-doped $SrTiO_3$ and with adding mesoscale grain boundaries ZT =2.2 K at 915 K has been achieved [40]. Other methods are engineering band convergence [41] and strong electron phonon coupling by charge density waves [42].

Thermoelectric compounds containing copper normally act as a p-type semiconductor and some of them can be considered as good candidates for thermoelectric applications due to their high ZT. For instance, some ionic conductors such as Cu_2Se and Cu_2S illustrate high figures of merit [43, 44]. Lately, some other trigonal copper compounds like $Cu_3SbSe_{4-x}S_x$ solid solutions [45] and Cu_2SnSe_3 [46, 47] have been shown to have ZT values around unity.

Tetrahedrites are copper thermoelectric compounds with chemical structure of $Cu_{12}Sb_4S_{13}$, and will be thoroughly discussed in the next chapter.

2. TETRAHEDRITE THERMOELECTRIC MATERIALS

State-of-the-art TE materials usually contain environmentally harmful atoms, such as Pb, or elements that exist in low abundance on earth, such as Te [48]. Therefore, compounds containing nontoxic and earth-abundant components are worthy of exploration. These compounds are compliant to large-scale utilization due to their environment-friendly and inexpensive features. Tetrahedrite materials, of nominal structure $Cu_{12}Sb_4S_{13}$, are a group of compounds that satisfy these requirements. Tetrahedrite appears naturally as a considerably abundant mineral throughout the world and is a normal byproduct of the Cu and Ag mining industry [49]. Moreover, the tetrahedrite group of TE materials show a remarkably low thermal conductivity, while exhibiting a decent electrical conductivity and thermopower [50]. In conclusion, these TE materials consistently show a ZT close to unity [51] at temperatures around 700 K. Tetrahedrites are excellent compounds for TE applications at high temperatures due to their low toxicity and high earth abundance, yet illustrating good TE characteristics for intermediate-temperature utilizations.

Tetrahedrites (tennantites) are copper compounds in which chemical structure is $Cu_{12-x}\beta_xSb(As)_4S_{13}$, where β could be a transition metal element such as Zn, Mn, and Ni [52] or other metals such as Mg[53]. The tetrahedrite-tennantite (As bearing) series is an important family of copper natural ore minerals and also one of most widespread sulfosalts on the earth. They are able to incorporate various elements on different sites. For instance, Zn, Ni, Mn, Fe, or Co will reside on the copper sites and other atoms such as, Te, As, and Bi on the antimony (Sb) site [54, 55], and finally Se on the sulfur site [56, 57, 58], which allows one by control of chemical compositions to tune its electronic structure. In general, these materials show on the one hand intrinsic low lattice thermal conductivity and on the other hand adjustable electronic transport properties which make them good candidates for thermoelectric power generation.

2.1 Basic Properties

The following subsections will highlight the crystal structure and physical characteristics that control the main properties of tetrahedrite. Hereafter, "pure tetrahedrite" will be used in reference to $Cu_{12}Sb_4S_{13}$.

Early studies focused on the crystal structure of $Cu_{12}Sb_4S_{13}$ based materials. The primitive unit cell's volume is $1.1\ nm^3$ and it contains 29 atoms. This structure is similar to Zintl antimonides with comparable κ. As mentioned in last subsection, the structure is cubic with space group 217. As shown in figure (2.1) , there are two different copper sites in the lattice. half of the twelve Cu atoms are placed on tetrahedral 12d Cu-I sites and the other six Cu atoms are distributed in trigonal planar 12e Cu-II sites. Four of the six Cu-II sites are believed to be occupied by monovalent Cu and the remaining two are nominally filled by Cu^{2+} ions, while the Cu-I sites are filled only by monovalent Cu atoms. Furthermore, two distinct sites are identified for sulfur atoms; the S-I site, tetrahedrally coordinated by two other Cu-I and one antimony, and the S-II site which is connected to six other Cu-II atoms. Eventually, Sb is joined to three other S-I sites.

2.2 Crystal Structure

The complex crystal structure of tetrahedrite contributes to its favorable thermoelectric characteristic. $Cu_{12}Sb_4S_{13}$ crystalizes in a cubic structure with space group 217 ($\bar{I}43m$) as shown in figure 2.1.

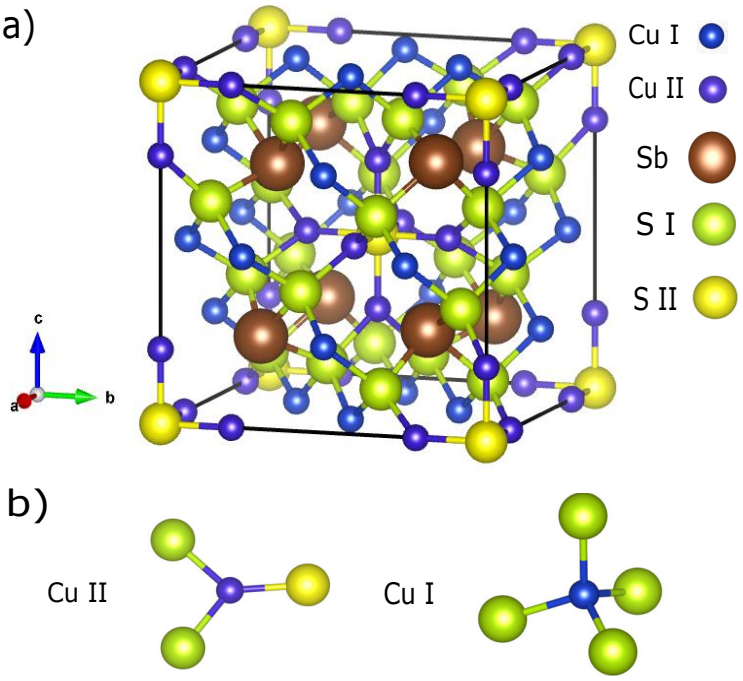

Figure 2.1: (a) Room-temperature crystal structure of $Cu_{12}Sb_4S_{13}$. (b) Cu-I at the 12d crystallographic site shown tetrahedrally coordinated by S-I and Cu-II at 12e is trigonally coordinated by two S-I and one S-II. Reprinted with permission from [2].

As illustrated, there are two unique Cu sites (12d and 12e), one Sb site (8c), and two S sites (24g and 2a) [4] Every Cu12d (also named Cu-I) atom is coordinated tetrahedrally to four S-24g atoms; whereas, each Cu12e (Cu-II) atom is trigonally connected to two S-24g atoms and one S2a atom with total 58 atoms per unit cell. In the trigonal coordination, the Cu12e atom is sandwiched between two Sb atoms such that the Sb lone pairs are oriented towards the Cu12e atom; this bonding effectively yields a trigonal bipyramidal arrangement for the Cu12e atom with two Sb atoms on the axial sites. Every S-24g is tetrahedrally coordinated to two Cu12d atoms, one Cu12e atom, and one Sb atom. However, each S2a atom is in an octahedral coordination with six Cu12e atoms. Finally, each Sb atom is tetrahedrally coordinated with three S-24g atoms and a protruding lone pair, such that the Sb lone pair creates a void-like pocket in the structure leading the crystal structure of tetrahedrite becomes fully complex and shows an array of distinct atomic bonds.

A $Cu_{12}Sb_4S_{13}$ crystal in formula unit (f.u.) has a molar mass of $1666.45\ \ gram\ \ mole^{-1}$, and its

unit cell (u.c.) has a lattice constant of $a = 10.3908\,\text{Å}$, accordingly, the volume could be derived $V = 1.12 \times 10^{-27} m^3$ [59]

By increasing N, the part of the specific heat due to the acoustic phonon modes will decrease (since $C_v = C_v/N$), while the optical phonon modes will not impact the heat transfer (to first order, because these mode's group velocities are very small). Hence, we can estimate the total specific heat at by using the Dulong-Petit equation $C_v = 3nk_B$, where n is the density of atoms in unit cell and k_B is the Boltzmann constant. On the other hand, according to Eq. (1.2), high ZT requires high electrical conductivity as well as low lattice thermal conductivity. Therefore, the materials need to behave with respect to electrons as a good crystal and respect to phonons as a glassy or disordered material. This is what led Slack [60] to come up with "phonon-glass, electron-crystal" or PGEC idea in 1995. In most phonon-glass compounds, the phonon mean free path λ can be replaced by the interatomic distance d and the minimum of the lattice thermal conductivity κ_L, could be formulated [61] by using:

$$\kappa_L = \frac{1}{3}\nu\lambda C_v \tag{2.1}$$

where, ν is the phonon group velocity. Therefore, the minimum lattice thermal conductivity κ_L will be

$$\kappa_{L,min} = \nu\lambda n k_B. \tag{2.2}$$

As mentioned, n is the density of conventional unit cells ($n = \frac{N}{V}$), this implies that as the primitive unit cell volume becomes larger, the lattice thermal conductivity becomes smaller which explains why thermal conductivity is small in these materials.

Having a large primitive unit cell is thus one of the reasons for such an intrinsic low thermal conductivity. In PGEC materials, lattice vibrations of a specific crystal structure also give rise to phonon-phonon interactions which scatter the energy carrying acoustic phonons. Some of these materials, including tetrahedrites, have extremely low lattice thermal conductivity regardless of

alloying them with other elements and/or nano structuring them. Other reasons are the rattling effect and anharmonicity.

2.3 Lattice Dynamics

Cu-based tetrahedrites are preferable as a power generation material, specifically because of their exceptionally low lattice thermal conductivity, which reaches the lowest possible value predicted by theory [62]. This is in part due to the large size of the primitive unit cell volume in the $Cu_{12}Sb_4S_{13}$, which reduces κ_L, and the vast arrays of atoms inside the primitive unit cell produces further optical phonon modes [63]. Figure (2.2) presents the calculated phonon dispersion of $Cu_{12}Sb_4S_{13}$ [3]. The three harmonically unstable vibrational optical phonon branches at the boundaries are connected to the out-of-plane motions of Cu atoms at 12e sites. Large lattice anharmonicity and rattler-like motion of the Cu12e atoms give rise to strong phonon-phonon scattering. This will be explained in the next sections.

Negative (imaginary, in-fact) frequencies in a phonon dispersion calculation indicate dynamical instability. Such an instability can be brought about either from improper positioning of the atoms for the calculation or a pathway for a symmetry lowering phase transition. Those corresponding to soft modes, could be indicative of ferroelectric order. In this case, negative frequencies are believed to be due to sensitivity to displacement of Cu-II ions.

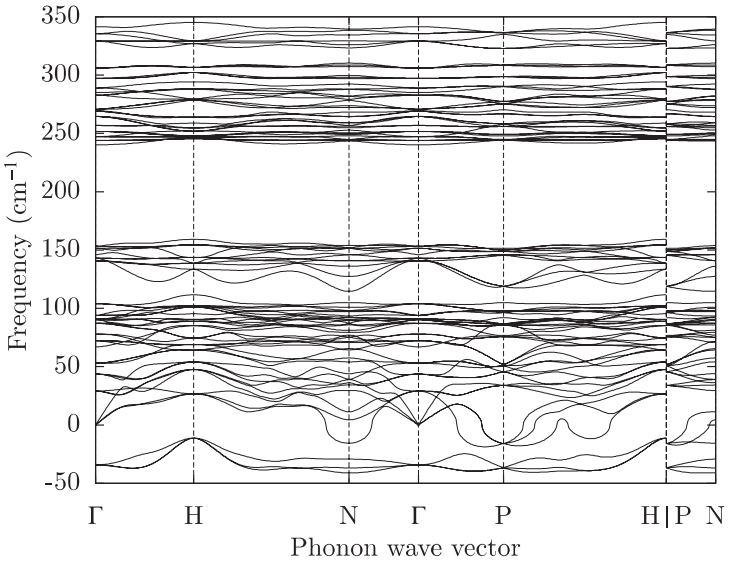

Figure 2.2: Calculated phonon dispersion for $Cu_{12}Sb_4S_{13}$ using DFT. Reprinted with permission from [3]

It is known that the dynamics of the trigonal coordinated Cu atom is a vital point of the vibrational density of states in tetrahedrites. Although the community has raised some issues concerning tetragonally connected Cu contributions and its displacement comparing the trigonally connected Cu, it has been known that trigonally connected Cu (Cu in 12e site) moves with larger displacement [64, 4, 65, 3]. Asymmetric hybridizations results in a double well potential which the Cu atom energetically favors one over the other one giving rise to slightly out of plane position. The energies of the Cu-II displacement above the trigonal plane have been inspected with experimental and computational tools [66, 5, 67, 68].

A vibrational first principle molecular dynamics calculation of constitutive elements of $Cu_{12}Sb_4S_{13}$ is exhibited in figure 2.3. The marked dashed line at around 4 meV indicate the significant vibrational mode of Cu-II (Cu12e) in the low energy limit. The Cu atoms are anharmonically stabilized above approximately 100 K. The renormalized DOS at room temperature creates a vibrational Cu-II-dominated peak near 4 meV that has been observed in both inelastic neutron scattering [5] and first principles molecular dynamics (FPMD) simulations.

In this limit, the high amplitude vibrating atom Cu12e interacts with primarily energy carriers (phonons) in this compound [4]. Therefore, large intrinsic phonon scattering observed in this TE material is associated with out of plane vibration of Cu-II. The renormalized DOS at T = 300 K semi-quantitatively reproduces a vibrational Cu(2)-dominated peak near 4 meV that has been observed in both INS experiments [35] and FPMD simulations. The activity of the lone pair in Sb is believed to be the source for the asymmetric bonding and consequently resulting the anharmonicity in tetrahedrite.

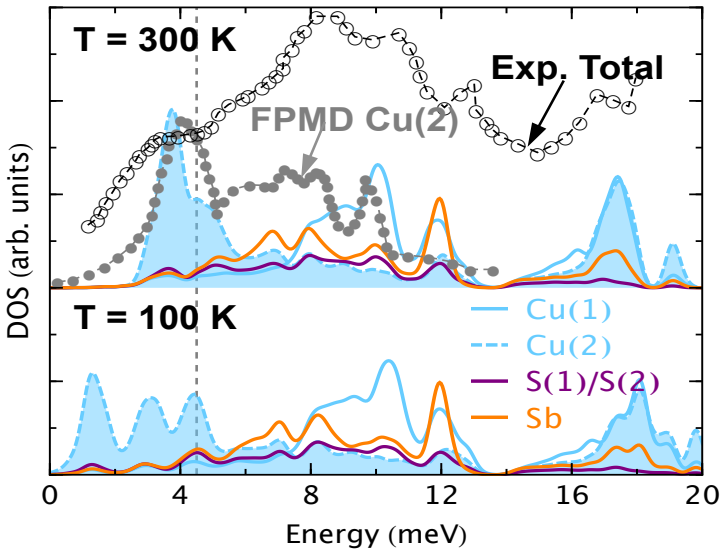

Figure 2.3: Vibration calculation of DOS in $Cu_{12}Sb_4S_{13}$ tetrahedrites at 100 and 300 K. Cu-II components are highlighted by filled colors, compared with the DOS of Cu-II from first-principles molecular dynamics (FPMD) simulations (grey dots) [4] and the total DOS from inelastic neutron scattering measurements (grey circles)[5]. Plot reprinted with permission from [6].

2.4 Rattling Behavior

The idea of rattling behavior in some compounds such as clathrates and multiple-filled skutterudites was first introduced by Slack [60], for cases where some atoms reside in oversized atomic sites, and may provide a mechanism for strong scattering of acoustic phonons. The multi-filled skutterudites are stable in an ambient temperature up to close to 950 K and can be created by adding guest metal atoms interstitially inside the large voids present in the crystal structure. In skutterudites, these cages consist of up to eight octahedra with radii from 2.04 to 1.76 Å for $IrSb_3$ and CoP_3, respectively. This enclosed space is big enough to accommodate an occupying atom each which allow them to rattle.

In the context of phonon scattering, the rattling elements (Cu-II in tetrahedrite) contribute phonon-phonon interaction due to the presence of the additional phonon modes in the occupied materials. Accordingly, comparing to skutterudites, the lattice thermal conductivity of partially-filled-skutterudites, over a large range of temperatures is significantly reduced [33]. Neutron scattering as well as XRD analysis are among the methods to measure anharmonic behavior in these compounds [69].

2.5 Anharmonicity

When we are expanding the potential energy of the ionic interactions several terms show up which could be considered as anharmonicity. An ideal harmonic crystal, at low phonon energies, without any impurities or defects will have a boundlessly high thermal conductivity, while lattice thermal resistivity emerges from the anharmonic terms in the ionic potential. In some materials the anharmonicity could come from specific chemical bonding or/and atomic arrangements. For example, in $AgSbTe_2$ the low lattice thermal conductivity is assigned to Sb lone pairs which leads to anharmonicity [70, 71, 72]. It was shown by Skoug and Morelli that the lone pair electrons play the key part in driving the anharmonicity in chalcogenide compounds such as $CuSbSe_2$ and Cu_3SbSe_3 to produce the low thermal conductivity [72]. In this group of materials, a repulsive force between lone pair electrons from group-V atoms (here antimony) and neighboring chalcogen

ions of selenium leads to anharmonicity and consequently enhances the thermal resistivity. It appears that the bond length, the coordination number of the group five atoms and the angle between chalcogen atom and group five atoms defines the strength of this anharmonicity. A similar behavior is observed in compounds with the $I-V-VI_2$ formula where their structure is similar to rock salt [73]. A few $I-V-VI_2$ stable compounds with lone pair electrons from group V atoms have anharmonic bonds that give rise to strong phonon-phonon interactions, which let their κ_L reach to the amorphous limit.

The Grüneisen parameter is one measure of anharmonicity, as defined by

$$\gamma_i = -\frac{\partial \ln(\omega_i)}{\ln(V)} \tag{2.3}$$

where ω_i is each phonon frequency and V is the crystal's volume. This parameter characterizes the bond "strength" in solid compounds and how it changes by varying the distance among atoms. If we only consider the acoustic phonon modes at high temperatures, for the heat conduction process, they will affect the thermal lattice conductivity by [74]:

$$\kappa_L \propto \frac{\langle M \rangle T_\theta^3 \delta}{N^{2/3} T \gamma^2} \tag{2.4}$$

where, T_θ is the Debye temperature, $\langle M \rangle$ is the average mass of the atoms, δ is the volume per atom, N is the number of atoms in the primitive unit cell and γ as defined above is the Grüneisen parameter.

A large Grüneisen parameter means intense anharmonicity which enhances thermal resistivity. The aforementioned reasoning can be applied particularly to the intrinsic low κ_L associated with tetrahedrites, and its crystal structure. κ_L is found to have a value around 0.5 (W/m K) in range of room temperature. From an experimental prospective, the Grüneisen parameter, averaged over all modes, can be written by [75]:

$$\gamma = \frac{9 B \alpha V_m}{C_V} \tag{2.5}$$

where, C_V is the specific heat, α the linear thermal expansion coefficient, V_m is the molar volume and B is the bulk modulus. In the Zinc doped tetrahedrite case ($Cu_{10}Zn_2Sb_4S_{13}$), C_V is around 4 J/K at 300 K, [76], $B = 44$ GPa [77] and α is 10.3×10^{-6} 1/K. Using the above equation gives a Grüneisen parameter around 2.1 at room temperature, which is comparable to values found for other compounds with large anharmonicity. For example, the Grüneisen parameter is 2.05 for $AgSbTe_2$ and 2.9 for $AgBiSe_2$ [71].

As is mentioned in section 2.1, in the context of anharmonicity for tetrahedrites, there are two important Cu atoms. Since Antimony is chemically bonded by three other S atoms, it is in the Sb^{3+} state which presents the classic chemical lone pairs. Since this Sb atom with its lone pair electrons dwells above/below the Cu-II plane, as illustrated in figure 2.4, both Sb above and below plane containing Cu-II and three S atoms establish a bipyramid assembly which could be assumed as a cage structure, somewhat similar to structure that observed in partially filled skutterudites and clathrates.

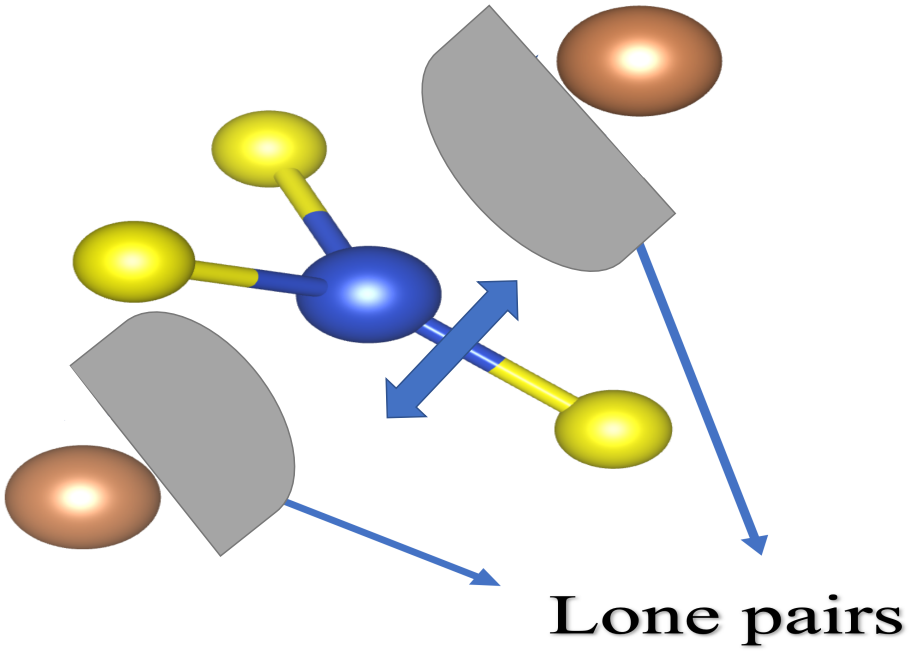

Figure 2.4: A portion of the $Cu_{12}Sb_4S_{13}$ crystal structure showing a trigonal bipyramid formed by the three Cu-S bonds and lone pair-containing Sb (brown) atoms above and below it. The grey shapes indicate the lone pairs, and the copper atom is indicated by the blue sphere. The arrow shows the movement of the Cu-II atom.

Suekuni was the first to investigate the Cu-II oscillation through the S trigonal plane [7] which was suspected to be the source of low κ (total thermal conductivity). Similar to other cage compounds, energy carrying phonons will be expected to be scattered by this low energy oscillation. Later study on the low temperature heat capacity disclosed that the data derived experimentally could be fit only if a Debye lattice is considered with three additional Einstein oscillators, associated with three localized modes from Cu-II atoms [76]. The oscillation of the Cu-II atoms perpendicular to the S triangular plane is associated with an Einstein oscillator with energy of 8.4 meV. The loose overlap of Sulfur's p-orbitals with Copper's d-orbitals leads to strong anharmonicity which is the reason for high amplitude type of oscillation. The movement of Cu-II atoms normal to S plane creates these two low energy Einstein oscillators. The other high energy Einstein

peak was measured in inelastic neutron scattering where density of states has a peak at temperature corresponding to 8.5 meV [5]. This supports the idea that Cu-II movements normal to S plane is the reason for strong anharmonicity in phonon-phonon interactions. Additionally, calculations on lattice dynamics led to unstable oscillating modes with imaginary frequencies which are believed to be associated to instability of Cu-II as shown above. Also, first principle calculations give rise to a double- well potential associated with Cu-II displacement [78].

2.6 Metal-semiconductor transition

While tetrahedrite has as a body centered cubic structure at ambient temperature, it also displays a structural phase transition at low temperature. This transition could be observed in the temperature dependent resistivity behavior of tetrahedrite sample in figure (2.5). Over several years, different groups identified through measuring magnetic susceptibility measurements, also observed in heat capacity as well as electric resistivity that a metal-semiconductor transition (MST) occurs in $Cu_{12}Sb_4S_{13}$ at temperatures near 83 K [7, 79, 80].

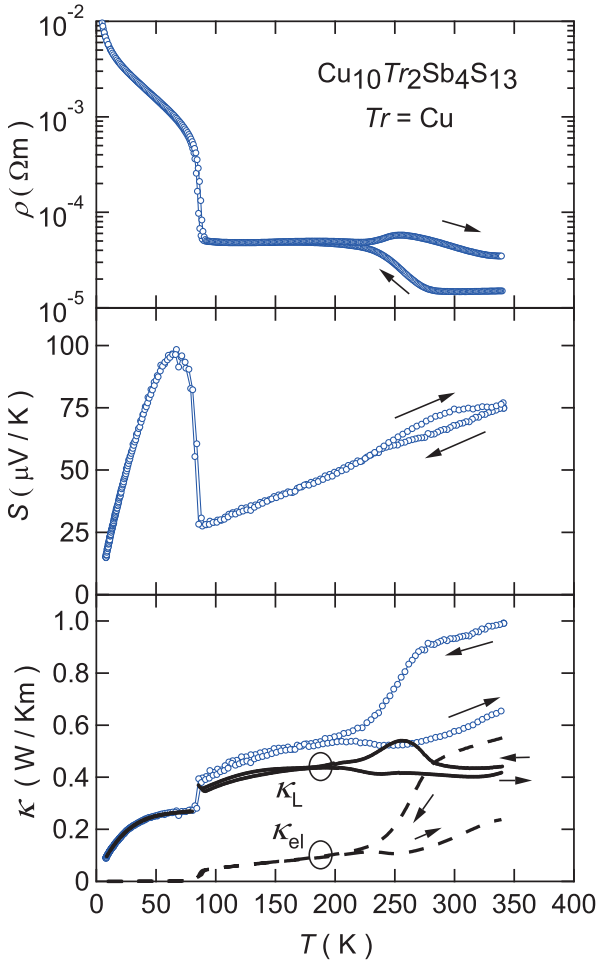

Figure 2.5: Temperature dependence of electrical resistivity, thermopower S, and thermal conductivity for unsubstituted phase $Cu_{12}Sb_4S_{13}$. The dashed line in the bottom figure represents electronic thermal conductivity κ_{el}, and the solid line shows lattice thermal conductivity κ_L. Reprinted with permission from [7]

Several mechanisms were suggested to describe the physical source of this MST [81, 5, 82]. Two main reasons are considered more likely: an antiferromagnetic-paramagnetic transformation and a Jahn-Teller distortion. A antiferromagnetic-paramagnetic transition is less likely to be the the reason for MST, since the tetrahedrite does not show magnetic order. Nevertheless, two relatively new studies proposed that a cubic-tetragonal phase transition also happens close to 85 K. A temperature-dependent powder X-ray diffraction (XRD) study indicates a first-order crystal structure transformation phase transition [5]. Also, a very recent paper showed that the trigonal-planar

copper cations remain in planar coordination below the MST [82]. On the other hand, Tanaka et al. [81] carefully studied the connection between physical properties and crystal structure below and above the phase transition temperature.

2.7 Electronic Properties

The electrical conductivity of tetrahedrite materials changes over almost six orders of magnitude for different compounds. In the $Cu_{12}Sb_4S_{13}$, the valence states of the elements are not well understood, and various models have been proposed in last decades.

In the context of crystal chemistry, ten Cu^+ plus two Cu^{2+} are expected to establish a stable charge balanced tetrahedrite $Cu_2^{2+}Cu_{10}^{+}Sb_4^{3+}S_{13}^{2-}$. In this context, it is assumed that Cu^{2+} atoms strictly fill the 12d positions and ionic bonding dominates [59]. In contrast, tetrahedrites are stable in a wide range of composition from $Cu_{12}Sb_{4.67}S_{13}$ to $Cu_{14}Sb_4S_{13}$. Thereafter, a Brillouin zone model was introduced by Johnson and Jeanloz [83] in order to analyze the electrical conductivities. This model explained that the electronic configurations of tetrahedrite is characterized by the total number of electrons in the valence band per unit cell assuming Cu to have valence equal to one. According to their model, for $Cu_{12}Sb_4S_{13}$ based compounds, the stability is enabled only with 204 to 208 valence electrons. An X-ray absorption spectroscopy confirmed this model and indicates that the proportion of Cu^+ to Cu^{2+} relies on chemical structure [84]. Density Functional Theory calculations also suggest that all twelve Cu atoms should stay in a monovalent state [3]. This model also explained the large ionic conductivity and presence of covalent bonding observed in tetrahedrites [4].

By these analyses, $Cu_{12}Sb_4S_{13}$ is electron-poor and should be metallic, while $Cu_{10}Zn_2Sb_4S_{13}$ has completely filled valence bands and should be a semiconductor. In fact, EPR (electron paramagnetic resonance) measurements illustrated that Cu atoms could be also in a magnetic divalent state in contrast to the assumption that all Cu atoms are in a monovalent state [85]. If, two of the twelve Cu atoms are assumed to be in a combination of Cu^+ and Cu^{2+} state this leads to the result that $Cu_{12}Sb_4S_{13}$ acts as a metal or a degenerate semiconductor which agrees with experimental results. Furthermore, this model implies that the valence electrons per unit cell shouldn't exceed 208,

and that for compositions closer to this number (equal to that of $Cu_{10}Zn_2Sb_4S_{13}$) the stability is enhanced. Optical spectra of an ore sample of tetrahedrite which was also believed to be an electron balanced semiconductor, demonstrated a 720 nm absorption edge implying a 1.7 eV bandgap. It has also been discovered [86] that some of the Cu ions are mobile. There are indications that this is due to the mixed state ions, however, this is not confirmed. Nevertheless, partially substituting [87] these two mobile coppers with other metals can apparently prevent this Cu ionic motion. Indeed, no ionic conductivity is witnessed for natural mineral sample, which are highly substituted. NMR relaxation studies can be particularly sensitive to the appearance of atomic hopping and this is one the issues explored in later chapters.

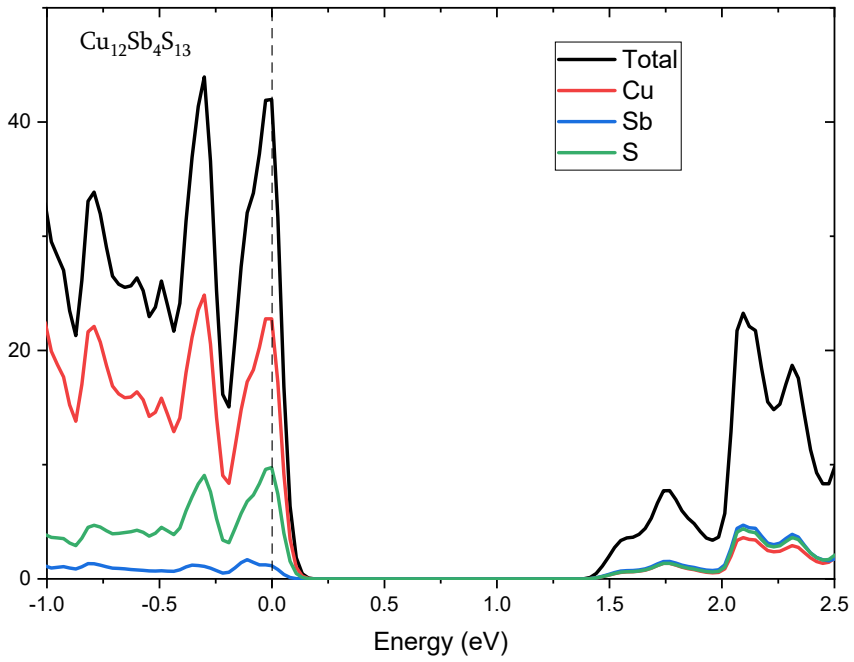

Figure 2.6: Electronic density of states (DOS) for $Cu_{12}Sb_4S_{13}$. Calculation method is discussed in chapter 6.

At room temperature, undoped tetrahedrites act as a p-type metal. In $Cu_{12}Sb_4S_{13}$ (figure 2.6), the hybridization of S 3p and Cu 3s orbitals creates the valence band, while the conduction band

is dominated almost equally by all atoms participating. The Fermi level remains on the top of the valence band, and the band gap is around 1.2 eV. The Hall measurements deliver a weak signal, identifying small mobility and positive charge carrier concentration [88, 3]. However, substituting various elements into the tetrahedrite crystal structure sites is currently an active field of investigation to boost these qualities in a favorable way.

2.8 Doping

Mixing two atoms or more to the parent compound is implemented in the TE composites in order to modify the phonon transport as well as electronic structure. The vast compositional range enabled by the crystal structure of Cu-based tetrahedrite has resulted a large number of studies of several doped and substituted samples. Doping is usually reserved for very small substitution amounts to change the number of carriers. Basically, a broad range of transition metals can substitute Cu atoms in $Cu_{12}Sb_4S_{13}$ crystal structure, and such substitution have been reported in naturally available mineral tetrahedrites [56]. Originally, thermoelectric behavior of doped tetrahedrite ($Cu_{10}\beta_xSb_4S_{13}$) substituted with transition metal (β = Zn, Cu, Ni, Co, Fe, and Mn) up to a restricting threshold of (x = 2), was studied by Suekuni et al. [7]. Among all such samples, $Cu_{10}Ni_2Sb_4S_{13}$ shows the highest ZT approching to 0.13 at 340 K.

Later, Heo et al. also presented thermoelectric behavior of fully substituted tetrahedrite at high temperature limit [89, 90]. Thereafter, several groups explored the electronic features of substituted tetrahedrites employing computational methods [68, 91]. As discussed earlier, for $Cu_{12}Sb_4S_{13}$ the Fermi level stands near the top of the valence band, and incorporating Zn, which mainly takes a divalent state, pushes the Fermi level up to the gap. In fact, Zn operates as a dopant by presenting its extra electrons to the pristine tetrahedrite lattice and filling its holes. By using this knowledge, Lu et al. observed a ZT close to unity at 720 K for Zn substituted tetrahedrite ($Cu_{11.5}Zn_{0.5}Sb_4S_{13}$) [3]. Hence, substituting the Cu by transition metals sets the stage for prospect investigation of tetrahedrites.

Since substitution of atoms in tetrahedrite began to be studied, several investigations have been reported into substituting 3d transition metals [88] and even 4p elements [58]. Crystal structure,

stability and magnetic behavior of synthetic tetrahedrite has been studied for dopants such as Cd [92], Zn [93, 66, 94], Co [65, 95], Mn [65], Ni [96, 94, 97, 93], Bi [97], and Fe [3, 98, 99, 100, 101]. So far, the highest ZT amongst various dopants is for Zn and Ni co-doped tetrahedrite with ($Cu_{10.5}NiZn_{0.5}Sb_4S_{13}$) chemical formula which yielded ZT around unity at 724 K [102]. In addition to improving the ZT, these investigations appear to imply that doping diminishes formation of secondary phases or impurities. Indeed, two groups reported explicitly that the favored tetrahedrite phase is formed in preference to other phases when small levels of substituted elements exist in the crystal structure [103, 104]. Later, many other research groups supported this observation with similar results [105, 106, 107]. Therefore, numerous analyses have indicated that doping and substituting with 3d transition metals not only improves ZT, but also stabilizes the principal tetrahedrite phase and reduces the Cu ion motion throughout the crystal structure. Although several studies investigated 3d transition metals substitution into the tetrahedrite, the large crystal structure along with the complexity of them enables more exotic doping possibilities. This includes Sn and Ge substitution $Cu_{12-x}(Ge,Sn)_xSb_4S_{13}$ for which x is restricted to 0.6 or less[108]. In other studies, Au and Ag doping has been reported to be feasible [109, 99] and Pb doping in tetrahedrite compound displayed improving figure of merit up to 40% at 720 K with a $Cu_{11}PbSb_4S_{13}$chemical formula [110]. In spite of toxicity and low efficiency of these samples, these analysis demonstrates that ample elemental doping could be studied. Therefore, a wide array of elements, aside from 3d transition metals, can be tested as a substitute on the Cu site in crystal structure.

Substituting dopants on Sb sites have also been inspected by several groups and in some cases, substantial enhancement in the materials performances were reported. Initially Lu and Morelli [111] prepared the compound $Cu_{12}Sb_{4-x}Te_xS_{13}$, where x is limited up to 1.5, and obtained a ZT peak of 0.92 for x=1 at 720 K. Following this study, Bouyrie et al. analyzed Te doping on the Sb site as well as continued multi element substituting (co-doping) with transition metals on the Cu site and Te on Sb sites [112, 113, 114, 93, 95]. Also, substituting Bi into the Sb site ($Cu_{12}Sb_{3.8}Bi_{0.2}S_{13}$) appears to improve the ZT up to 0.85 around 670 K [54]. While it has been confirmed that replacing Sb with As is possible in synthetic tetrahedrite [99], in natural minerals, it has been observed quite

often . In fact, the mineral is called "tennantite" when most or all of the Sb is substituted with As atoms [115, 116].

Replacing S sites in $Cu_{12}Sb_4S_{13}$ have been studied over last couple of years. Doped tetrahedrites with Te and Se elements as anions were investigated initially with mineralogical groups. However, lately some simulational calculations proposed the synthetic tetrahedrite with Se as the chalcongenide have stable phases [117, 118]. Later, a research analyzed a solid solution of $Cu_{12}Sb_4S_{13-x}Se_x$, where x was restricted up to 2, and yielded highest ZT of 0.85 at 720 K (for x=1) [119]. It has been agreed that ZT enhancement in Se doped samples associated with reduction in κ_L, as a result of strengthened alloy scattering of phonons. Afterwards, thermoelectric performance was lifted even higher by enriching the tetrahedrite with extra Cu ($Cu_{12+x}Sb_4S_{12}Se$), achieving an outstanding ZT of 1.1 at 720 K [120]. To this moment, this is the maximum reported ZT among all synthetic doped tetrahedrites. A very new report analyzed thermoelectric behavior of Zn with Sn co-doped tetrahedrite ($Cu_{11}ZnSb_4S_{12.75}Se_{0.25}$) and obtained the maximum ZT of 0.85 at 670 K [88]. In conclusion, doping Se to the tetrahedrites improves thermoelectric features, in particular, when incorporated with other effective substitutes.

2.9 Synthetic Methods

In this section we will review two synthetic methods and their advantages. First, we introduce the melting and recrystallized process, which is utilized more often than the other one. Normally tetrahedrites are consolidated from natural mineral ore and are referred as melting recrystallization process in articles. Second, solution phase methods such as solvo-thermal and hot injection will be discussed.

Most tetrahedrite studies implement a conventional recrystallization after melting process. In this method, quartz ampoules are filled with component precursors, then will be heated up to 923 K and kept at that temperature for at least 12 hours [121]. In this step, it is essential to keep the sample under constant 0.3 K min^{-1} heat rate to avoid the extra pressure accumulated from vaporized sulfur. The final ingot is not pure $Cu_{12}Sb_4S_{13}$, then, the final result is ground to fine powder, pressed, and annealed for up at 723 K for three weeks to improve homogeneity. The

final products were consolidated either with spark plasma sintering (SPS) or hot pressing. In conclusion, in order to achieve a single phase sample, this process requires long annealing time (one day up to 3 weeks), followed by a lengthy reaction periods (from 12 to 40 hours). There is a relatively similar method implemented to synthesize $Cu_{12}Sb_{3.6}Bi_{0.4}S_{10}Se_3$, however, the purity of the final product becomes challenging [122]. The melt recrystallization method is not a feasible processes at large scale because of its slow synthetic reaction times and the amount of utilized heat in the process. Hence, a rapid and economically cheap approach could be promising to promote tetrahedrite thermoelectric materials in large scale utilization.

Recently, it has been discovered that combining the natural mineral teterahedrites with chemically synthesized samples is a possibility. Initially, geologists and mineralogist were the ones who examined the basic features of natural ore of tetrahedrites. Later, when the thermoelectric potential of these materials was recognized, researchers started to analyze the physical properties of more mineralogical specimens [123, 87]. Indeed, most of the thermoelectric analysis by Seebeck measurements performed on mineral ores were mostly developed by Telks in the fifties [11, 124]. More recently, mineral specimens combined with chemically prepared tetrahedrites and the thermoelectric properties of the mixed samples were analyzed [125, 77]. In this method, the chemically synthetic tetrahedrite (processed with traditional approach) works as a seed matrix to promote the formation of a specific phase from the mineral ore specimens. Tetrahedrites processed with this mechanism demonstrate decreased κ_L and reduced σ (electric conductivity). The maximum ZT obtained with this method was 0.91 at temperatures close to 723 K [125]. In spite of the fact that this method is more effective in large scale commercial implementation and also economical, the natural mineral specimen usually accommodates a certain trace of impurities, which enhances the complexity of compositional control. In addition, chemically synthesized tetrahedrites show improved characteristics over their naturally based counterparts. However, natural mineral-based specimens are dependent on the synthetic tetrahedrite for the single phase $Cu_{12}Sb_4S_{13}$ seed. Therefore, mineral based thermoelectric tetrahedrite could be generated with small modifications beyond the traditional melting approach.

2.10 Cu_3SbS_4 phase

Refinement of the XRD for tetrahedrite samples normally shows a secondary Cu_3SbS_4 phase known as famatinite. This phase can be separately grown as a thin films for the purpose of the solar cell applications [126] due to its suitable optical and electrical properties and was even considered as a candidate for a topological insulator or semimetal[127].

The Cu_3SbS_4 crystal structure is tetragonal in an ordered sphalerite superstructure type which is in the space group of number 121 ($I\bar{4}m$). The lattice parameters for this phase are $a = 5.391$ Å, $c = 10.764$ Å, with volume of $c = 312.83$ Å^3 [128]. The crystal structure of Cu_3SbS_4 is shown in figure 2.7.

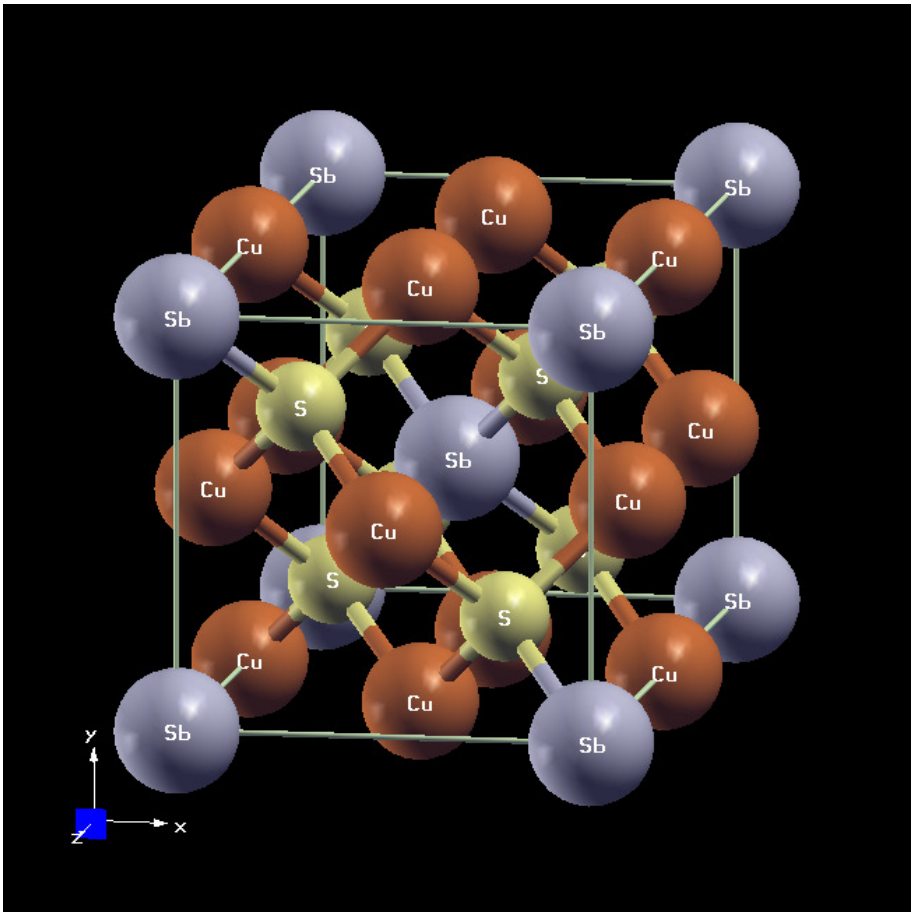

Figure 2.7: The crystal structure of Cu_3SbS_4.

In this crystal structure, there are two Cu sites with multiplicity of two to the one. Cu atoms fill sites 2b and 4d, the Sb atoms fill the site 2a, and S atoms fill sites 8i.

3. DENSITY FUNCTIONAL THEORY CALCULATIONS

Numerical simulations have become one of the most crucial tools in studying new materials. In recent years, advances in calculating facilities such as CPU, GPU, and memories made numerical simulations faster, easier and more accurate. First principle calculations used as a numerical method to solve a large number of problems. Implementing density functional theory (DFT) will transform the many body problem of interacting particles into a one particle reference that results in principle in the same electron density as the real system [129]. Solving the Schröodinger equation "*exactly*" for more than three interacting particles is impossible. Solving this equation for 10^{23} particles is a pharaonic task. However, we can approximate the exchange and correlation terms between electrons in DFT. Two of the approximations used are the generalized gradient approximation (GGA) [130] and local density approximation (LDA). However, LDA is viewed as having considerable limitations. It has been demonstrated that these two approximations are functional and reliable. These two methods predicted relatively accurate results for periodic arrangements and materials with defects, such as dislocations vacancies.

Lately two more approximations have been developed that can proceed with more accurate results. One approach employs pseudo-potentials that incorporates relatively simple basis set; whereas the other approach utilizes complex basis sets like the Linear Augmented Plane Wave Method (LAPW).

In most of calculations that I carried out, I used the WIEN2K package which runs calculations through the LAPW approach. In the LAPW case the plane waves are adopted close to atoms to replicate the rapid change in the wave functions of the valence electrons.

3.1 Starting from Scratch

We consider a solid a periodic set of positively charged particles (nuclei) that are heavy and are surrounded by lighter, negatively charged particles (electrons). If this solid has N nuclei the total number of particles with only electromagnetic potential will be $Z + NZ$. There are many particles

and since some of these particles are very light, we are dealing with quantum many body problem which the "exact" Hamiltonian for this set can be expressed as

$$\begin{aligned}\hat{H} &= -\frac{\hbar^2}{2}\sum_i \frac{\nabla^2_{\vec{R}_i}}{M_i} - \frac{\hbar^2}{2}\sum_i \frac{\nabla^2_{\vec{r}_i}}{m_e} \\ &\quad -\frac{1}{4\pi\epsilon_0}\sum_{i,j}\frac{e^2 Z_i}{|\vec{R}_i - \vec{r}_j|} + \frac{1}{8\pi\epsilon_0}\sum_{i\neq j}\frac{e^2}{|\vec{r}_i - \vec{r}_j|} + \frac{1}{8\pi\epsilon_0}\sum_{i\neq j}\frac{e^2 Z_i Z_j}{|\vec{R}_i - \vec{R}_j|} \end{aligned} \tag{3.1}$$

Where M_i is the mass of the nucleus located at $\vec{R}_i$, m_e is the mass of electrons at $\vec{r}_i$. As mentioned earlier, solving this problem exactly is out of question. To reach an acceptable approximate eigenstate, I explain the three approximations steps that have been taken.

3.2 The Born-Oppenheimer Approximation

Electrons are much lighter and move very rapidly while the nuclei are heaver and slower. Thus, it can be assumed that the nuclei are frozen at fixed locations with electrons being in instantaneous equilibrium with them. This means that electrons remain as the only players in the many body problem. The role of the nuclei reduces to a source of positive charge and they are being considered as external particles to the cloud of electrons. This leaves the solid system as a set of NZ interacting negatively charged electrons that are moving in the area filled with the potential due to nuclei. This approximation is the Born-Oppenheimer approximation.

After considering the Born-Oppenheimer approximation, some terms in equation (3.1) disappear. This leaves the Hamiltonian with only following terms

$$\hat{H} = \hat{K} + \hat{V} + \hat{V}_{ext} \tag{3.2}$$

where $\hat{T}$ is the kinetic energy of the electron gas, $\hat{V}$ is the potential energy due to electron-electron interactions, and $\hat{V}_{ext}$ is the potential energy of the electrons due to the nuclei.

3.3 Density Functional Theory

After the first step of approximation, the quantum many body problem is substantially easier than the original equation, however, it is still very difficult to solve. Historically, the DFT theory was expanded substantially by Hohenberg and Kohn [131].

Their approach states that there is a one to one mapping between the ground-state density $\rho(\vec{r})$ of a many electron assembly (could be an atom, a molecule, or a solid) and the external potential V_{ext}. A direct conclusion is that the ground state expectation value of any observable quantity is a distinctive functional of the exact ground state electron density, $\langle\Psi|\hat{Q}|\Psi\rangle$. Afterwards, if we allow the observable quantity $\hat{Q}$ to be a many-body Hamiltonian, then the the ground state total energy functional can be given as:

$$E_{V_{ext}}[\rho] \equiv H[\rho] = \underbrace{\langle\Psi|(\hat{T}+\hat{V})|\Psi\rangle}_{F_{HK}[\rho]} + \langle\Psi|\hat{V}_{ext}|\Psi\rangle \tag{3.3}$$

where the $F_{HK}[\rho]$ (known as the Hohenberg-Kohn density functional) is universal for all many electron assembles. In other words, the **total** ground state energy $E_{V_{ext}}[\rho]$ is mapped uniquely to the ground state energy of $V_{ext}[\rho]$.

Slightly later, Kohn and Sham published a paper that changed DFT into a practical tool [129]. They developed an algorithm to derive the ground state density. They consider the energy functional as :

$$E_{V_{ext}}[\rho] = T_0[\rho] + V_H[\rho] + V_{xc}[\rho] + V_{ext}[\rho], \tag{3.4}$$

which is equation (3.3), where $F_{HK}[\rho]$ is replaced by $T_0[\rho] + V_H[\rho] + V_{xc}[\rho]$. $T_0[\rho]$ is the single particle kinetic energy, $V_{xc}[\rho]$ is the exchange correlation energy functional, and $V_H[\rho]$ is the Hartree component of the electron-electron energy.

The analogous Hamiltonian (known as the Kohn-Sham Hamiltonian) is:

$$\begin{aligned}\hat{H}_{KS} &= \hat{T}_0 + \hat{V}_H + \hat{V}_{xc} + \hat{V}_{ext} \\ &= -\frac{\hbar^2}{2m_e}\vec{\nabla}_i^2 + \frac{e^2}{4\pi\epsilon_0}\int \frac{\rho(\vec{r}')}{|\vec{r}-\vec{r}'|}d\vec{r}' + \hat{V}_{xc} + \hat{V}_{ext}. \end{aligned} \tag{3.5}$$

The Hartree component, a functional of the electron-electron energy is

$$V_H[\rho] = \frac{e^2}{4\pi\epsilon_0}\int \frac{\rho(\vec{r}')\rho(\vec{r})}{|\vec{r}-\vec{r}'|}d\vec{r}'d\vec{r}. \tag{3.6}$$

In the Local Density Approximation (LDA) method, the exchange-correlation functional has the following form:

$$E_{xc}^{LDA} = \int \rho(\vec{r})\varepsilon_{xc}(\rho(\vec{r}))d\vec{r}. \tag{3.7}$$

In the above equation, $\varepsilon_{xc}(\rho(\vec{r}))$ is approximated by a local density functional, while, in the GGA method, the gradient of the density will play a role. In fact, the local gradient density functional together with local density functionals are used together with the local density to include more details about the electron gas numerically, so the ε_{xc} will be $\varepsilon_{xc}(\rho(\vec{r}), \vec{\nabla}\rho(\vec{r}))$.

The LDA method is anticipated to perform well for structures with a slightly varying density. However, rather surprisingly, it appears to be notably precise in several other (realistic) cases too.

In order to find a solution for equation(3.4), various approaches have been employed. However, in this dissertation, I discuss LAPW (Linearized Augmented Plane Wave) approach which is a developed version of the APW method. Therefore, I explain the APW method first.

In order to solve the Schrödinger equation in solids, we can separate the space into two parts. One region represents the spherical space with radius R_α near each individual nuclei where the wave functions and potentials are the same as the interior atom. This volume is known as the *muffin tin* region indicated by S_α. The remaining space outside the spheres is called the interstitial region I. In the APW approach the core potential is substituted with a pseudo-potential. Then, the

solutions function for inside and outside of the muffin tin is given by:

$$\phi_{\vec{K}}(\vec{r}, E) = \begin{cases} \frac{1}{\sqrt{V}} e^{i(\vec{k}+\vec{K})\cdot\vec{r}} & \vec{r} \in I \\ \sum_{l,m} A_{l,m} u_l^{\alpha}(\vec{r}', E) Y_m^l(\hat{r}') & \vec{r} \in S_\alpha \end{cases} \tag{3.8}$$

where V is the unit cell's volume, the $u_l^{\alpha}(\vec{r}', E)$ is the solution to the radial component of the Schrödinger equation for an atom α with energy E. $Y_m^l(\hat{r}')$ are spherical harmonics.

To address the locations inside the muffin tin, a position $\vec{r}'$ is introduced with respect to the origin of other sphere as shown in figure (3.1).

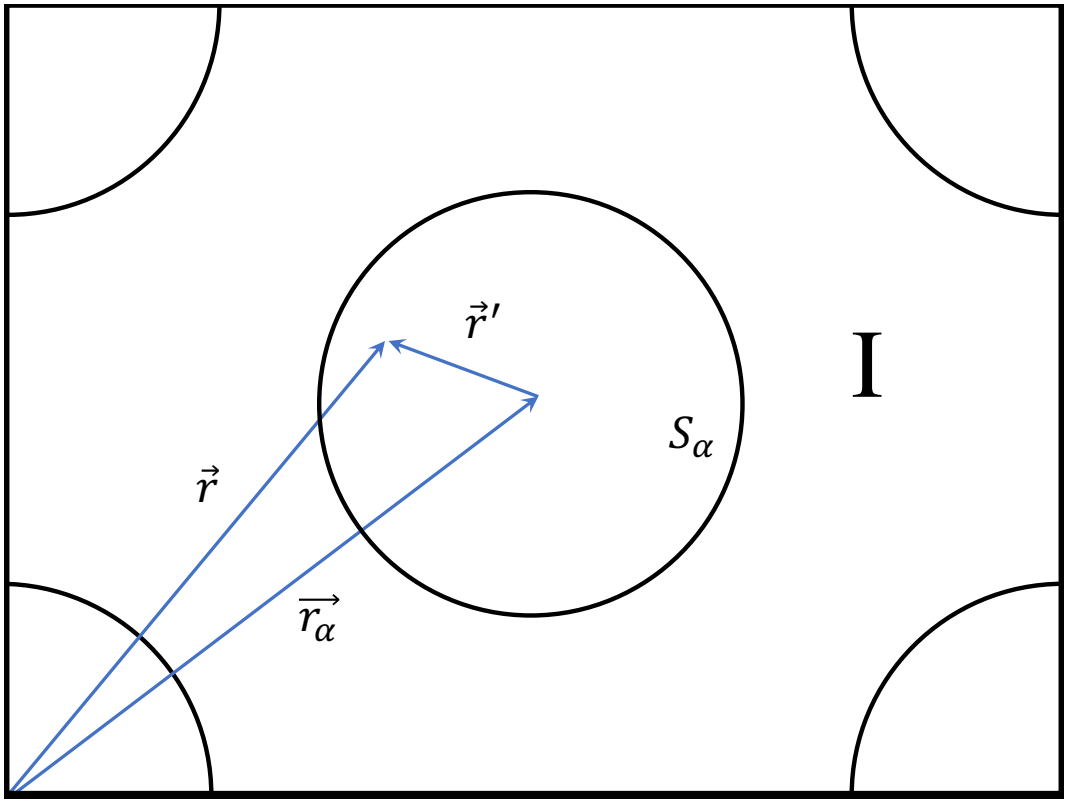

Figure 3.1: The muffin tin region and the interstitial region, for a case with two atoms.

There were a number of problems with the APW approach. The major problem is that the $u_l^{\alpha}(\vec{r}', E)$ is dependent on the unknown energy parameter of a searched eigenstate. Another draw-

back is the functions $u_l^\alpha(\vec{r}', E)$ vanish on the edges of the muffin tin boundary for general values of the energy parameter E, which subsequently leads to decoupling between the plane waves and the radial wave functions. In order to solve the energy dependence of the basis set several methods were suggested. A simple and precise method is the LAPW approach. This method utilizes linear combination of $u_l^\alpha(\vec{r}', E)Y_m^l(\hat{r}')$ and the derivation of their energy over to the linearization parameters, E as

$$\phi_{\vec{K}}(\vec{r}, E) = \begin{cases} \frac{1}{\sqrt{V}} e^{i(\vec{k}+\vec{K})\cdot\vec{r}} & \vec{r} \in I \\ \sum_{l,m} \left(A_{l,m} u_l^\alpha(\vec{r}', E) + B_{l,m} \underbrace{\frac{\partial u_l^\alpha(\vec{r}', E)}{\partial E}\Big|_{E_0}}_{\dot{u}_l^\alpha(\vec{r}', E)} \right) Y_m^l(\hat{r}') & \vec{r} \in S_\alpha, \end{cases} \tag{3.9}$$

where $r\dot{u}_l^\alpha(\vec{r}', E)$ is the solution to the radial part of the Schrödinger equation.

The precision of a plane wave basis set relies on K_{max}. It was useful to set a criterion for LAPW. A better quantity to look into for accuracy can be $R_{min}^\alpha K_{max}$, which is the product of the smallest muffin tin radius and K_{max}.

3.4 WIEN2K and NMR Quantities

I used the WIEN2k package to run *ab-initio* calculations [132]. This package implements the full potential linearized augmented plane wave approach. WIEN2k is among the most accurate schemes for band structure calculations. Various properties such as bandstructure, electron density of states, phonon behavior exhibiting vibrational modes, hyperfine fields [133], electron densities, Fermi levels, spin densities, forces, total energy, optical properties, equilibrium geometry, and of particular significance here, NMR chemical and Knight shifts [134], and electric field gradient (EFG) [135] could be calculated through this package. The EFG is a parameter (chapter 4) that is reflective of the electric charge density near the nucleus and associated with ground state density which is reperesntive of quadrupole interaction of the nucleus.

For calculations described here, I implemented the Generalized Gradient Approximation (GGA) where the exchange correlation was chosen to be Perdew-Burke-Ernzerhof (PBE).

I calculated EFG parameters for various sites in various samples from all-electron distribution. Equations for NMR frequencies in a crystal when excited from m_z to (m_z+1) states are discussed in [136]. As will be discussed in section (4.1.7) with details, the quadrupole shift can be expressed in forms of the EFG principal values ($\frac{\partial^2 V}{\partial x^2}, \frac{\partial^2 V}{\partial y^2}, \frac{\partial^2 V}{\partial z^2}$), and the quadrupole is obtained from $\nu_Q = \frac{3e^2qQ}{2hI(2I-1)}$, where Q is the quadrupole moment, and $eq = \frac{\partial^2 V}{\partial z^2}$ is the largest principal value. The quadrupole effect on the NMR shift can be considered with perturbation theory, for all calculations, I treated first and second-order quadrupole shift for each transition.

The NMR shielding tensor $\hat{\sigma}$ is determined as induced magnetic field B_{ind} on the nucleus at position R due to an external uniform field B_{ext}, typically given in part per million (ppm). The tensor $\hat{\sigma}$ is measured and must be compared to a reference compound.

$$\delta(\mathbf{R}) = \sigma_{\mathbf{ref}} - \sigma(\mathbf{R}). \tag{3.10}$$

Most times only the isotropic part $\sigma(\mathbf{R}) = \mathbf{trace}[\sigma(\hat{\mathbf{R}})]$ is determined. The impact of the B_0 on the nucleus is a minor perturbation regarding to the typical scale of energy in the electronic structure. Thus, its effect on the spin and orbit of the electron will be separated in the WIEN2K calculations. A more detailed discussion can be found in section (4.1.3).

The orbital contribution to the shielding tensor or the orbital portion of the induced magnetic field is derived from the Biot-Savart equation as :

$$B_{ind}(\mathbf{R}) = \frac{\mathbf{1}}{\mathbf{c}} \int \mathbf{j_{ind}}(\mathbf{r}) \times \frac{\mathbf{r}-\mathbf{R}}{|\mathbf{r}-\mathbf{R}|^{\mathbf{3}}}. \tag{3.11}$$

$\mathbf{j}(\mathbf{r})$ is the induced current due to orbital electrons and derived from

$$j_{ind}(\mathbf{R}) = -\frac{\mathbf{p}|\mathbf{r}\rangle\langle\mathbf{r}| + |\mathbf{r}\rangle\langle\mathbf{r}|\mathbf{p}}{\mathbf{2}} - \frac{\mathbf{B_{ext}} \times \mathbf{r}}{\mathbf{2c}}|\mathbf{r}\rangle\langle\mathbf{r}|, \tag{3.12}$$

In WIEN2K the contribution of core states and valence states are derived separately. For the

calculation of the core part, only a spherically symmetric core density is employed as

$$j_{core}(\mathbf{r}) = -\frac{\mathbf{1}}{\mathbf{2c}}\rho_{\mathbf{core}}(\mathbf{r})\mathbf{B_{ext}} \times \mathbf{r}. \tag{3.13}$$

The valence electron contribution to the induced $\mathbf{j}(\mathbf{r})$ is given by

$$j_{valence}(\mathbf{r}) = \sum_{\mathbf{o}} \Big[\langle \ {}^{\mathbf{(1)}}_{\mathbf{o}} | \mathbf{J^{(0)}}(\mathbf{r}) | \psi^{\mathbf{(0)}}_{\mathbf{o}} \rangle + \langle \psi^{\mathbf{(0)}}_{\mathbf{o}} | \mathbf{J^{(0)}}(\mathbf{r}) | \psi^{\mathbf{(1)}}_{\mathbf{o}} \rangle + \langle \psi^{\mathbf{(0)}}_{\mathbf{o}} | \mathbf{J^{(1)}}(\mathbf{r}) | \psi^{\mathbf{(0)}}_{\mathbf{o}} \rangle \Big], \tag{3.14}$$

where $J^{(0)}$ and $J^{(1)}$ are paramagnetic and diamagnetic contribution of the current operator, ${}^{(0)}_{o}$ is an unperturbed Kohn and Sham occupied orbital and ${}^{(1)}_{o}$ is the first order perturbation of ${}^{(0)}_{o}$ given by :

$$| \ {}^{(1)}_{o} \rangle = \sum_{e} | \ {}^{(1)}_{e} \rangle \frac{\langle \ {}^{(1)}_{e} | H^{(1)} | \psi^{(0)}_{o} \rangle}{\varepsilon_o - \varepsilon_e} + \sum_{core} | \ {}^{(1)}_{core} \rangle \frac{\langle \ {}^{(1)}_{core} | H^{(1)} | \psi^{(0)}_{o} \rangle}{\varepsilon_o - \varepsilon_{core}} \tag{3.15}$$

and $H^{(1)}$ is the perturbation because of the external magnetic field given by:

$$H^{(1)} = \frac{1}{2c}(\mathbf{r} \times \mathbf{p}) \cdot \mathbf{B_{ext}}. \tag{3.16}$$

In order to carry out the the induced spin density and spin part of the NMR shielding tensor, WIEN2k uses the following equation to find the magnetic hyperfine field at the nucleus

$$\mathbf{B_{hf}} = \underbrace{\frac{8\pi}{3}\mu_B \mathbf{m_{av}}}_{B_c} + \underbrace{\left\langle \Phi_1 \middle| \frac{S(r)}{r^3}\big[3(\mu.\hat{r})\hat{r} - \mu\big] \middle| \Phi_1 \right\rangle}_{B_{sd}} \tag{3.17}$$

Where B_c is the Fermi contact term, $\mathbf{m_{av}}$ is the average spin density over the spherical volume that contains the nucleus when its diameter is equivalent to the Thomson radius. The B_{sd} is the spin-dipolar component of the hyperfine field. Φ_1 is the large component of the wave function, S is the reciprocal relativistic mass enhancement, and μ is the magnetic moment operator of the electron. Since B_{sd} calculations are carried out on the atomic core, its computing is simple. Therefore,

the Knight shift can be calculated by

$$\mathbf{B_{hf}} = -\hat{\sigma}_{\mathbf{s}}\mathbf{B_{ext}} = -(\hat{\sigma}_{\mathbf{c}} + \hat{\sigma}_{\mathbf{sd}}) \cdot \mathbf{B_{ext}}. \tag{3.18}$$

To perform NMR shielding and give reliable results which may be dependant on measurement sensitive to 1 ppm or better, WIEN2k implements a 100 Tesla external magnetic field. This enormous magnetic field induces spin splitting in the size of 1 mRy. This requires a particularly large number of k-points. For example, for Al with a face centered cubic (fcc) structure 1000000 k-points is needed.

The nuclear magnetic resonance (NMR) spectroscopy is a very powerful non-selective, nondestructive analytical tool for material characterization, both in solution and in solid state. Solid-state nuclear magnetic resonance (NMR) consists of several techniques, which are distinguished by different pulse sequences and generate different responses in the sample, allowing obtaining data on different time scales. This provides the basis for understanding measurable and informative NMR parameters: hyperfine coupling including quadrupole shift and chemical shift, motional narrowing linewidths, and relaxations. In this dissertation, we will use these techniques to study various materials.

4.1 Nuclear Magnetic Resonance

The Hamiltonian that governs the nuclear spin involves a sum of different Hamiltonians, according to

$$H_{tot} = \underbrace{H_Z + H_{Rf}}_{H_{External}} + \underbrace{H_{CS} + H_K + H_{DD} + H_J + H_Q}_{H_{Internal}} \tag{4.1}$$

where H_Z is the Zeeman Hamiltonian, H_{Rf} is the a radio frequency Hamiltonian, H_{CS} is the chemical shift Hamiltonian, H_K is the Knight shift, H_J is the J-coupling Hamiltonian, H_{DD} is the dipole-dipole Hamiltonian, H_Q is the quadrupolar Hamiltonian. The first two terms are external Hamiltonians which are under human control (e.g., the magnet, magnetic field gradients, and radio-frequency pulses), while the others are internal Hamiltonians determined by their local atomic level environment. We will introduce these terms in the next sections.

4.1.1 Zeeman Hamiltonian

In equation (4.1), the Zeeman interaction (Hz) is the main term which contains the interaction between the externally applied magnetic field, B_0 and the magnetic moment of the nucleus. A nucleus with spin $\vec{I}$ has a magnetic moment, $\vec{\mu} = \gamma\hbar\vec{I}$, where γ is the gyromagnetic ratio. The

Zeeman interaction occurs only with nuclei that possesses non zero spin and yields $2I + 1$ energy levels of separation with $\omega_0 = \gamma B_0$ energy separation. ω_0 is also called the Larmor frequency. The Zeeman Hamiltonian is given by [137]

$$H_Z = -\vec{\mu} \cdot \vec{B_0} = -\gamma \hbar I_z B_0 = -\hbar \omega_0 I_z. \tag{4.2}$$

The interaction is linear with applied magnetic field and thus leads to the stimulus to produce higher magnetic field spectrometers. In fact, larger separation of the energy levels results to higher population difference and consequent enhancement in signal to noise proportion within the measured spectrum. Since the Zeeman Hamiltonian depends on the gyromagnetic ratio, which is constant for each individual nucleus, the Larmor frequency ω_0 for each nucleus is unique at a particular applied external magnetic field. Slight perturbations to the Zeeman term are generated by other interactions such as RF field terms, shielding, dipole-dipole effect, spin-spin coupling, and quadrupolar terms.

4.1.2 RF field Hamiltonian

The RF-field Hamiltonian H_{Rf} has the same form as the Zeeman Hamiltonian,

$$H_{Rf} = -\vec{\mu} \cdot \vec{B_1}(t) = -\gamma \hbar I_z B_1(t). \tag{4.3}$$

The applied radiofrequency field $\vec{B_1}(t)$, oscillates with the frequency ω_1 which is linearly polarized with the phase $\phi(t)$,

$$\vec{B_1}(t) = 2B_1 cos(\omega_1 t) \left[\vec{e_x} cos(\phi) + \vec{e_y} sin(\phi)\right]. \tag{4.4}$$

In this condition equation (4.3) can be written in the form:

$$\hat{H}_{Rf}(t) = -2\hbar\gamma B_1 cos(\omega_1 t) \left[\hat{I}_x cos(\phi) + \hat{I}_y sin(\phi)\right]. \tag{4.5}$$

To solve equation (4.3), it is desirable to change the Rf-field Hamiltonian to a time independent

form by the transforming it to the rotating frame. In fact, a Hamiltonian $H_{tot} = H_Z + H_{Rf}$ can be transformed to the H_Z-Hamiltonian representation by the transformation

$$\hat{H}^r_{tot} = e^{\frac{i}{\hbar}\hat{H}_Z t}\hat{H}_{tot}e^{-\frac{i}{\hbar}\hat{H}_Z t} = \hat{H}_Z + e^{\frac{i}{\hbar}\hat{H}_Z t}\hat{H}_{Rf}e^{-\frac{i}{\hbar}\hat{H}_Z t}. \tag{4.6}$$

The transformation of the RF field interaction to the rotating coordinate frame as follows from the equation (4.6) can be expressed as

$$\hat{H}^r_{Rf} = e^{\frac{i}{\hbar}\hat{H}_Z t}\hat{H}_{Rf}e^{-\frac{i}{\hbar}\hat{H}_Z t} \tag{4.7}$$

based on equation (4.2), $\hat{H}_Z = \hbar\omega_0\hat{I}_z$, the basic trigonometric equation, equation (4.7), may be written as

$$\hat{H}^r_{Rf} = -2\hbar\gamma B_1\cos(\omega_1 t)\left[\hat{I}_x\cos(\omega_0 t - \phi) - \hat{I}_y\sin(\omega_0 t - \phi)\right]. \tag{4.8}$$

Continued consolidation of the trigonometric functions will result in the equation which comprises two pairs of coefficients as $\omega_1 \pm \omega_0$ as arguments in the cos, sin functions. Selecting $\omega_1 = \omega_0$ the oscillations at frequencies $\omega_1 + \omega_0 = 2\omega_0$ can be ignored because the nuclear magnetization is affected substantially only by fields rotating with the angular frequency near to the nuclear Larmor frequency ω_0. This leads to

$$\hat{H}^r_{Rf} = -\hbar\gamma B_1\left[\hat{I}_x\cos(\Omega t + \phi) + \hat{I}_y\sin(\Omega t + \phi)\right]. \tag{4.9}$$

where $\Omega = \omega_1 - \omega_0$ is the offset with respect to the RF-field frequency ω_1.In the case of resonance for spins the r.f. field term turns explicitly time independent and the final form can be written as :

$$\hat{H}^r_{Rf} = -\hbar\gamma B_1\left[\hat{I}_x\cos(\phi) + \hat{I}_y\sin(\phi)\right]. \tag{4.10}$$

4.1.3 Chemical Shift Hamiltonian

The three-dimensional magnetic shielding by surrounding electrons is the third interaction in equation (4.1) that the nucleus senses either in solid state or liquid. In some NMR cases, the chemical shift Hamiltonian (H_{CS}) is the most responsive interaction to variations in the instant environment of the nucleus. However, in solid state NMR, the Knight shift can play a much important role than chemical shift.

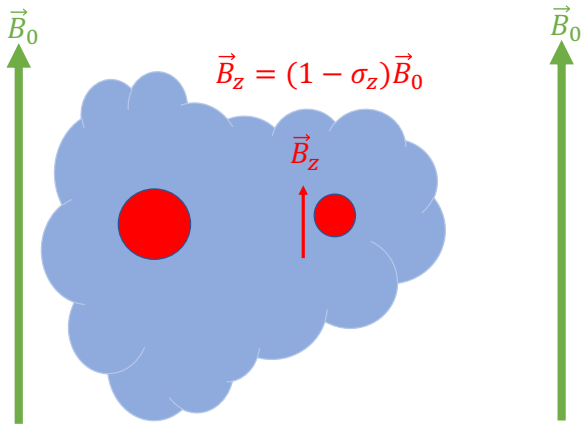

Figure 4.1: Schematic figure of chemical shielding and the magnetic field experienced by nucleus.

The chemical shift term emerges from the slight local magnetic fields that are formed around the nucleus by electric currents induced in electron orbitals by an applied external field B_0. This slight perturbation on the nucleus appears in a small change in the total magnetic field experienced by the nucleus. Hence, the magnetic field at the nucleus is not the same as the externally applied field and accordingly this difference is the nuclear magnetic shielding and paramagnetic effects, or chemical shift interaction $B_z = (1 - \sigma_z)B_0$, as displayed in figure (4.1). The chemical shift

Hamiltonian is expressed as

$$H_{CS} = -\gamma\hbar\vec{I}\cdot\hat{\sigma}\cdot\vec{B}_0 = \hbar\omega_0(\sigma_{xz}I_x + \sigma_{yz}I_y + \sigma_{zz}I_z) \tag{4.11}$$

Note that in the equation (4.11), $\hat{\sigma}$ is the shielding tensor and depends on the orientation and is proportional to the strength of the applied magnetic field. Therefore, it is essential to compare our results with reference materials. We can always transform to a basis that the chemical shift tensor $\hat{\sigma}$ is diagonal. This frame is called principal axes system (PAS) and the chemical shift tensor has diagonal form which can be given by

$$\sigma_{iso}^{CS} = \frac{1}{3}(\sigma_{xx}^{P} + \sigma_{yy}^{P} + \sigma_{zz}^{P}). \tag{4.12}$$

Note that what we measure in the experiment is independent of the frame since we are tracing the $\hat{\sigma}$. Note that in this dissertation the chemical shift $\delta = -\hat{\sigma}$ is used.

In solid state NMR, the chemical shift amount is representative of the effective magnetic environment of a nucleus, but in comparison to solution state spectrum, the molecules are not allowed to move. It is important to note that the shielding depends on the particular orientation of the solid in regard to B_0. Hence, a certain arrangements of the spins perpendicular to the applied magnetic field delivers a sharp spectrum representative of this specific orientation. For most polycrystalline samples, a random distribution generates all feasible orientations. This leads to a very broad peak in NMR lineshape. The size of the chemical shift anisotropy, depending on materials is between 0 and 10^5 Hz. There are more contributions that will be discussed with detail in next section.

4.1.4 Knight Shift Hamiltonian

The Knight shift denoted by K indicates the relative shift due to the spins, in NMR frequency for nuclei in a metal (e.g. copper) compared with the same nuclei in a nonmetallic condition (e.g. copper chloride). The measured shift shows the local magnetic field generated at the Cu nucleus by the magnetization of the conduction electrons. The local magnetic field in Cu metal enhances the applied resonance magnetic field by around 2000 ppm. In nonmetallic copper chloride the average

local field on Cu is negligible in comparison.

The Hamiltoniam for interaction of a conduction electron and the nucleus can be expressed as [138] sum of the following terms

$$\hat{\mathbf{H}} = -\mathbf{2}\gamma_{\mathbf{n}}\hbar\mu_{\mathbf{B}}\tilde{\mathbf{I}} \cdot [\frac{\mathbf{8}\pi}{\mathbf{3}}\tilde{\mathbf{S}}\delta(\mathbf{r}) + [\frac{\mathbf{3}\tilde{\mathbf{r}}(\tilde{\mathbf{r}} \cdot \tilde{\mathbf{S}})}{\mathbf{r^5}} - \frac{\tilde{\mathbf{S}}}{\mathbf{r^3}}] - \frac{\tilde{\mathbf{I}}}{\mathbf{r^3}}] \tag{4.13}$$

where $\vec{I}$ and $\vec{S}$ are the nucleus and electron spin, respectively, $\vec{l}$ is the electron's orbital angular momentum, and $\vec{r}$ is the electron's position vector. The first term in the equation is the Fermi contact interaction, which s-characterterize the significant part of the conduction electrons. The second term denotes the spin dipolar correlation between the spin of electron and nucleus, an anisotropic Knight shift in the non-cubic symmetry environment is due to this term. In powder forms, in the cases without quadrupole shift, this component can be a primary reason for broadening of the NMR line shape. The last term introduces the interaction between electron's orbital momentum with nucleus spin. In our samples this term is very crucial because the orbital shift is roughly proportional inversely to the bandgap which is typically small in the d-bands in Cu based tetrahedrites, however, this term is normally included with chemical shielding.

Since the electrons and nuclei are weakly interacting the wave function can be written $\psi_e\psi_n$. If we consider delocalization of conduction electrons and periodicity of the lattice, the ψ_e could be decomposed as $\psi_{\vec{k}}\psi_s$, where $\psi_{\vec{k}} = u_{\vec{k}}exp(i\vec{k} \cdot \vec{r})$. Hence, the shift in energy due to the first term of the equation (4.13) can be written as

$$\Delta E = -\gamma h I_z \left[\frac{8\pi}{3}\langle|u_{\vec{k}}(0)|^2\rangle^2_{E_F}\chi_P B_0\right] \tag{4.14}$$

where, χ_P is the Pauli spin susceptibility of the conduction electrons. Note that $\langle 2\mu_B S_z\rangle = \chi_p B_0$. Therefore, the Knight shift due to s-electron can be written as

$$K_s = \frac{\Delta\omega}{\omega_0} = \frac{\Delta B}{B_0} = \frac{8\pi}{3}\langle|u_{\vec{k}}(0)|^2\rangle_{E_F}\chi_P. \tag{4.15}$$

The Knight shift is associated with susceptibility through the spatial variation of the electron wave function. This can be considered as the intensity of the magnetic field on the the nucleus. Hence, we could use this function to determine the hyperfine field B_{hf} as

$$\frac{B_{hf}}{\mu_B} = \frac{8\pi}{3}\langle|u_{\vec{k}}(0)|^2\rangle_{E_F}. \tag{4.16}$$

The Knight shift due to the Pauli susceptibility K_s can be given by

$$K_s = \frac{B_{hf}^s}{\mu_B}\chi_P. \tag{4.17}$$

The Knight shift can also give some information on density of states, since the Pauli susceptibility is linked to DOS through $\chi_P = 2\mu_B^2 g(E_F)$.

The last term in equation (4.13), contains the interaction of orbital angular momentum induced in occupied conduction electron states with nucleus in an applied magnetic field. From the tight binding Green's function approximation there is a general form [136]

$$\mathbf{K_{orbital}} = \frac{\mathbf{2e^2}}{\mathbf{(mc)^2}}\sum_{\mathbf{\Psi'}}\frac{\langle\mathbf{\Psi}|\mathbf{L_z}|\mathbf{\Psi'}\rangle\langle\mathbf{\Psi'}|\frac{\mathbf{L_z}}{\mathbf{r^3}}|\mathbf{\Psi}\rangle}{\mathbf{\Delta E}}. \tag{4.18}$$

Where $\mathbf{\Psi}$ and $\mathbf{\Psi'}$ are the occupied states and excited states, respectively. The sum goes over all excited states. In equation 4.18, a slight change in ΔE can result in a significant orbital shift in the transition metals since for d bands ΔE is very small. This Knight shift term also known as the Van Vleck Knight shift. Similar to equation (4.17), the orbital Knight shift can be expressed as

$$\mathbf{K_{orbital}} = \frac{\mathbf{B_{hf}^{orbital}}}{\mu_\mathbf{B}}\chi_{\mathbf{VV}} \tag{4.19}$$

where χ_{VV}, is the Van Velck susceptibility, and $B_{hf}^{orbital} \propto \langle\frac{2\mu_0\mu_B}{r^3}\rangle_\Psi$ can be used to approximate the $B_{hf}^{orbital}$.

Other effects on the Knight shift can be due to the conduction electrons that contain the core polarization or involving the conduction electron diamagnetism. The shift due to core polarization

is indirect. In the absence of external field, the equal numbers of electrons spin in up states cancel the same amount of electrons with spin down. However, when there is an applied magnetic field the story is different. The conducting electrons introduce an "extra" effective field at the nuclear site, due to the spin orientations of the conduction electrons in the presence of an external field. Only s-character electrons will interact with the nucleus. The exchange interaction must be the reason for this core polarization field. The Knight shift due to core polarization hyperfine fields can also be negative because of the particular arrangement of the valence electrons.

Therefore the Knight shift can be utilized as an essential tool to investigate hyperfine field interaction of different kinds, and distinct the spin susceptibilities of various processes. I summurize the significant contributions to Knight shift by following equation

$$\mathbf{K_{tot}} = \mathbf{K_{orbital}} + \mathbf{K_{core}} + \mathbf{K_s}. \tag{4.20}$$

4.1.5 Dipole-Dipole Hamiltonian

The affect of magnetic dipole moment of one nucleus on another nucleus through space is called the dipolar coupling interaction and the Hamiltonian is written as

$$H_{DD} = -\frac{\mu_0}{4\pi}\frac{\gamma_1\gamma_2}{|\vec{r}|^3}\Big(\frac{3}{|\vec{r}|^2}\big(\vec{I_1}\cdot\vec{r}\big)\big(\vec{I_2}\cdot\vec{r}\big) - \big(\vec{I_1}\cdot\vec{I_2}\big)\Big) \tag{4.21}$$

where $\vec{r}$ is the distance between the two nuclei. This equation can be rewritten in a general form of

$$H_{DD} = \hat{I}_1 \cdot D \cdot \hat{I}_2. \tag{4.22}$$

In the PAS frame, D could be represented as a traceless and symmetric tensor as

$$D_{PAS} = -\frac{\mu_0}{2\pi}\frac{\gamma_1\gamma_2}{|\vec{r}|^3}\begin{pmatrix} -\frac{1}{2} & 0 & 0 \\ 0 & -\frac{1}{2} & 0 \\ 0 & 0 & 1 \end{pmatrix} \tag{4.23}$$

In the rotating frame explained in section (4.1.2), the dipolar Hamiltonian is expressed by

$$H_{DD} = -\frac{\mu_0}{4\pi}\frac{\gamma_1\gamma_2}{|\vec{r}|^3}\big(\hat{I}_{1z}\hat{I}_{2z} - \frac{1}{2}(\hat{I}_{1x}\hat{I}_{2x} + \hat{I}_{1y}\hat{I}_{2y})\big)\big(3\cos^2\theta - 1\big) \tag{4.24}$$

Where θ is the angle between two dipoles.

4.1.6 J-coupling Hamiltonian

The interaction of magnetic dipole moment of one nucleus on other one, mediated by electrons surrounding these nuclei is called the J-coupling or the scalar coupling. The Hamiltonian for this interaction is given by,

$$H_J = 2\pi\hat{\vec{I}}_1 \cdot \hat{J} \cdot \hat{\vec{I}}_2. \tag{4.25}$$

Where the tensor $\hat{J}$, in principle, has a set of isotropic and anisotropic elements.

4.1.7 Quadrupole Hamiltonian

Generally an atomic nucleus with spin I has its spin energy levels determined by the Zeeman term with the applied magnetic field B_0. However, atomic nuclei with $I \geqslant \frac{1}{2}$, in which the charges around the nucleus have a non spherical shape are also identified by the quadrupole moment Q of electric charges. This charge distribution interacts with the gradient of the electrostatic electric fields induced on the nucleus by the position of charges in the solid. Thus, the nuclear spin is affected by the quadrupolar Hamiltonian [139], which can be given by

$$H_Q = \frac{eQ}{2I(I-1)}\sum_j V_{jj}I_j^2. \tag{4.26}$$

In the above equation, V_{jj} are the second derivatives of the electric potential. V_{jj} could also be interpreted as electric field gradient (EFG) tensor which has $j = X, Y, Z$ as principle coordinates. In this coordinate system, the three quadrupolar frequencies are

$$\nu_j = \frac{3eQV_{jj}}{2I(I-1)h}. \tag{4.27}$$

These frequencies are linked by the Laplace equation

$$\frac{\partial^2 V}{\partial x^2} + \frac{\partial^2 V}{\partial y^2} + \frac{\partial^2 V}{\partial z^2} = \nu_x + \nu_y + \nu_z = 0. \tag{4.28}$$

Thus, generally two parameters are used. The quadrupolar frequency $\nu_Q = \nu_z$ associated with the largest principal axial element V_{zz} of the EFG matrix and the asymmetry parameter $\eta = \frac{V_{xx} - V_{yy}}{V_{zz}}$. Here we pick the principal axial values of EFG in the following order

$$||V_{zz}|| \geqslant ||V_{yy}|| \geqslant ||V_{xx}||. \tag{4.29}$$

In conclusion, figure (4.2) displays a comparative view of magnitude of effect of these Hamiltonians.

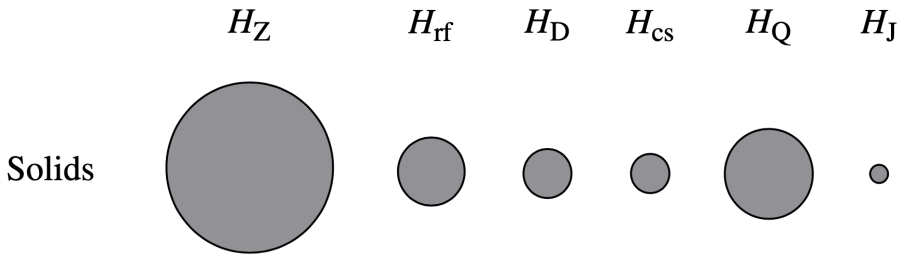

Figure 4.2: A semiquantitative comparison of the area between the magnitude effects of solid-state Hamiltonian magnitudes on NMR spectra. The plot is reprinted with permission from [8].

4.2 Relaxation Times

Despite the fact that the NMR spectroscopy is a completely quantum mechanical effect, using a classical picture is very convenient to display NMR relaxations processes. We begin the motion of a spin in an external magnetic field $\vec{B}_0$, assuming that $\vec{B}_0$ may possibly vary with time. $\vec{B}_0$ will produce a torque on the magnetic moment $\vec{\mu}$ of amount $\vec{\mu} \times \vec{B}_0$. This leads to the equation of motion

$$\frac{d\vec{\mu}}{dt} = \vec{\mu} \times (\gamma \vec{B}_0) \tag{4.30}$$

On the other hand, if we assume that the nucleus with magnetic moment $\vec{\mu}$ precessing around $\vec{B}_0$ with frequency $\vec{\Omega}$, the change in $\vec{\mu}$ will be

$$\frac{d\vec{\mu}}{dt} = \frac{\partial \vec{\mu}}{\partial t} + \vec{\Omega} \times \vec{\mu} \tag{4.31}$$

Combining equations (4.30) and (4.31), we get

$$\frac{\partial \vec{\mu}}{\partial t} = \vec{\mu} \times (\gamma \vec{B}_0 + \vec{\Omega}). \tag{4.32}$$

If we deliberately transfer to a reference frame that $\vec{\Omega} = -\gamma \vec{B}_0$, $\vec{\mu}$ remains fixed. The angular frequency $\gamma \vec{B}_0$ is the same "Larmor frequency" introduced in previous sections.

There are statistical ensembles of the nuclear magnetic dipole moments $\vec{\mu}_i$. The net magnetic dipole moment $\vec{M}$ of the ensemble of nuclear magnetic moments is the vector sum of the individual magnetic moments, i.e. $\vec{M} = \sum_i \vec{\mu}_i$. Due to cancellation of the randomly distributed x and y elements of the individual magnetic moments of nuclei, the net magnetization vector in equilbrium is aligned with the laboratory z axis as shown in Figure (4.3).

The dynamics of the net magnetization $\vec{M}$ in the presence of the applied magnetic field is expressed by the equation

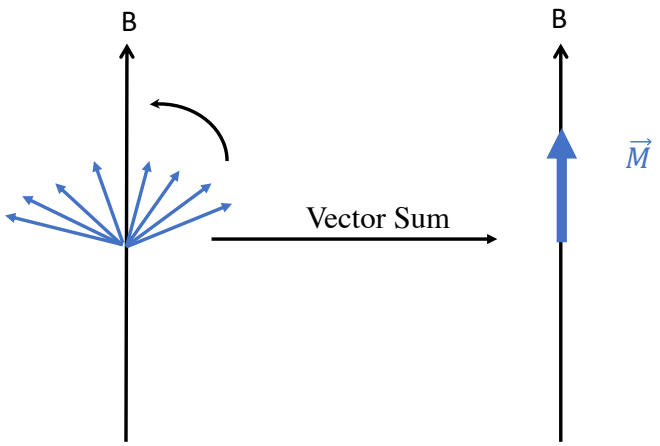

Figure 4.3: The classical net magnetization vector of randomly distributed magnetic moments exhibited in an external magnetic filed B.

$$\frac{d\vec{M}}{dt} = \gamma\vec{M} \times \vec{B}_{tot} - \hat{R}\big(\vec{M} - \vec{M}_0\big) \tag{4.33}$$

where $\vec{M}$ is the instantaneous net magnetization for the ensemble spins, $\vec{M}_0$ is the equilibrium net magnetic moment aligned with the laboratory frame,$\vec{B}_{tot} = \vec{B}_0 + \vec{B}_{rf}$ and $\hat{R}$ is given by

$$\hat{R} = \begin{pmatrix} \frac{1}{T_2} & 0 & 0 \\ 0 & \frac{1}{T_2} & 0 \\ 0 & 0 & \frac{1}{T_1} \end{pmatrix}. \tag{4.34}$$

In the above equation, T_1 called the spin-lattice relaxation time (or longitudinal relaxation time), and T_2 is the spin-spin relaxation time (or transverse relaxation time) associated with the portion of $\vec{M}$ in the xy-plane. T_1 relaxation reduces out of equilibrium component by transferring spin energy to the phonons or conduction electrons (the lattice). In comparison, T_2 indicates rotation of spins in an applied magnetic field B and conserves the energy. Furthermore, T_2 associates with the dephasing of the spin. Later, we will explore the other processes including the Gaussian decay.

5. EXPERIMENTAL APPARATUS

5.1 NMR Setup and Data Analysis

The NMR results provided in this dissertation were generated from a home-built NMR machine made by Dr. Ross and previous students providing fixed magnetic field near 9 T. This machine is a pulsed NMR spectrometer with a superconducting magnet that includes a sample cryostat. The superconducting material of current magnets is composed of niobium-titanium with T_C= 10 K. The cryostat setup embodies a wide bore liquid helium vessel that is thermally shielded by a liquid nitrogen reservoir which is sandwiched among two vacuum layers. This setup ensures that the targeted samples can kept a range of temperatures from 4.2 up to 500 K.

A tube containing the sample was wrapped in a conducting coil, made out of silver for the Cu NMR experiment discussed here, and other elements were used to deploy the spin-echo sequence and to collect the result signal at designated frequency. The coil is enclosed in a probe and then lowered into the bottom of vessel where it is placed in the bore of the shielded superconducting magnet. NMR experiments were done from 450 K down to 4.2 K.

To employ the spin-echo sequence and obtain the echo signal collected by the coil, the probe containing the sample is connected to an electronic setup. In order to enhance signal transfer to the probe, the coil is designed to be in a resonating RLC circuit which enables tuning through two variable, along with fixed capacitors. With this method, the resonance could be maintained while the frequency is changed. The variable capacitors incorporated into the cryostat and can be effectively adjusted down to 4.2 K.

5.1.1 Electronic Hardware

An overall schematic figure of the electronic hardware utilized to observe the signals is illustrated in figure (5.1). The NMR electronics have been well documented with details in [9]. The NMR electronic setup consists of two primary parts: a transmitter and a receiver, as denoted by two separate colors in figure (5.1). The transmitter sends the RF-pulses to the collecting coil sig-

nals. It contains a frequency synthesizer, a power amplifier, and a pulse sequence generator (PSG). The transmitter can set B_1, discussed in section (4.1.2), in the along the rotating axis $\pm x'$ and $\pm y'$ directions within pulse phase circuitry. The setup works in 100 to 1000 watt range of power.

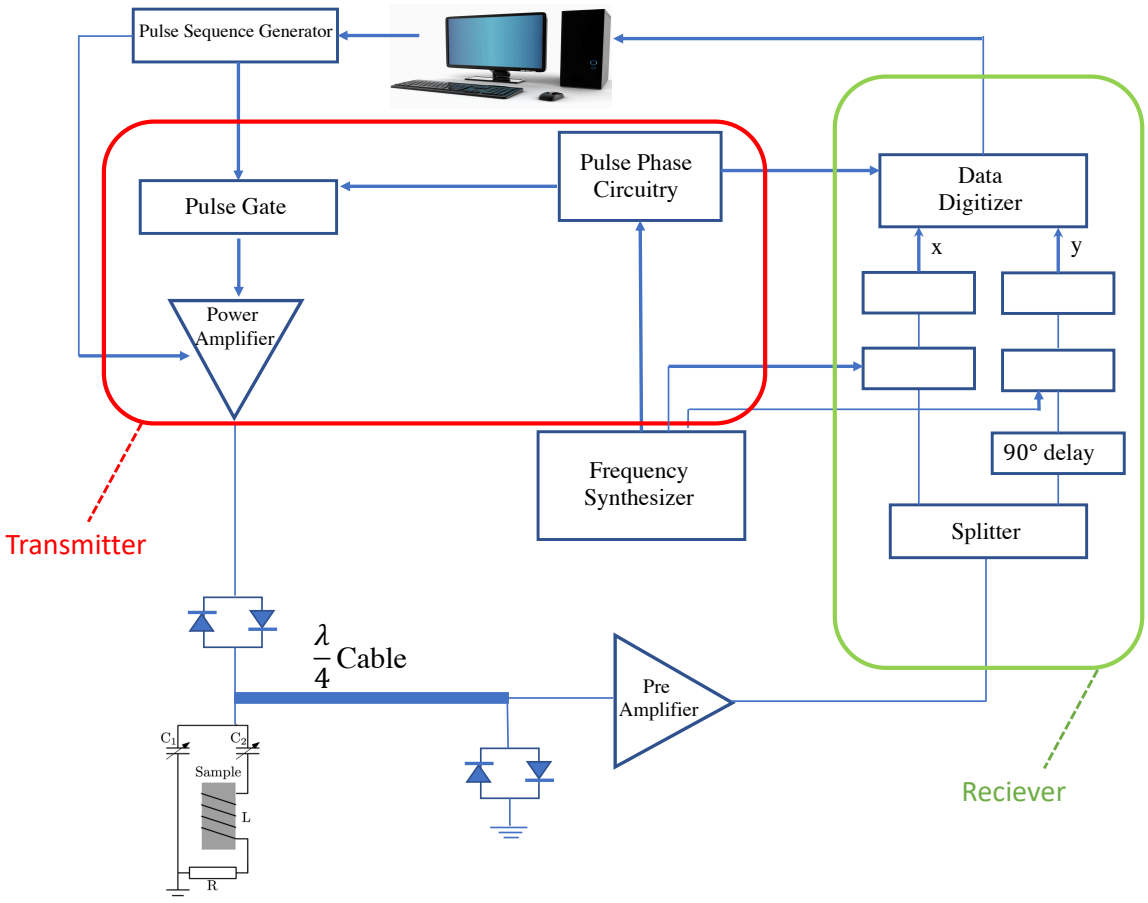

Figure 5.1: A block diagram schematic of the NMR signal electronics. Modified version of figure displayed in [9]

The receiver, shown in the green box in figure 5.1, receives the amplified (through series of pre-

amplifiers) microvolt signals collected from the coil. Then, in order to eliminate the RF-signals, a quadrature detection is implemented. In this detection setup, the collected signal is separated into X and Y channels. The Y channel is delayed by 90°. Next, the two channel signals and the reference frequency are mixed and transferred to a low pass filter. At the end, more amplifiers are utilized to enhance the signal to the digitizer level.

To perform NMR spectroscopy at various frequencies, one must adjusted the calibrated RLC circuit in order to attain the desired resonant frequency. A discussion of the impedance matching principle utilized is given in Appendix A.

5.2 Materials Characterization

5.2.1 XRD

Powder X-ray diffraction (XRD) is a fast analytical method mainly employed for phase determination of a crystalline material which provides detailed information about unit cell magnitudes. The studied material is finely ground to determine the crystal parameters.

I performed powder X-ray diffraction at room temperature with a Bruker D8 X-ray Powder Diffractometer available in Department of Chemistry, a shared facility, and performed Rietveld refinement by GSAS-2 [140] software.

Figure 5.2 shows a schematic view of how XRD works.

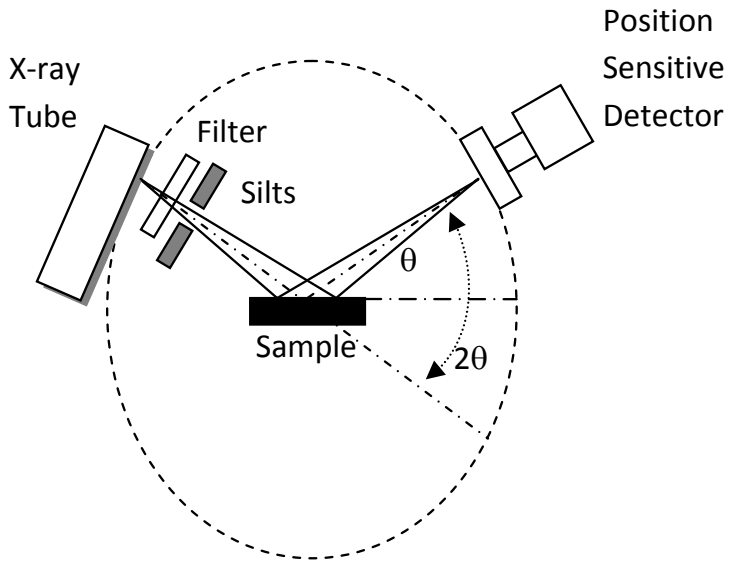

Figure 5.2: A schematic view of a Bragg X-ray powder diffractometer

5.2.2 WDS

The unique potential of an electron probe is the capacity to identify the composition of materials by implementing wavelength dispersive spectroscopy (WDS). With this technique, various materials including minerals, powders, thin films, and metals/alloys can be evaluated.

WDS experiments were carried out on various samples in a Cameca SX5 Electron Microprobe at Texas A&M University is located in the Materials Characterization Facility (MCF).

6. EXPERIMENTAL RESULTS AND DISCUSSION FOR $Cu_{12}Sb_4S_{13}$*

In this chapter, I report NMR spectra and relaxation times relating to Cu atom viberation in $Cu_{12}Sb_4S_{13}$ tetrahedrite. We show that a two-phonon Raman process involving strongly anharmonic local vibrational modes dominates the NMR quadrupolar relaxation. A one dimensional anharmonic potential is presented to model the anharmonic local oscillators providing a measure of the dynamical atom displacements. Most of this chapter was published in an article in the journal ACS Applied Materials & Interfaces under the title of *Structure Change and Rattling Dynamics in $Cu_{12}Sb_4S_{13}$ Tetrahedrite: an NMR Study*" [2] and reproduced with permission.

6.1 Experiment

6.1.1 Sample preparation and characterization

Sample synthesis was carried out by our collaborator Dr. Xu Lu from Chongqing University. A polycrystalline sample of tetrahedrite was synthesized by conventional solid state reaction. High purity elements ($> 99.99\%$) weighed according to the stoichiometric ratio were sealed in quartz ampoules under a vacuum of $\sim 6.5 \times 10^{-4}$ mbar. The sealed quartz tubes were firstly heated to 923 K at a rate of 0.3 K min^{-1} and kept at that temperature for 12 h before cooling to room temperature at 0.4 K min^{-1}. The ingots obtained were ground into fine powders and then cold pressed into pellets. The resulting pellets were further annealed at 723 K for a week in order to improve homogeneity. The annealed products were re-ground into fine powders for sintering. The final products were consolidated by the spark plasma sintering (SPS-625) system at 673 K for 5 minutes under a uniaxial pressure of 45 MPa.

An electron microprobe experiment was performed implementing wavelength dispersive spectrometry (WDS) on a Cameca SXFive armed with wavelength dispersive X-ray spectrometers to test composition. Measuring at 10 locations, we obtained a mean composition of $Cu_{11.91}Sb_{3.95}S_{13}$,

*Part of this section is reprinted with permission from N. Ghassemi, X. Lu, Y. Tian, E. Conant, Y. Yan, X. Zhou, and J. H. Ross Jr, "*Structure Change and Rattling Dynamics in $Cu_{12}Sb_4S_{13}$ Tetrahedrite: an NMR Study,*" ACS applied materials & interfaces, vol. 10, no. 42, pp. 36010-36017, 2018. Copyright (2018) American Chemical Society.

with statistical fluctuation corresponding to less than 1% relative uncertainty in these values. Systematic uncertainties for this instrument are also on order of 1%.

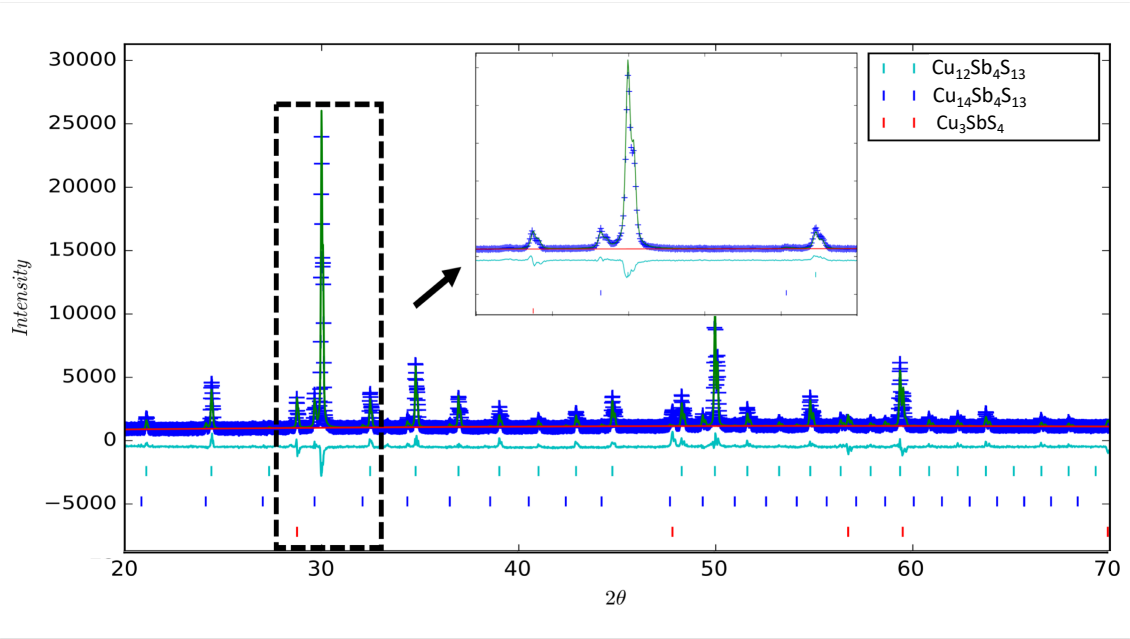

Figure 6.1: X-ray powder diffraction data for tetrahedrite sample (blue crosses), with refined curve (green) and difference plot. In the inset, the most intense peak is $Cu_{12}Sb_4S_{13}$ phase; small satellite at 29.8° and 29.8° due to $Cu_{14}Sb_4S_{13}$ and Cu_3SbS_4 phases, respectively. Reprinted with permission from [2]

Crystal structural characterization was performed with powder X-ray diffraction (XRD) using a Bruker D8 diffractometer with CuKα radiation. GSAS II software was implemented for Rietveld refinement [140]. Tetrahedrite samples are known[105, 141] to segregate into regions of Cu-rich $Cu_{14}Sb_4S_{13}$ tetrahedrite (Cu_{14}) in addition to $Cu_{12}Sb_4S_{13}$ and the XRD results showed a small second Cu_{14} phase in addition to the main phase, with refinement indicating a Cu_{14} phase fraction of 8.7%, with the the small amount of Cu_3SbS_4 phase [121] seen in XRD. Cu_3SbS_4 was also seen in WDS. In agreement with reported results [105, 141] the fitted Cu_{12} and Cu_{14} lattice constants are 10.3246 Å and 10.4458 Å respectively and the Cu_3SbS_4 phase has a lattice consisting of a tetragonal unit cell containing 8 atoms in 121($I\bar{4}2m$) space group with a=5.391 Å and c= 10.764

		Cu12 phase				Cu14 phase			
Site	WP [a]	x	y	z	SOF [b]	x	y	z	SOF
Cu I	12d	0.5	0	0.25	1	0.5	0	0.25	1
Cu II	12e	0	0	0.2173	1	0	0	0.215	1
Cu III	24g	–	–	–	–	0.2885	0.2885	0.0054	0.082
Sb	8c	0.2687	0.2687	0.268	1	0.2664	0.2664	0.2664	1
S I	24g	0.884	0.884	0.3623	1	0.1149	0.1149	0.3603	1
S II	2a	0	0	0	1	0	0	0	1

Table 6.1: Atomic parameters in the refinement of $Cu_{12}Sb_4S_{13}$ and $Cu_{14}Sb_4S_{13}$ at room temperature. Both structures cubic space group I-43 (# 217), with lattice constant a =10.3246 Å for $Cu_{12}Sb_4S_{13}$ and 10.4458 Å for $Cu_{14}Sb_4S_{13}$. [a] Wyckoff Position. [b]SOF: site occupancy factor. $R_W = 7.88\%$.

Å. Based on the WDS measurement, we estimated that there is 5% of this phase. $Cu_{14}Sb_4S_{13}$ has the same space group and a set of atomic positions nearly equivalent to those of $Cu_{12}Sb_4S_{13}$, with the addition of a small-occupation Cu interstitial (Cu-III) which provides charge balance and thus expected insulating behavior along with eliminating the metal-insulator transition in this phase. More discussion of the $Cu_{14}Sb_4S_{13}$ phase is found in the next chapter. The Cu_3SbS_4 phase has an XRD peak at an angle very close to Si crystal and initially assumed to be impurity due to the Si structure. However further DFT calculations directed us to the existence of this phase. Figure 6.1 shows the result, with fitting details given in Table 6.1. For the minority Cu_{14} phase, the atomic positions are close to those reported in ref. 141, with small differences especially for Cu-III. For the fit, we assumed full site occupation of the tetrahedrite sites (except for Cu-III) due to relatively low sensitivity to these parameters.

6.1.2 Measurement methods

A custom-made pulse spectrometer as explained in section (5.1), was used to conduct NMR experiments in a constant magnetic field of 8.9 T in a temperature range from 4.2 to 295 K using a multitemperature detecting probe. CuCl was utilized as the NMR shift standard for ^{63}Cu and ^{65}Cu spectra. NMR measurements employed spin echo integration vs frequency and fast Fourier transformation (FFT), with the NMR spectra obtained by assembling and superposing FFT spectra at a sequence of frequencies.

NMR spin-lattice relaxation time (T_1) measurements were obtained based on an inversion recovery sequence implementing a multi-exponential function for recovery of the central transition[142]. For magnetic shift contributions, we follow the convention $K = (f - f_0)/f_0$ for Knight shifts, with f_0 the standard reference frequency and positive shifts having paramagnetic sign. In the analysis, we used nuclear moment values (Q and γ) reported in ref. 143. The ^{63}Cu and ^{65}Cu gyromagnetic ratios γ and quadrupole moments Q used are as follows: $^{63}\gamma$ = 7.1118 rad/s G^{-1}, $^{65}\gamma$ = 7.6044 rad/s G^{-1} , ^{63}Q = -22.0 fm^2, ^{65}Q = -20.4 fm^2. Electric field gradients (EFGs) are given in terms of the standard parameters $\nu_Q = \frac{3eQV_{zz}}{2I(2I-1)h}$ and $\eta = (V_{xx} - V_{yy})/V_{zz}$.

6.2 NMR Lineshape

The NMR resonance signal for lineshape is affected by various parameters. Given an ensemble of spins placed in a non-homogenous magnetic field, the Larmor frequency signals in the lineshape will be broaden due to inhomogeneity of magnetic field in the ensemble. Figure 6.2 shows the ^{63}Cu room temperature line shape. Since $Cu_{12}Sb_4S_{13}$ was shown not to have a NMR signal at room temperature, the spectrum displayed in figure (6.2) is attributed to the Cu_3SbS_4 phase. The disappearance of the $Cu_{12}Sb_4S_{13}$ phase signal is due to Cu-ion motion as described later.

For ^{63}Cu which has $I > \frac{1}{2}$, interaction between the EFG and the nuclear quadrupole moment will split the energy levels. This kind of quadrupole interaction will impact the central transition in the NMR spectrum. On the other hand, in general, the interaction between electron and nuclear dipoles will lead to an anisotropic Knight shift which occurs typically once the symmetry at the nucleus is less than cubic symmetry. This results in a number of frequency shifts based on orientation of the sample and gives rise to spread of the NMR signal into a powder line shape. In the case that none of mentioned interactions occur, the line shape is expected to have a characteristic broadening which gives a direct information about the local field seen by nucleus.

The room temperature line shape for the powder sample has seven peaks. These are edge singularities of quadrupole-broadened powder patterns, and the results were fitted as a superposition of two sites.

Fitting of the spectra was performed using the Quadfit package [144], and with a custom NMR-

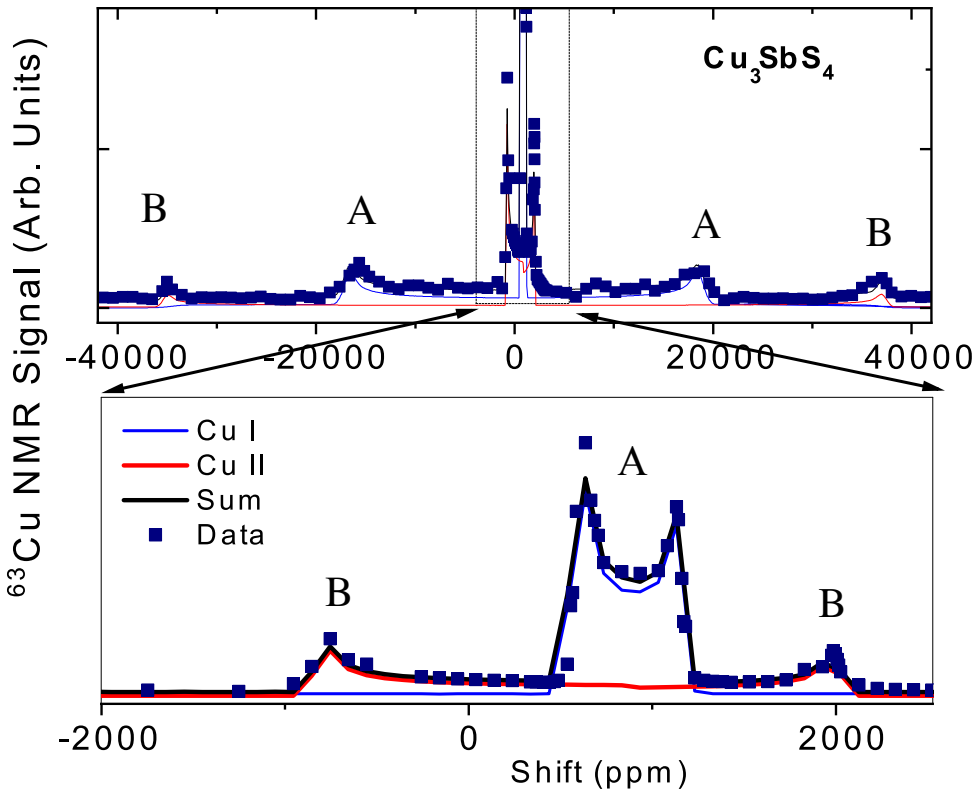

Figure 6.2: ^{63}Cu NMR line shape for the sample including $Cu_{12}Sb_4S_{13}$ and Cu_3SbS_4 phases, measured at room temperature. The inset shows the $I_z = +1/2$ to $-1/2$ central transitions while the satellite transitions can be observed in the wider spectrum. The solid curve corresponds to the two site fitting described in text.

line-shape code from our lab. Data were also taken using FFT methods for greater detail (shown in figure 6.3 along with lower-temperature data), and by spin-echo integration with smaller H_1 alternating field (Figure 6.2) for better resolution of the relative intensities.

The Cu_3SbS_4 phase has two Cu sites with two to one occupation ratio, these are denoted as site A and B, respectively. Fitting the latter measurements gave spectral areas differing by about 24% for the two fitted sites in Cu_3SbS_4 phase, due apparently to an enhanced broadening of the edge singularities of site B giving some deviation from the fit. These are reasonably consistent with two to one site occupation with the difference assumed to be due to T_2 difference.

Site A (site assignment described below) exhibits the two outer satellite transitions ($m_z = \pm 3/2 \leftrightarrow \pm 1/2$), in the upper plot of figure 6.2, as well as the central transition ($m_z = 1/2 \leftrightarrow$

$-1/2$) edge peaks near 700 and 1100 ppm. This site was fitted with quadrupole parameters $\nu_Q = 3.6$ MHz and $\eta = 0$, magnetic shift $K_{iso} = 970$ ppm, and a small axial magnetic shift anisotropy $\delta = K_{\parallel} - K_{\perp} = +141$ ppm, where the principal values are parallel and perpendicular to the symmetry axis, respectively.

Note that the satellite peaks at -18000 and 19000 ppm provide a very good match to the central transition in this fit and that there is no sign in this range of a second-order spectrum for $\nu_Q \approx 18$ MHz as observed at lower temperatures[10] and associated with $Cu_{12}Sb_4S_{13}$. Thus, we see that the $Cu_{12}Sb_4S_{13}$ line shape is not present due to the motion of the Cu ions. The site B exhibits the outer singularities seen in both plots of figure 6.2. These were fitted with $\nu_Q = 7.3$ MHz, K_{iso} = 970 ppm, and a small axial shift anisotropy of $\delta = -145$ ppm, with $\eta = 0$.

Given that two sites with $\nu_Q \approx 3.85$ MHz and $\nu_Q \approx 7.59$ MHz were identified at room temperature, we completed a DFT calculation for the Cu_3SbS_4 compound. The result shows that the Cu sites have computed values of $\nu_Q \approx 3.64$ MHz and $\nu_Q \approx 6.59$ MHz with $\eta = 0$ for both cases. These are scaled down with respect to observed values but within the range of what is expected for such calculations [132]. This confirms the existence of this phase in our sample. Further evidence of Cu_3SbS_4 phase is found in the reflection due to small amount of this phase in the XRD results figure (6.1). Therefore, we conclude the presence of Cu_3SbS_4 in this sample explains the presence of the small peaks at room temperature. In fact, it has been reported that the pure $Cu_{12}Sb_4S_{13}$ phase does not have a room temperature signal [145, 146] which now we understand to be due to motion of the ions. At low temperatures, the spectral weights are significantly enhanced below 150 K, which addresses the dominance of the $Cu_{12}Sb_4S_{13}$ phase signal.

Figure 6.3 displays the central part of the ^{63}Cu NMR lineshapes at three temperatures. As seen in the figure the $Cu_{12}Sb_4S_{13}$ shift starts at about 650 ppm and becomes more positive as temperature decreases below the MIT, matching the previously reported [10] Knight shift changes for $Cu_{12}Sb_4S_{13}$. Figure 6.4 shows the more detailed changes versus temperature approaching the phase transition. There is a gradual lineshape change below about 200 K, as $Cu_{12}Sb_4S_{13}$ becomes visible then near $T = 88$ K the lineshape suffers an abrupt change at the position of the MIT [85] in

synthetic $Cu_{12}Sb_4S_{13}$. Over the same range a peak centered at about -700 ppm appears. However, this resonance disappears at 4 K and we could not further analyze these changes.

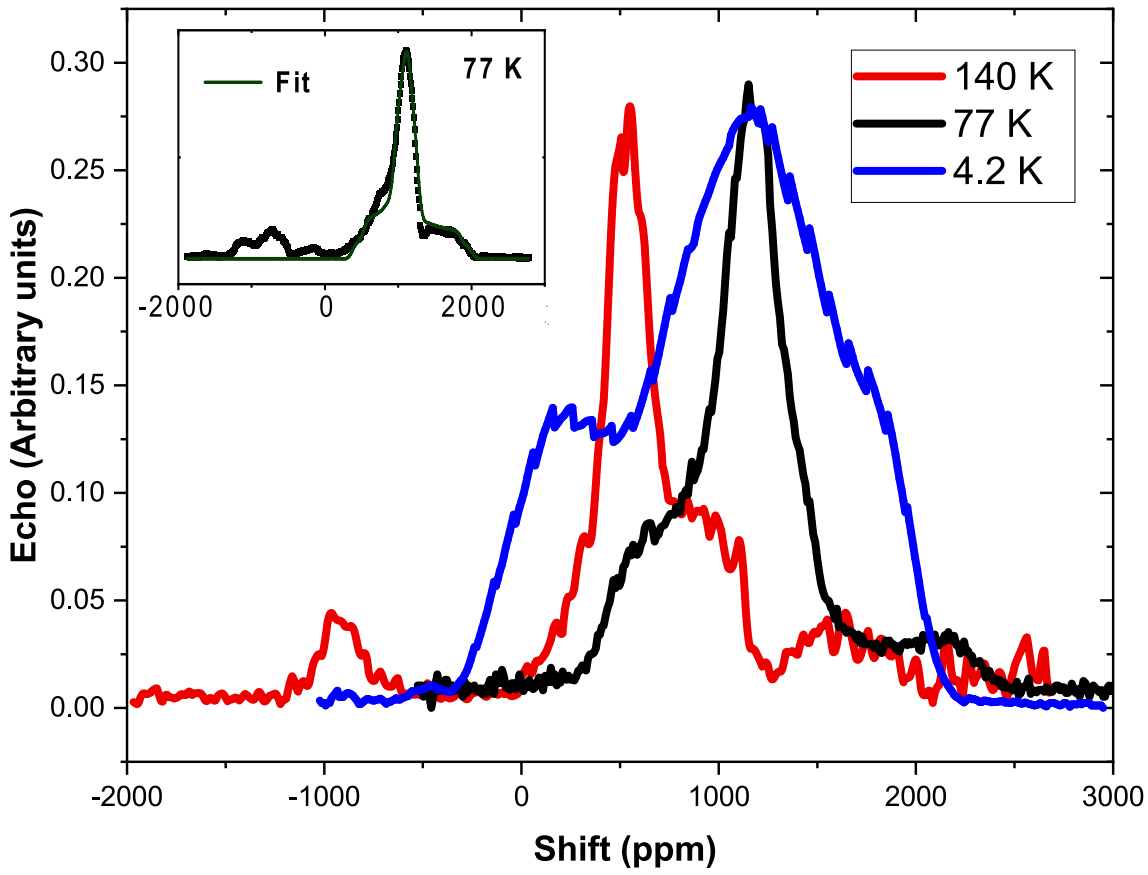

Figure 6.3: Central region of ^{63}Cu NMR line shapes at temperatures of 4.2 K, 77 K, and 140 K. Line shapes have been scaled for convenience to give comparable intensities.

6.3 $Cu_{12}Sb_4S_{13}$ Spectrum

Below T_c the parameters ν_Q= 75 kHz, $\eta = 1$, along with $\delta = 225$ ppm and $\eta = 1$, provide a good model for the 77 K data (inset, figure 6.3). With these parameters, the 77 K signal above 1300 ppm is a satellite resonance, and the measured 77 K T_1 (0.20 s at 1700 ppm vs. 0.27 s at the peak position) is also consistent with this assignment, given that for a quadrupole mechanism, which dominates, as discussed below, the central transition T_1 exceeds that of the satellites [147] as observed here.

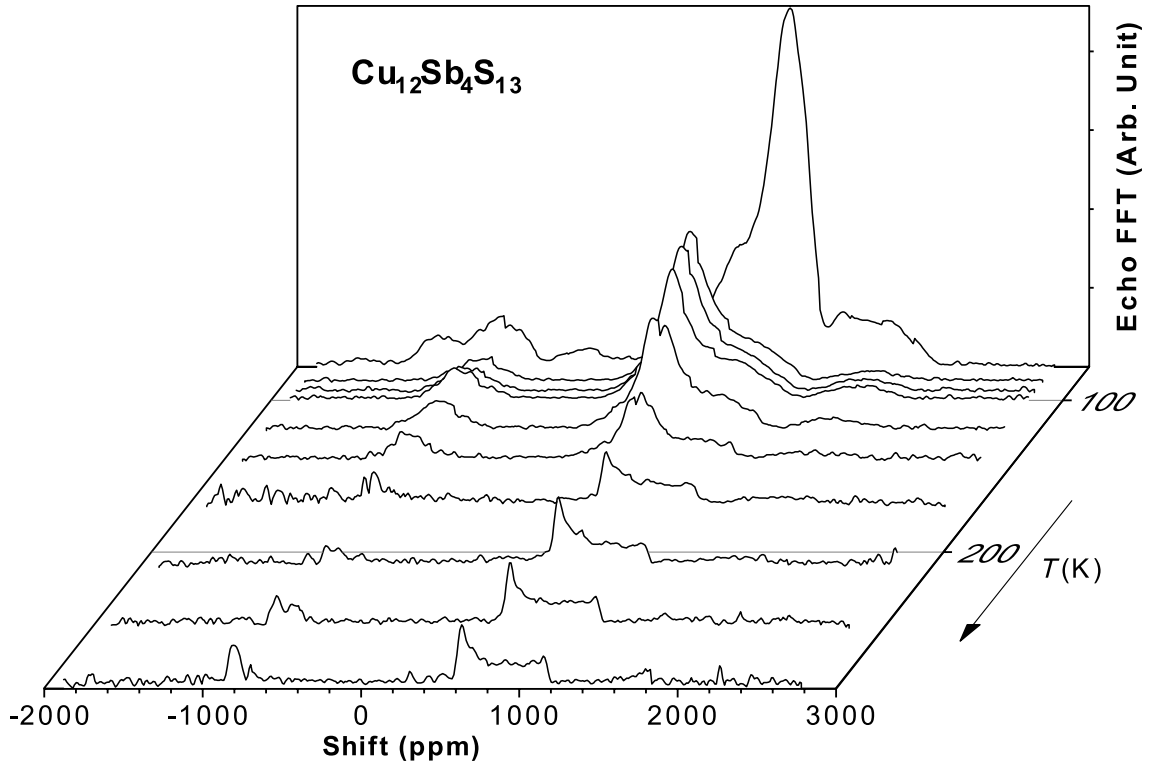

Figure 6.4: ^{63}Cu NMR line shapes plotted at different temperatures. Signals are scaled by factor T to preserve the spectral intensity.

Figure 6.5 shows the most intense peak position versus temperature, along with its center of gravity (c.g.) position. At room temperature, the Cu_3SbS_4 phase c.g. is 120 ppm below the fitted isotropic K = 970 ppm due to the second-order quadrupole contribution, which adds a negative shift [142]. Below about 150 K, the resonance is due to $Cu_{12}Sb_4S_{13}$ phase. At intermediate temperatures the c.g. and peak position are very similar due to a small EFG, while at 4 K the spectrum develops considerable asymmetry, so the peak position and c.g. are again shown separately. The spectra observed here is understood to be the Cu-I structure site, with Cu-II believed to have a very large EFG [148, 10]. The Cu-I peak positions are the same as those of Kitagawa et al. [10], over the temperature range previously reported, and this can be seen in figure 6.5. The large jump at T_c is a Knight shift change, connected [10] to a large spin susceptibility change in the MST. At higher temperatures the Cu-I peak merges with what becomes the lower edge of the Cu_3SbS_4 phase.

In measurements between T_c and 120 K a second site was also observed [10] with $\nu_Q = 18.6$

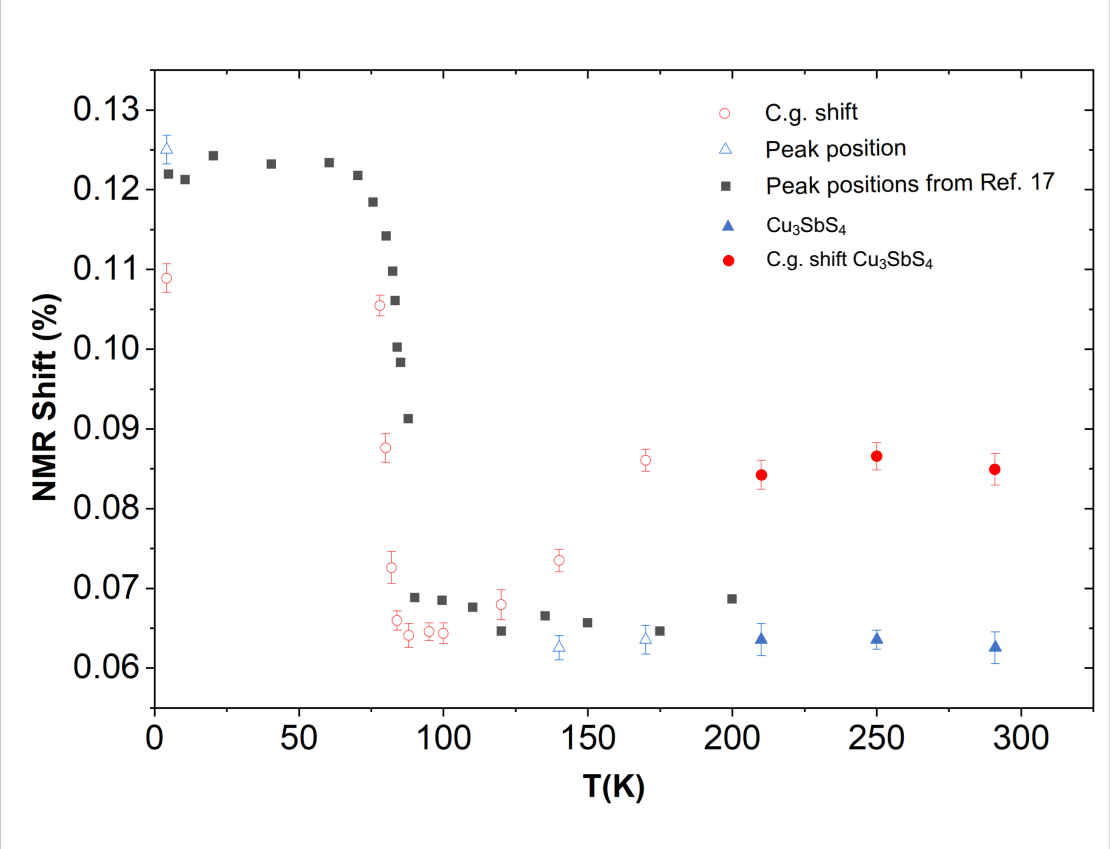

Figure 6.5: Position of most intense spectral peak, and center of gravity position (C.G), for ^{63}Cu resonance of Cu-I, and comparison to data taken from Ref. 10

MHz. As previously reported, the $\nu_Q = 18.6$ MHz resonance also becomes very broad and difficult to observe at low temperatures [10]. Note also that Bastow et al. [148] observed site II with $\nu_Q \approx 20$ MHz at room temperature, but in a naturally-occurring tetrahedrite sample, in which, due to heavy substitution the structural transformation and MST, would not be expected to occur.

In unsubstituted $Cu_{12}Sb_4S_{13}$, previously reported resistivity measurements have exhibited an unidentified feature at about 200 K [149, 114], and now we assume that the line-shape changes we observe in this temperature range due to Cu-ion motion are also related to these observed features. A gradual softening of the elastic constants is also observed between room temperature and the MST [150], presumably related to ion dynamics.

6.4 DFT Results

Ab initio density functional theory (DFT) simulations were conducted using WIEN2K[132], applying the projector augmented wave (L)APW method and the Perdew-Becke-Ernzerhof (PBE) exchange-correlation functional. A cubic 58 atom unit cell of $Cu_{12}Sb_4S_{13}$ in the ordered configuration of figure 2.1 with Cu at Wyckoff sites (12d) and (12e), S at (2a) and (24g), and Sb at (8c) was investigated, using a 1000 k-point mesh and a plane wave cutoff of 100 eV. For a fixed lattice constant of 10.306 Å, corresponding to the 100 K experimental value[151], the atomic positions were relaxed.

For Cu_3SbS_4, we used the structure reported by Pfitzer [128] which includes a tetragonal unit cell of 8 atoms in $121(I\bar{4}2)$ space group with $a = 5.391\,\text{Å}$ and $c = 10.764\,\text{Å}$. The calculation initialized with $RK_{max} = 6$, the plane-wave expansion cutoff of $G_{max} = 12$ Bohr^{-1} and $10 \times 10 \times 10$ k-points considered with the PBE (Perdew, Burke, and Ernzerhof) exchange correlation function, without spin polarization or spin orbit coupling. Our calculated band gap is 0.054 eV which is in good agreement with recently reported calculations 0.045 eV [152]. However, note that it was recently shown [153] that using more advanced functionals yields a larger semiconducting gap for this material. However, this is unlikely to have a large effect on calculated electric field gradients (EFGs), which depend only on the filled states within the valence band. The EFG results for the two Cu sites in this material, site A and site B, are 2.85318×10^{21} (V/m^2) and -1.46966×10^{21} (V/m^2) respectively, quoted as the largest-magnitude principal values of the EFG tensors, which are symmetry-constrained to be axial in both cases. Converting to the standard quadrupole parameter $\nu_Q = \frac{3eQV_{zz}}{2I(2I-1)h}$, based on the standard ^{63}Cu quadrupole moment [143], we obtain $\nu_Q = 6.59$ MHz and $\nu_Q = 3.64$ MHz respectively with $\eta = 0$ for both nuclei. There are in a good agreement with the $\nu_Q = 7.59$ MHz and $\nu_Q = 3.85$ MHz obtained from fitted curve to the room temperature line shape. The band structure and DOS of Cu_3SbS_4 phase is provided in figure 6.6.

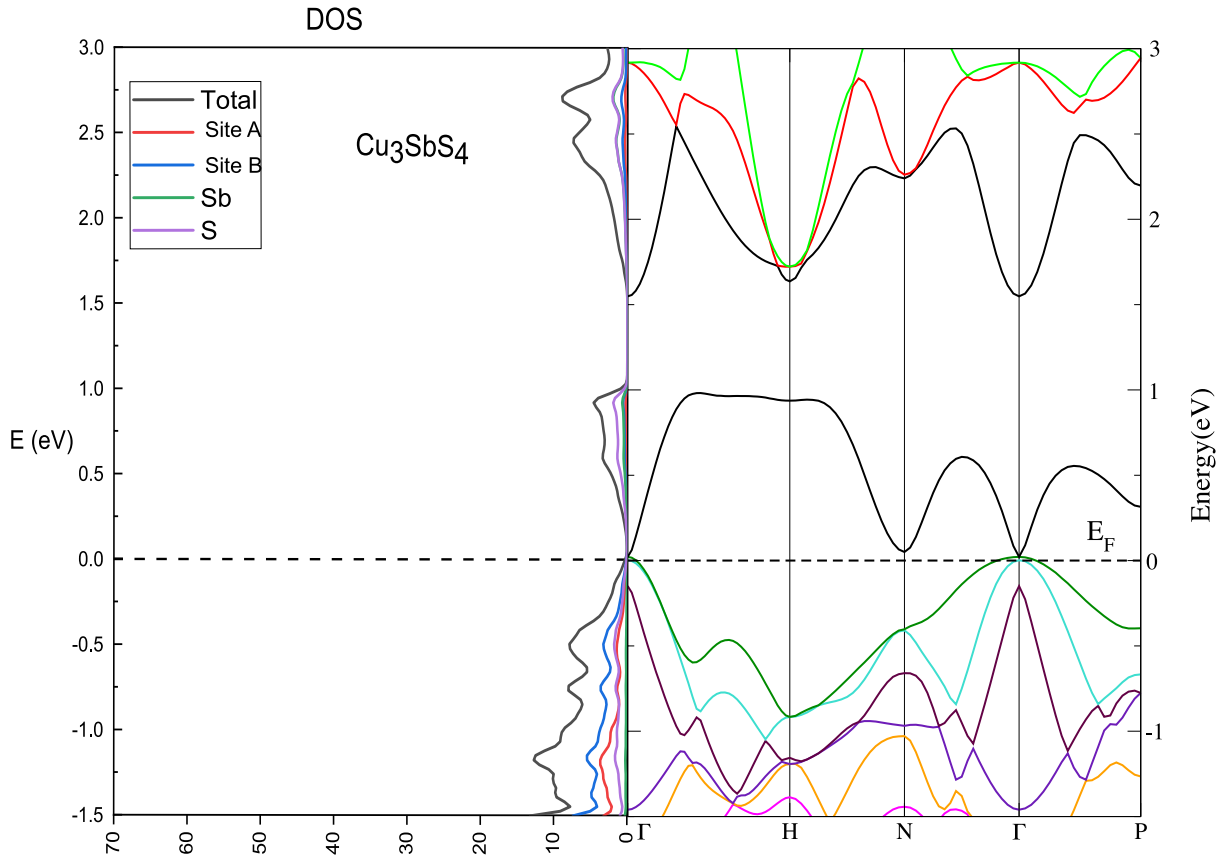

Figure 6.6: Density of states and energy-band diagram for Cu_3SbS_4 along high symmetry lines in the BZ.

The results of the $Cu_{12}Sb_4S_{13}$ electronic structure derived by DFT calculation is shown in figure (6.7). $Cu_{12}Sb_4S_{13}$ appears to be in a metallic state where the Fermi energy sits close to a sharp peak in DOS above the valence band, and a semiconducting gap (1.1eV) splits the conduction bands from the valence bands. The valence bands are mainly due to hybridization of sulfur 3p and copper 3d orbitals.

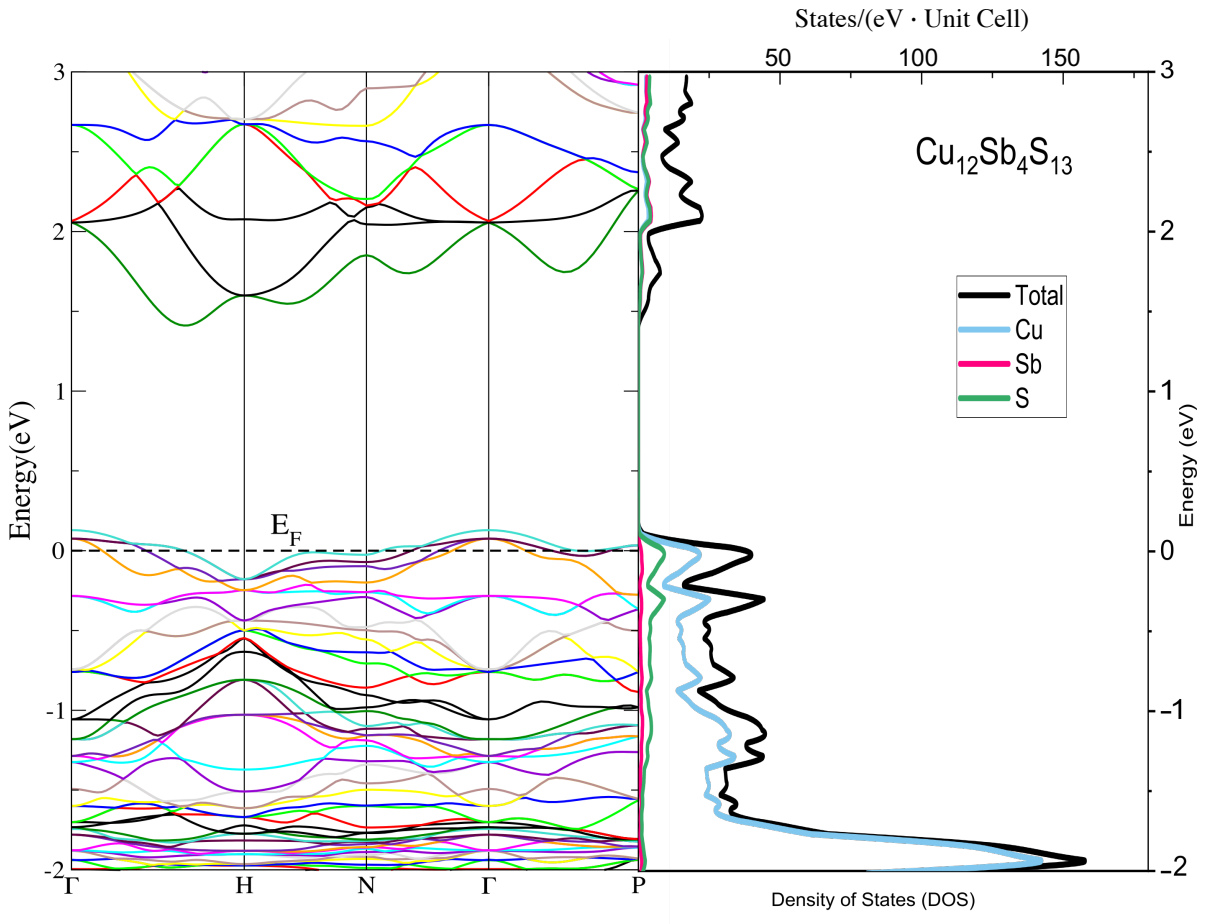

Figure 6.7: Calculated electronic band structure and density of states for $Cu_{12}Sb_4S_{13}$.

The results show that the Fermi level is in the valence band as expected for $Cu_{12}Sb_4S_{13}$, indicating p-type conduction for this composition, with band-structure agreeing with previous results [3]. The calculated EFG provides help in further understanding the experimental results, as well as measuring the charge anisotropy close to the nucleus. EFG results using the WIEN2K code[154], for the two Cu sites are $\nu_Q = 0.3$ and 17 MHz, with $\eta = 0$ and $\eta = 0.15$ respectively. These are consistent with the values observed just above T_c in the pure tetrahedrite[10] and at ambient temperature in natural tetrahedrite[148]. We also see reduced EFG close to T_c and the computational results thus serve to reinforce the analysis showing that the spectrum near T_c corresponds to the undistorted structure.

6.5 Spin Lattice Relaxation

The most intense central transition peak was chosen to carry out NMR relaxation measurements. This was done for ^{65}Cu as well, with spectra for both nuclei showing similar features. The T_1 was fitted by a standard multiexponential function for magnetic recovery of the central transition [155]. For spin $3/2$, this function is $\frac{M(t)}{M(0)} = A + \frac{1}{5}e^{(t/T_1)} + \frac{9}{5}e^{(6t/T_1)}$. Using a different function for quadrupole relaxation would lead to an overall scaling of the T_1 which does not affect the fitting parameters described below. We also fitted the same function including stretched exponentials, but found that the ordinary exponential provided the better fit. The resulting rates can be seen in figure 6.8, where the data above the 150 K corresponds to the Cu_3SbS_4 phase. There is a relatively broad jump in $1/T_1$ at around 88 K due to the MST [151]. In addition, a peak can also be observed at a temperature around 12 K for both nuclei.

The isotopic ratio $^{63}T_1/^{65}T_1$, shown in figure 6.9, is uniform and stable over a large temperature range and approaching to the quadrupole moment ratio $(Q_{65}/Q_{63})^2 = (20.4/22.0)^2 = 0.86$. Within the framework of relaxation[156, 139] theory, this indicates a quadrupole mechanism. Spin or other magnetic fluctuations will lead instead to a ratio determined by gyromagnetic ratios, also shown in the figure. The quadrupole process is an indication of a lattice vibrations or atomic fluctuations as the dominant mechanism.

As the temperature increases, T_1T becomes constant, a situation usually indicative of Korringa-like conduction electron relaxation[156, 157], while phonon processes normally lead to a T^2 or higher temperature dependence of $1/T_1$. By contrast, the quadrupole-dominated $T_1T \sim$ constant behavior is a result that has been shown[158] to result from strongly anharmonic local-oscillator behavior. It is interesting that this extends to the Cu_3SbS_4 phase and the values are almost identical. The peak at the low temperatures is also characteristic of such behavior. This is interrupted by an additional maximum in the relaxation rate appearing near the MST T_c, due to the slowing down of fluctuations often accompanying a phase transformation, for example as typically observed in incommensurate charge density wave systems[159].

Assuming additive quadrupole and magnetic contributions to the relaxation process, in order

to further analyze we separated them by assuming [155, 160] $\frac{1}{T_1} = \frac{1}{T_{1Q}} + \frac{1}{T_{1M}}$ with $(T_{1M})^{-1} \propto \gamma^2$ and[156] $(T_{1Q})^{-1} \propto Q^2$, where T_{1Q} and T_{1M} indicate the quadrupole and magnetic contributions. This separation is an approximation, since the two relaxation functions differ somewhat, however since the quadrupole process dominates for the entire temperature range, the correction is small, and using the fitted T_1 without separation gives results which are nearly identical to those obtained by this procedure.

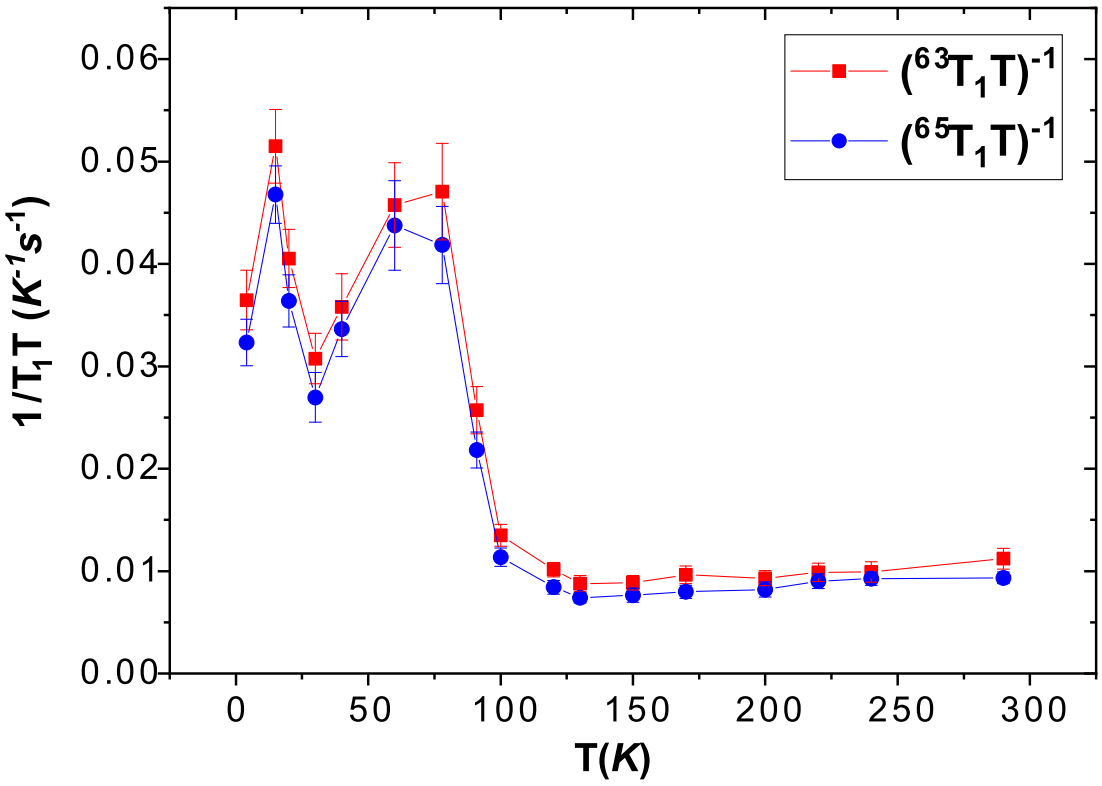

Figure 6.8: ^{63}Cu and ^{65}Cu NMR spin-lattice relaxation rates at the most intense position of the central transition from 4.2 to 295 K

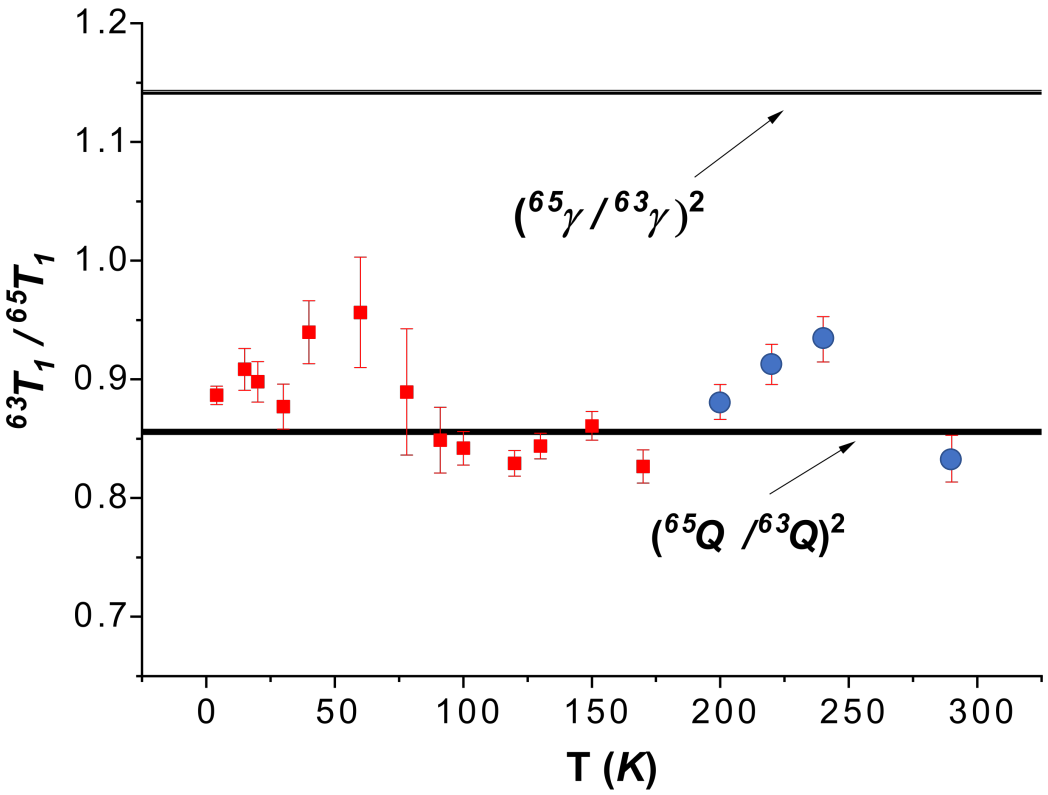

Figure 6.9: Isotopic ratio of overall relaxation rates, with limits for pure quadrupolar/magnetic relaxation indicated. Squares are for $Cu_{12}Sb_4S_{13}$ phase and circles are for Cu_3SbS_4 phase.

6.6 Anharmonicity

By employing real-space descriptors such as vibrational density of states for $Cu_{12}Sb_4S_{13}$, it has been shown[151] that the Cu12e atom has a location probability concentrated close to the plane of its 3 S neighbors (Fig. 2.1) with off plane dynamic displacement. To model the effect of such behavior on NMR relaxation Dahm and Ueda introduced a one dimensional double-well potential to study this type of problem and obtained qualitative agreement with results for β-pyrochlore oxide.[158] Following this result,[158] we define a Hamiltonian:

$$H = \frac{P^2}{2M} + \frac{1}{2}ax^2 + \frac{1}{4}bx^4, \tag{6.1}$$

where x, M and p are the coordinate, mass, and momentum of the Cu ion, respectively, and a and $b > 0$ are constants. This is treated in a self-consistent quasiharmonic approximation resulting in an effective harmonic Hamiltonian

$$H = \frac{P^2}{2M} + \frac{1}{2}M\omega_0^2 x^2, \tag{6.2}$$

where ω_0 is phonon effective mode frequency determined implicitly from $M\omega_0^2 = a + b\langle x^2\rangle_{T,\omega_0}$. The dependency of the thermal average x^2 on ω_0 and T is given by

$$\langle x^2\rangle_{T,\omega_0} = \frac{\hbar}{M\omega_0}\left(\frac{1}{e^{\hbar\omega_0/k_BT} - 1}\right). \tag{6.3}$$

Eliminating b and a in favor of $\omega_{00} = \omega_0(T = 0)$ in equation 6.1 gives:

$$\left(\frac{\omega_0}{\omega_{00}}\right)^2 = 1 + \beta\frac{\omega_{00}}{\omega_0}\left[\frac{1}{e^{\hbar\omega_0/k_BT} - 1} + \frac{1}{2} - \frac{\omega_0}{2\omega_{00}}\right], \tag{6.4}$$

where $\beta = b\frac{\hbar}{M^2\omega_{00}^3}$ is a dimensionless factor characterizing the anharmonicity. NMR spin-relaxation could be explained by two-phonon Raman process since the quadrupole term is the dominant term,

$$\frac{1}{T_1^R} = \left(\frac{k_BTV_2}{2M}\right)^2\frac{2}{\Gamma_0}\frac{4\Gamma_0^2 + \omega_r^2}{\omega_r^6}, \tag{6.5}$$

where V_2 is proportional to the second spatial derivative of the EFG, Γ_0 is amount of phonon damping and ω_r is phonon frequency renormalization which can be obtained by taking the real part of the phonon self-energy by $\omega_r^2 = \omega_0^2 + \omega_0 Re\Pi(\omega)$.

In this model we obtain a good fit to our data, as displayed in figure 6.10 by the dashed curve. This fit excluded the data shown in the figure at high temperatures, ignoring the points near the

MST for which $1/T_1$ is clearly dominated by fluctuations related to the transition. The resulting best-fit values are $\beta = 58$, $\omega_{00} = 23\ \ K$, $\Gamma_0 = 4.0\ \ K$ and $\omega_0 Re(\Pi) = -(4.7\ K)^2$, corresponding to an anharmonic potential well given by,

$$V(x) = (-13.4\ \text{J/m}^2)\ \ x^2 + (4.2 \times 10^{22}\ \text{J/m}^4)\ \ x^4. \tag{6.6}$$

This potential is shown in figure 6.11, also showing the energy levels obtained using a numerical package [161]. The separation between minima for this potential is 0.25 Å, and for comparison to crystallographic data, the rms displacement calculated for 291 K (Eq. 6.3) is $\sqrt{\langle x^2 \rangle_{\omega,T}} = 0.16$ Å.

Since the MST is believed to involve a lattice distortion, it is not clear whether the low temperature parameters should also apply above T_c. Thus, we used the method described above to fit the $1/T_{1Q}$ data points only below the transition points (T$<$ 70 K), with results shown in figure 6.10 as the dashed curve. This fitting gives $\beta = 99$, $\omega_{00} = 29$ K, $\Gamma_0 = 4.0$ K and $\omega_0 Re(\Pi) = -(8.0$ K$)^2$, an anharmonic well with a distance 0.23 Å between minima, and room temperature rms displacement of 0.13 Å. The fitted potential is thus similar but slightly narrower than what is obtained by including the high-temperature data. For the data above the MIT, it is not possible to make a separate fitting of the rattling behavior based only on the $(T_1 T) \approx$ constant plateau at these temperatures, however since the low-temperature-only fit passes rather close to these data we infer that there is not a large change in the dynamics across the MST boundary. Since the T_1 is sensitive only to dynamical behavior, rather than static disorder, it is clear that the low-temperature structure retains the rattling processes, with the dynamics not frozen out by a distortion of the structure below the MST or a large asymmetry in the potential well.

Other measures of the rattling behavior are provided by crystallographic methods, which have been analyzed to yield[151, 162] room-temperature thermal parameters for the 12e Cu site in the range 0.14 Å^2, corresponding to a rms displacement on order of 0.37 Å. However, as described

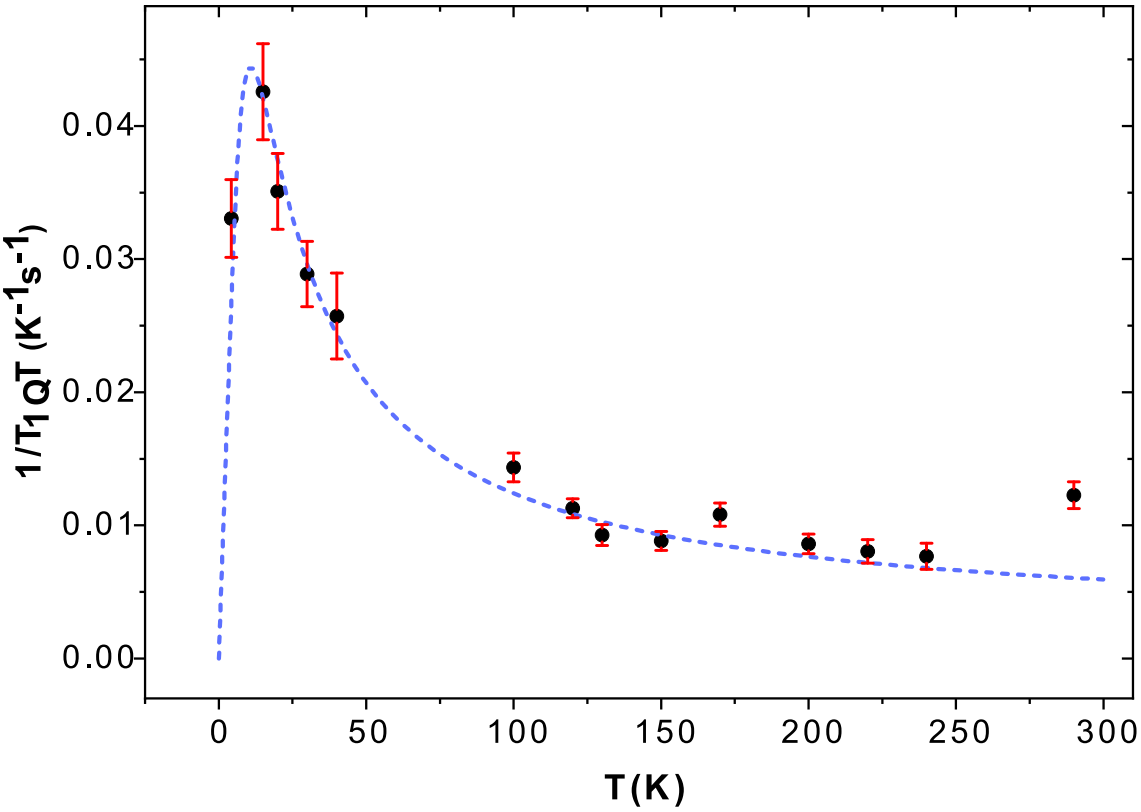

Figure 6.10: Quadrupole NMR relaxation rate for ^{63}Cu compared with the fitted anharmonic model (dashed curve). Dashed curve obtained from fit of low-T data only.

above [151] a split site analysis for this site, with probability maxima displaced by 0.30 Å bringing it closer to one of its neighbor S atoms, gives a better fitting. The latter model has as its largest residual thermal parameter U_{33} = 0.0294 Å^2 corresponding to a room temperature rms Cu 12d displacement of of 0.17 Å along one direction. This is quite close to the fitted result obtained here, making it appear likely that this indeed corresponds to a one-dimensional rattling behavior of the 12e Cu ions.

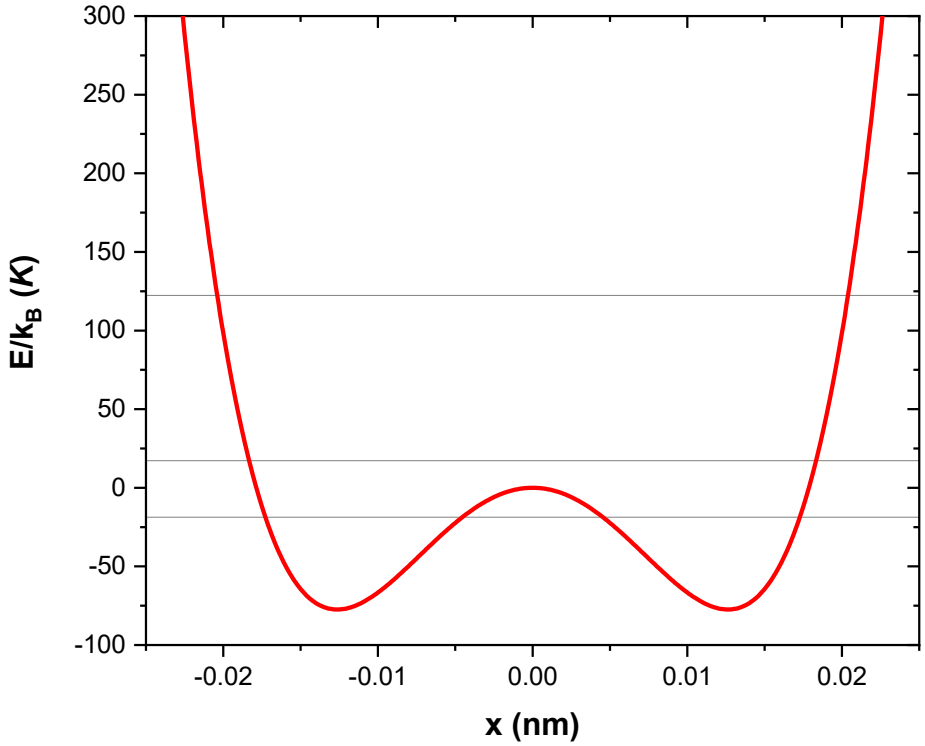

Figure 6.11: Fitted 1D double-well potential of equation 6.6 with calculated energy levels.

7. COPPER-ION HOPPING AND PHASE SEGREGATION IN CU-RICH TETRAHEDRITE*

In this chapter, ^{63}Cu NMR measurements are reported for the Cu-rich phase of $Cu_{12+x}Sb_4S_{13}$ ($x \lesssim 2$) and compared to $Cu_{12}Sb_4S_{13}$. We identify the NMR signatures of the phase segregation into Cu-poor ($x \approx 0$) and Cu-rich ($x \lesssim 2$) phases, with the metal-insulator transition observed in $Cu_{12}Sb_4S_{13}$ suppressed in the Cu-rich phase. Based on NMR T_1 and T_2 measurements, the results demonstrate Cu-ion hopping below room temperature with an activation energy of $\sim$150 meV for the Cu-rich phase, consistent with superionic behavior. The NMR results also demonstrate the effects of Cu-ion mobility in the $Cu_{12}Sb_4S_{13}$ phase, but with a larger activation barrier. We identify a small difference in NMR Knight shift for the metallic phase of $Cu_{12}Sb_4S_{13}$, compared to the Cu-rich phase, and when compared to DFT calculations the results indicate a mix of hyperfine contributions to the metallic shift. Much of these results has been reported in reference [163].

7.1 Copper Rich Tetrahedrite

The phase diagram of $Cu_{12+x}Sb_4S_{13}$ with $0 \leq x \leq 2$ has been studied over a wide range of temperatures. Samples segregate into two tetrahedrite structural phases ($Cu_{12}Sb_4S_{13}$ and $Cu_{14}Sb_4S_{13}$) which converge to a single phase [164, 165, 83] at higher temperatures, driven by relatively mobile Cu ions. In $Cu_{12}Sb_4S_{13}$, the Fermi level sits within the valence band making it metallic or heavily p-type, and a metal semiconductor phase transition (MST) occurs [166] at around 85 K, with structural changes accompanied by an increase in resistivity [166] as well as a drop in magnetic susceptibility [85]. The extra coppers in $Cu_{14}Sb_4S_{13}$ are expected to fill unoccupied states and push the Fermi level to the band-gap, hence rendering the compound insulating. There is currently practical interest in such a phase. Recently, Yan et al. [167] reported that adding 1.5 extra Cu per formula unit to $Cu_{12}Sb_4S_{13}$ enhances the efficiency up to $\sim 66\%$. In further band engineering, it was found that adding Se resulted in ~ 64 % further enhancement in power factor. A new method

*Part of this section is reprinted with permission from N. Ghassemi, Y. Tian, X. Lu, Y. Yan, X. Zhou, and J. H. Ross Jr, "*Copper-Ion Dynamics and Phase Segregation in Cu-Rich Tetrahedrite: an NMR Study,* The Journal of Physical Chemistry C, vol. 124, no. 7, pp. 3973-3979, 2020. Copyright (2020) American Chemical Society.

was also proposed in tetrahedrites to lower κ_L by using spinodal decomposition [114] of the Cu-poor and Cu-rich phases. This induces additional channels for phonon scattering and reduces the lattice thermal conductivity substantially. In addition, there are ongoing efforts to utilize Cu ion mobility in these and related Cu chalcogenides as an avenue for reducing thermal conductivity for thermoelectric applications [168], as well as in other device applications [169], although the impact of mobility on the stability of microfabricated devices is also a potential issue. Thus it is important to understand the kinetics and local structures involved in this segregation process.

NMR can be an effective way to probe ionic hopping in solids [170, 171], allowing sensitivity to a range of dynamical time-scales from 10^{-7} to 1 s and longer, not easily probed by other techniques. The local chemical information provided through NMR studies also provides a useful complement to other techniques such as diffraction studies, and also can often allow disordered or mixed systems to be studied effectively [172]. Nuclei with quadrupole moments, such as the ^{63}Cu nucleus probed here, can be particularly sensitive in this regard, since the electric field gradients which couple to the quadrupole moment can exhibit large changes in response to atomic displacements. In this work, we have used NMR techniques to study a copper rich $Cu_{12+x}Sb_4S_{13}$ tetrahedrite material. We show that the NMR spectra and relaxation times demonstrate the presence of the Cu motion extending to low temperature, with particularly high mobility observed in the copper rich tetrahedrite. Spin-lattice relation measurements provide an estimation of the activation energy of these mobile ions.

7.2 Experiment

7.2.1 Sample preparation

Synthesis: similar to the materials studied in the previous chapters, these samples are made by our collaborator, Dr. Lu. Polycrystalline samples of $Cu_{12}Sb_4S_{13}$ (Cu poor) and $Cu_{13.5}Sb_{3.98}Sn_{0.02}S_{13}$ (Cu rich) tetrahedrite were obtained by melting stoichiometric amount of high purity ($> 99.99\%$) elements (Cu, Sb, S) at 923 K for 12 h, and then cooling down to room temperature. The obtained samples were annealed at 723 K for a week. Finally, the obtained ingots were hand ground into

		Cu12 phase				Cu14 phase			
Site	WP [a]	x	y	z	SOF [b]	x	y	z	SOF
Cu-I	12d	0.25	0.5	0	1	0.25	0.5	0	0.9873
Cu-II	12e					0.2142	0	0	0.9460
Cu-II	24g	-0.2485	0.0642	-0.0642	0.5				
Cu-III	24g					0.2851	0.2851	0.0102	0.15
Sb	8c	0.2652	0.2652	0.2652	1	0.2666	0.2666	0.2666	0.9881
Sn	8c					0.2653	0.2653	0.2653	0.005
S-I	24g	0.1193	0.1193	0.3788	1	0.1144	0.1144	0.3513	1
S-II	2a	0	0	0	1	0	0	0	1

Table 7.1: Crystallographic information at 300 K for Cu rich sample including Cu12 minority phase. Lattice parameters $a = 10.4409$ Å for Cu14 (phase fraction 70%) and $a = 10.3205$ Å for Cu12 (phase fraction 30 %). $R_w = 6.05\%$. [a]SOF: site occupancy factor. [b] Wyckoff Position.

fine powder for spark plasma sintering (SPS-625) at 673 K for 5 min under a uniaxial pressure of 45 MPa.

7.2.2 Measurement methods

Room temperature powder X-ray diffraction (XRD) data were collected using a Bruker D8 spectrometer with CuKα radiation and analyzed using the GSAS-II package[173]. NMR measurements were carried out using spin echo integration versus frequency and by assembling and superposing Fast Fourier Transformation (FFT) spectra at a sequence of frequencies. These measurements were executed in a magnetic field of 8.9 T at frequencies near 100 MHz, using a custom-made pulse spectrometer in a temperature range from 4.2 to 300 K. A silver coil was used to eliminate spurious Cu NMR signals. ^{63}Cu NMR chemical shifts were referenced to CuCl.

NMR spin-lattice relaxation time (T_1) measurements were obtained based on an inversion recovery sequence implementing a multi-exponential function for recovery of the central transition [142]. We follow the convention $K = (f - f_0)/f_0$ for Knight shifts, with f_0 the standard reference frequency and positive shifts having paramagnetic sign. In the analysis, we used nuclear moment values (Q and γ) reported in Ref. [143]. Electric field gradients (EFGs) are given in terms of the standard parameters $\nu_Q = \frac{3eQV_{zz}}{2I(2I-1)h}$ and $\eta = (V_{xx} - V_{yy})/V_{zz}$.

7.3 Results and Analysis

The X-ray result and refinement are plotted in Figure 7.1. XRD analysis shows that the sample includes distinct $Cu_{13.6}Sb_4S_{13}$ and $Cu_{12}Sb_4S_{13}$ phases without any secondary phases. Detailed results are in Table 7.1. These phases will be referred to as Cu14 and Cu12 respectively. Both phases were refined in the cubic structure of space group $I\overline{4}m$ (217) with lattice constants $a = 10.4409\,\text{Å}$ and $a = 10.3205\,\text{Å}$ respectively, in good agreement with what was previously reported [164, 2]. The Cu14 majority phase has phase fraction 0.70 and the Cu12 minority phase 0.30. The Cu12 unit cell has two distinct Cu sites while Cu14 phase has three Cu sites with the site labeling the same as used previously (see figure 2.1) with the addition of the interstitial Cu-III site as previously proposed (see reference [141]). A good fit for the Cu12 minority phase was obtained by setting all sites to 100% occupancy, except for the Cu-II site which was modeled as having a split-site 24g configuration.

The half-occupied 24g site-II represents a two-fold off-center position for this ion, consistent with the fit described by Vaqueiro et al. [164]. Cu14 has a similar configuration with the addition of an interstitial Cu-III partially occupied site. Note that the XRD refinement in the Cu14 phase had a low sensitivity to Cu-I occupation in the range of 0.90 to 0.99. However, we obtained a slightly better fit with 0.99 occupation (Rw= 6.053% vs Rw= 6.138% for 0.92 occupation).

^{63}Cu NMR spectra obtained at several temperatures for a rich sample are shown in Figure 7.2. Also superposed are spectra for a $Cu_{12}SbS_{13}$ sample, as described in chapter 6 and reported previously [2]. The Cu-II position in Cu12 has a large quadrupole broadening [2] ($\nu_Q \approx 18$ MHz), and is well out of range in these spectra, whereas Cu-I has a very small quadrupole broadening ($\nu_Q \leq 1$ MHz) [148, 145, 146]. Since Cu14 has essentially the same structure, with the addition of the interstitial site, we assume here that Cu-II for the Cu14 phase is also out of range here, and we analyze these spectra as representing Cu-I and Cu-III sites for the Cu14 phase as well as the Cu-I site for the Cu12 phase. Above the Cu12 MST we find that the spectrum contains two main peaks. These are the central transitions ($-1/2 \rightleftharpoons 1/2$) for copper nuclei with $I = 3/2$. A broad peak is also observed to underlie these lines. Therefore, the spectra were fitted assuming three distinct

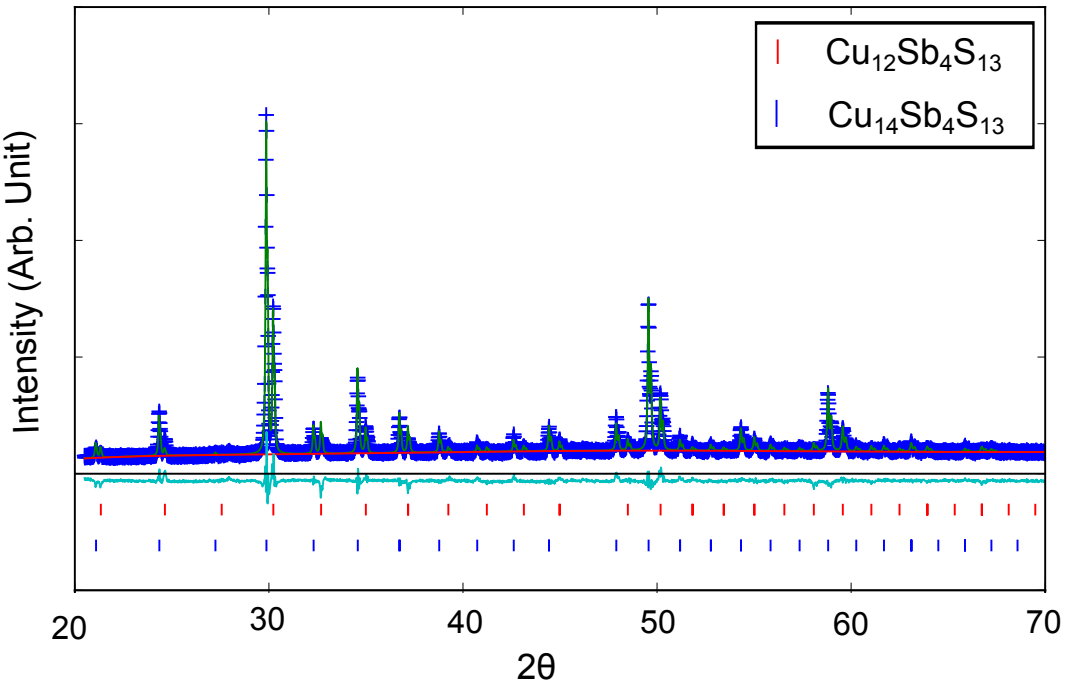

Figure 7.1: Powder X-ray diffraction patterns collected at room temperature for the Cu-rich $Cu_{13.6}Sb_{3.98}Sn_{0.02}S_{13}$ sample, showing the two fitted phases.

sites.

The Cu_3SbS_4 phase described previously was not found in the Cu14 sample, and also we tested a new Cu12 sample, with no room temperature signal which is in agreement with Matsui et al. [145] and Kitagawa et al. [146]. In the present results, the spectral weights are significantly reduced above 150 K (Figure 7.2), both in the Cu12 and Cu14 phases, an effect of ionic hopping at these temperatures, as described below.

In the analysis of the Cu-rich sample, we fitted three Gaussian peaks to the spectra corresponding to the model identified above. Figure 7.3(a) shows the lineshapes with fitted peaks at three different temperatures. One of these peaks corresponds to the Cu12 minority phase, as can be seen from the superposed spectra shown in Figure 7.2 and also Figure 7.3(b). The position for this peak rises with decreasing temperature from about 600 to 1200 ppm, in good agreement with the

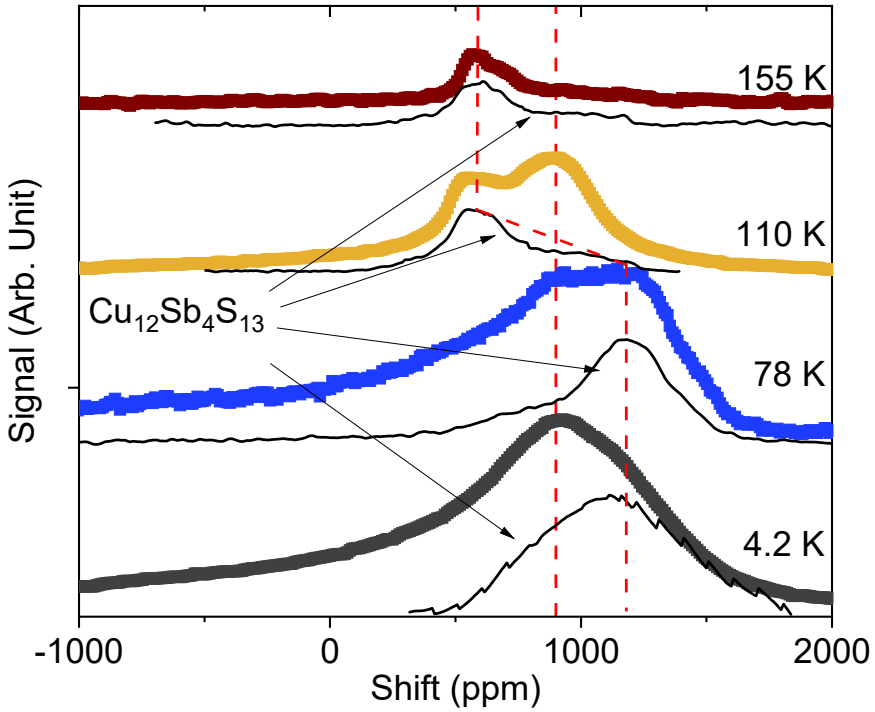

Figure 7.2: ^{63}Cu NMR spectra for $Cu_{14}Sb_4S_{13}$ at temperatures as shown. Solid curves are line-shapes for $Cu_{12}Sb_4S_{13}$ from reference[2]. The dashed lines are guides to the eye identifying the Cu-I site in Cu14 and Cu12 phases.

observed shifts for this composition [2, 145, 146]. The remaining signal is assigned to the Cu14 main phase. At 4 K the broadening is such [2] that the three peak model does not converge since the Cu12 phase also exhibits broadening due to structure change in the insulating phase. However, the general features, a shoulder at around 1200 ppm due to Cu12 and an additional peak near 900 ppm, can still be identified. These are plotted along with the fitted results in Figure 7.4 which summarizes the evolution of the peak positions vs temperature.

As the temperature changes, the fitted peak near 900 ppm remains unchanged. We attribute this peak to the Cu-I site in the Cu14 majority phase; with Cu-I in the metallic phase of the Cu12 composition known to exhibit a negative Knight shift above the MST due to the core polarization mechanism, it is reasonable that this peak should have a more positive shift in the charge balanced

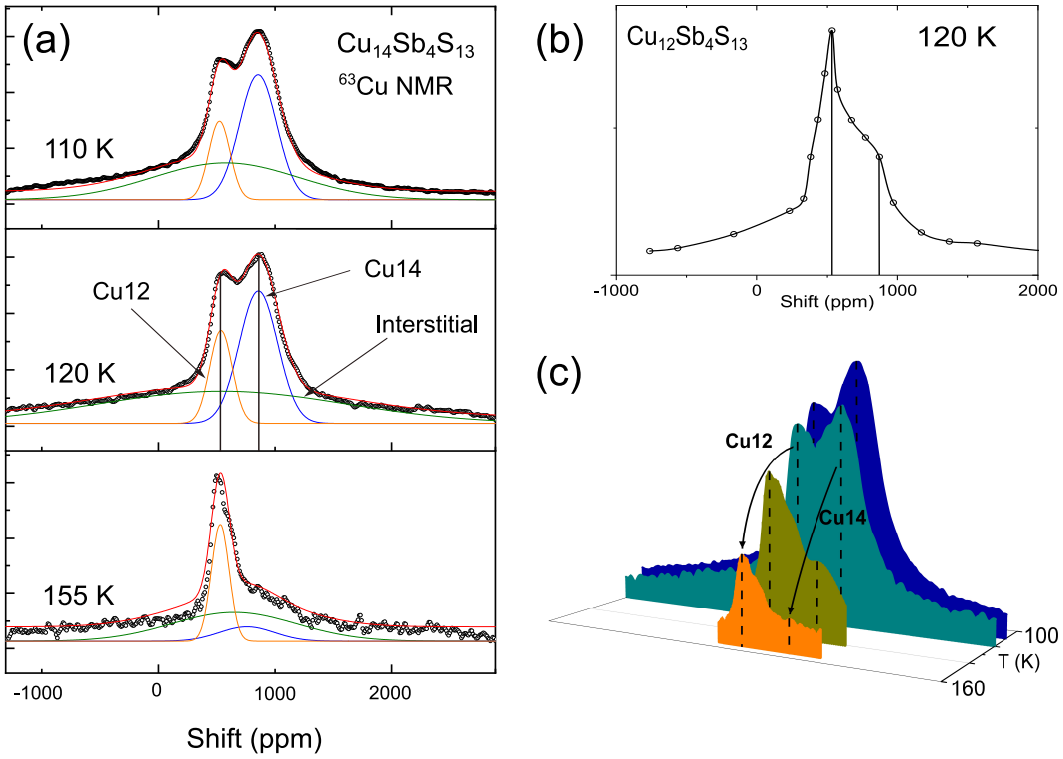

Figure 7.3: (a) NMR lineshapes and fitted spectra for Cu-rich sample at three indicated temperatures. Three fitted peaks are also shown, according to the model described in the text, as shown (b) Lineshape for $Cu_{12}Sb_4S_{13}$ sample at 120 K with the vertical lines showing identical shift positions as those in part (a). (c) ^{63}Cu spectra (NMR signal $\times T$) versus temperature for $Cu_{14}Sb_4S_{13}$ sample showing the signal loss at high T.

Cu14 phase. Note also that the line-width for this peak, as well as the Cu-I peak for Cu12, are comparable to what was recently reported [145] for Cu12. As anticipated, the results indicate that the phase transition is absent in the Cu14 phase. Meanwhile, the intensity of the much broader third fitted peak is such that it is assigned to Cu-III interstitial ions combined with Cu-I sites, as described below.

At 100 K, the fitted broad peak represents a fraction 0.40 of the NMR spectral weight, versus 0.36 for the Cu-I peak in the majority phase and 0.24 for Cu-I in Cu12 phase . XRD indicates 6 Cu-I sites fully occupied in the Cu12 phase (30% phase fraction); whereas, for the Cu-rich phase the results indicate 1.8 Cu-III ions per formula unit, in addition to the 6 Cu ions on Cu-I sites. This yields an expected relative spectral weight of 0.25 for the Cu12 phase, in reasonable

agreement with the fitting. By contrast, the Cu14 phase XRD occupancies yield expected relative spectral weights for Cu-I and Cu-III equal to 0.58 and 0.18 respectively. The corresponding fitted lines do not have this expected approximately 3:1 intensity ratio. However, the Cu-III interstitial site is a nearest-neighbor for Cu-I, and occupation of such a neighbor site would be expected to induce a large change in the EFG's experienced by the Cu-I site. With the Cu-III 24g site occupation observed to be 0.15 and since each Cu-I has four Cu-III near-neighbors, assuming random occupation of the Cu-III sites, the probability for a Cu-I to have no Cu-III neighbors will be $0.85^4 = 0.52$, and therefore half of the Cu-I sites are expected to experience a significantly enhanced EFG. The observed reduced NMR intensity for the Cu14 phase Cu-I line, and enhancement of the broad peak intensity, are in reasonable agreement with this scenario. Thus we assume that the broad peak is due to Cu-III interstitials combined with Cu-I sites directly affected by the Cu-III occupation, with the breadth due to random occupation of the latter sites.

7.4 Copper Motion

The temperature dependence of the $Cu_{14}Sb_4S_{13}$ spectra is further illustrated in Figure 7.3(c). Whereas the integrated spectral areas scaled by temperature would normally be temperature independent if the spectral weight is conserved, the observed reduction in NMR signal can be attributed to slow Cu hopping. This is observed in all samples: the NMR echo signal is sharply reduced in the temperature range 100 to 160 K, with the onset of hopping observed in both Cu-poor Cu12 as well as Cu-rich Cu14 in this same temperature range, although for Cu14 the faster drop implies greater Cu-ion mobility in the Cu14 phase. This can be compared to the large difference in Cu mobility reported for Cu12 vs. Cu14 phases at high temperatures once super-ionic behavior sets in [164].

For further confirmation of the dynamics of copper hopping, the spin-echo decay was measured by varying pulse separation, (t_{del}) in a standard spin-echo sequence, at the 900 ppm peak position for Cu-I in the Cu-rich Cu14 phase (Figure 7.5). We also made a similar measurements for the second, Cu12-dominated sample. The data were fitted to

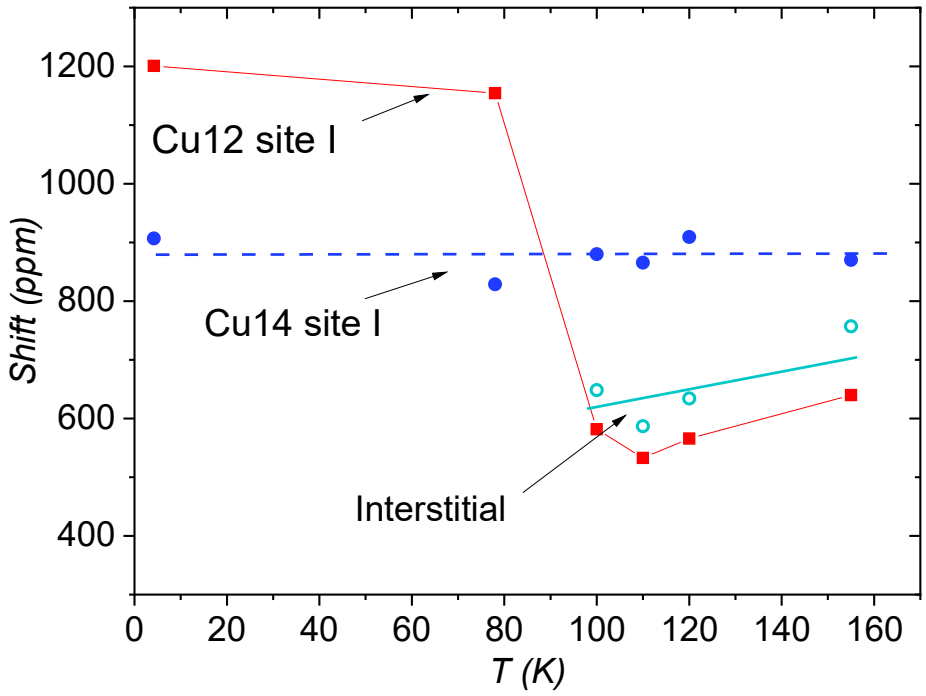

Figure 7.4: Temperature dependent peak positions for three fitted sites described in the text.

$$Echo = C[(1-\alpha)e^{-(2t_{del}/T_{2g})^2} + \alpha e^{(-2t_{del}/T_{2e})}], \tag{7.1}$$

where T_{2g} and T_{2e} are the Gaussian and exponential T_2 decays, respectively with T_2 here referring generally to all processes contributing to the echo decay. The ratio α helps to determine the relative significance of motion, since normally exponential decay is dominant when motion is important, while more nearly Gaussian decay occurs for a static NMR line, controlled by the nuclear dipole-dipole or pseudo-dipolar couplings [156].

Figure 7.6 summarizes the fitting results. The low-T decay curve for both samples is dominated by Gaussian decay. However, as the temperatures rise, α increases, indicating that atomic motion is more important. Both samples show an increasing α vs. T, signaling the onset of dynamics, see

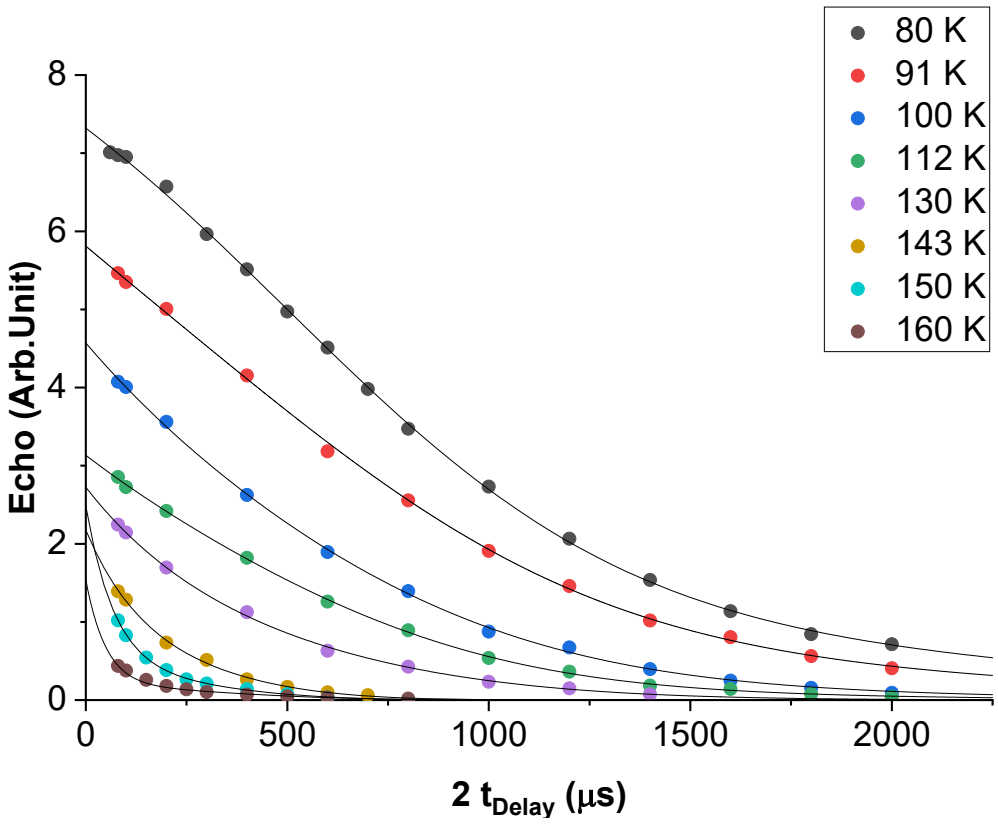

Figure 7.5: Spin echo decay rate for Cu14 phase at different temperatures, with fits described in text.

inset of Figure 7.6. Note that there is a larger underlying dipole width (shorter T_{2g}) for the Cu12 sample contributing to the observed difference in α in addition to the faster increase in $1/T_{2e}$ for Cu 14. However, clearly Cu12 has a lower mobility as the majority phase, similar to what was found as the minority phase in Cu14.

In analyzing the fitted T_{2e} for the Cu14 main phase, we assume an activated process with hopping time $\tau = \tau_0 exp(\Delta E/k_B T)$, where $\nu_0 = 1/\tau_0$ is the attempt frequency and ΔE is the activation energy. Assuming each Cu-ion hop destroys the echo refocusing process for a Cu ion and its neighbors, T_{2e} will equal the mean hopping time. This is a strong-collision, slow motion approximation, likely valid for the present case since the change of quadruple parameters associated with a sudden hopping event will make large changes in the precession frequency, removing it from the echo signal. We fitted only the last few points where α is close to 1, so that T_{2e} can be considered

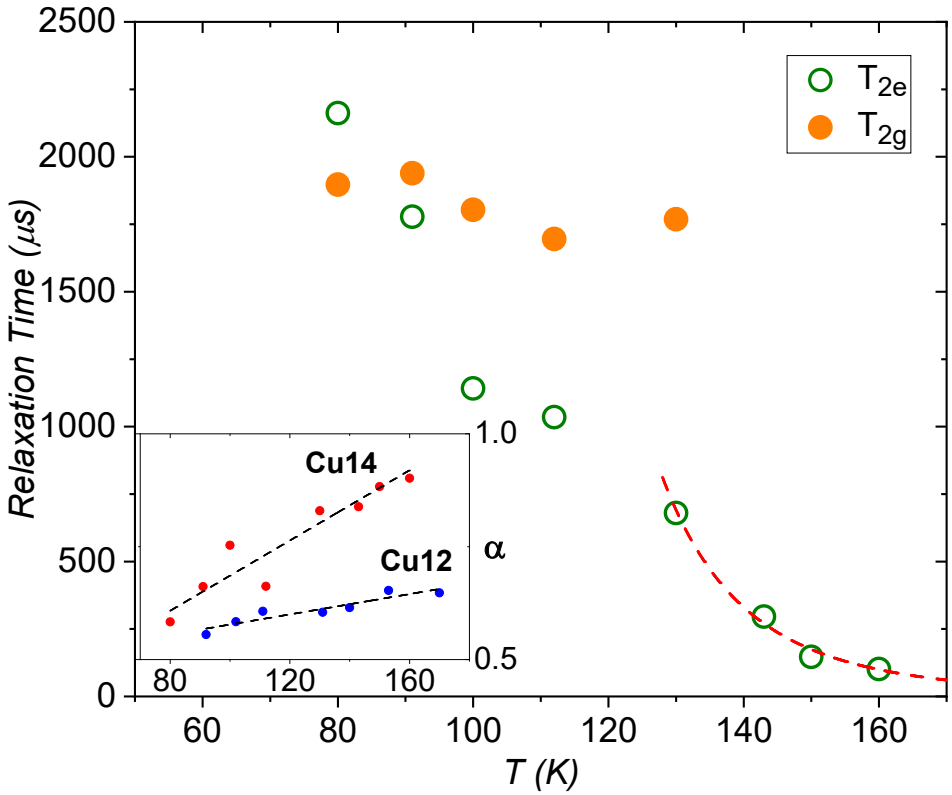

Figure 7.6: Fitting results of spin echo measurements. Main plot: T_{2e} and T_{2g} versus T for Cu14. The curve line is the fit described in the text. Inset: Fitting parameter α for majority phase in Cu rich and Cu poor samples, providing a measure of ion dynamics.

as dominated by motional processes. This yielded $\Delta E \approx 116$ meV. We also obtained a relatively large attempt time $\tau_0 \approx 2.25 \times 10^{-8}$s. The attempt time is significantly larger than expected for vibrational motions in solids, however this is a typical situation for NMR fitting for superionic conductors in the hopping regime, for reasons which are not entirely clear [174, 170]. This activation energy is consistent with the result obtained from T_1 measurements, described below. This helps to confirm the connection of kinetic processes to the disappearance of the NMR signal, rather than for example broadening or splitting of the NMR lines due to a symmetry breaking.

The nuclear dynamics can also be detected through the temperature dependence of the spin lattice relaxation time (T_1). ^{63}Cu $1/T_1T$ for the Cu14, Cu-I site, is shown in Figure 7.7. Faster relaxation behavior was reported in Matsui et al. [145] for a Cu12 sample although this is due

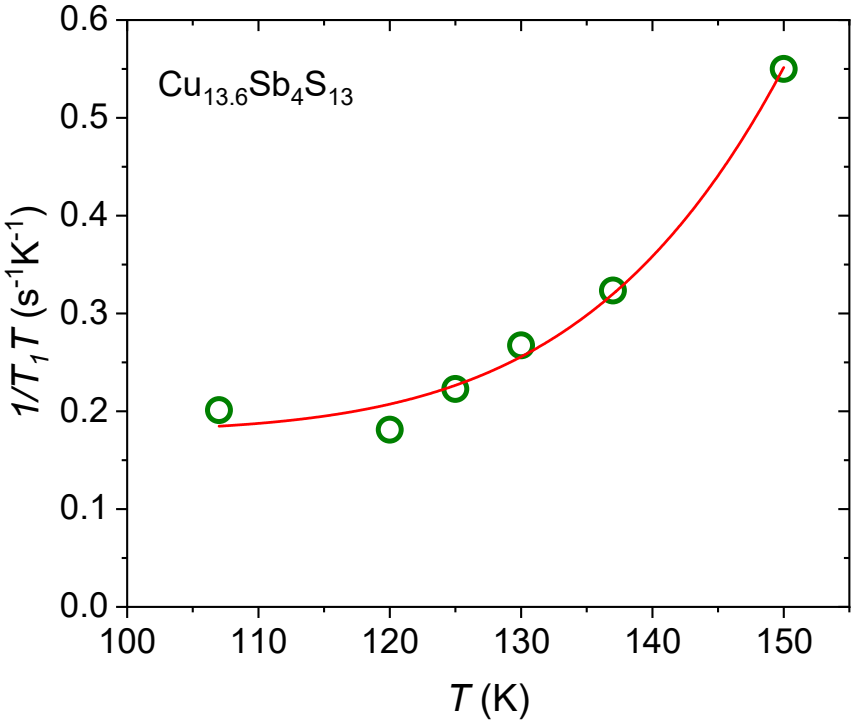

Figure 7.7: ^{63}Cu $1/T_1T$ for Cu-I site in Cu14 vs temperature. The curve is the activated fit explained in the text.

in part to the difference in fitting functions. $1/T_1T$ is fitted to the activation equation [174, 175] $a/Te^{(\frac{-\Delta E}{K_BT})} + b$, where ΔE is activation energy and a and b are constants. Figure 7.7 shows results of fitting with ΔE =145 $\pm$ 30 meV due to hopping in the Cu14 sample which is also in agreement with the activation energy we derived from T_2. Thus, even though the temperature range is limited due to the disappearance of the spin echo due to hopping, for Cu14 we obtain a consistent measure of the activated process involved here.

7.5 Discussion

The proposed Cu14 structure [86], with two extra Cu on the interstitial sites refined from X-ray diffraction, provides a good model for the observed NMR amplitudes. In the original X-ray fitting report, it had also been proposed [86] that some Cu ions were on unknown sites not accounted for by the Cu-I, Cu-II and Cu-III sites. Here we see that the 3-site model does well in accounting

for the NMR results. Previous results [164] also point to Cu-I occupation close to 1, and as noted above, NMR is consistent with this picture.

It has also been proposed [176] that the occupation of Cu-I should be reduced to 0.67 in the Cu14 phase with a corresponding fraction of Cu ions promoted to interstitial sites. This is due to the small refined Cu-I-Cu-III distance [86] of 2.37 Å. We tested this occupation in the XRD refinement, however, the R_w increased to 7.16 % with GOF= 2.38. In the refined results of the table 7.1, bond length between Cu-I to Cu-III is 2.36 Å, which is a normal Cu-Cu bond length [177, 178], however, with considerable uncertainty. Thus, it is unclear whether the Cu-I$-$Cu-III distance is an anomalously short one.

In the NMR spectra, we observed two peaks at $\sim$ 600 and $\sim$ 900 ppm for temperatures above the MST. Normally the contribution to the conduction electrons and holes to the NMR shift is a Knight shift (K). In an effective mass approximation, often appropriate for semiconductors [179], it is found that in the metallic limit $K \approx n^{1/3}$, where n is the carrier density. Thus, Cu14 (with balanced charge composition) is expected to have K much closer to zero, and thus we expect that K for the metallic phase of Cu12 is approximately equal to -300 ppm.

DFT calculations (provided in section 7.6) for $Cu_{12}Sb_4S_{13}$ show that the Cu-d partial density of states for Cu-I is $g_d(E_F) = 2.48$ eV/atom. This is comparable to what was found by Lu et al. [102] Considering the d-electron hyperfine field [180] -17.2 T/μ_B obtained for cuprate superconductors, the calculated $g_d(E_F)$ yields an estimate $K = -2470$ ppm. The observed value is considerably smaller, thus we conclude K can not simply be due to d-core polarization based on the calculated valence band of the DOS. Matsui et al. [145] have discussed that K can include considerable correlation effects. However, it is surprising that such effects should give the factor of $\sim$1/6 reduction in K that we obtain here. We speculate that there is an additional competing spin contribution to the Cu12 shift due to other mechanisms. DFT results indicate that $g_s(E_F)$ is 200 times smaller than the d term, thus it seems likely that an orbital hyperfine contribution gives partial cancellation.

The activation energy for ionic motion in the Cu14 phase is comparable to that of similar types

of superionic materials. Normally, solids that have ionic conductivity of 10 S/m or larger as well as activation energy on order of 100 meV, are considered as solid state ionics [170].Wang et al. indicate several examples of Li diffusion with E_a in the range of 170 to 220 meV[181]. Among Cu compounds, the activation energy in Cu_2Se is [182] 230 meV. In Cu_2Te the activation energy is 350 meV and doping small amount of Ag increases activation energy [183] up to 500 meV. In Cu-I the extracted [184] activation energy is 640 meV but CuI has a first-order phase transition to its superionic phase. Therefore, even though tetrahedrite has a first order transformation to its superionic phase, its Cu ions are nevertheless also quite mobile at low temperature. Thus, the results are in line with those of other materials, and the NMR activation results demonstrate that the behavior extends to low temperatures, with considerable Cu mobility apparent in both phases at room temperature and below.

Based on the activation energies we consider a simplified statistical approach to the hopping process in Cu14. Since the Cu-I site is an immediate neighbor to the partially filled Cu-III sites, we assume hopping proceeds mainly through these two sites. We further assume that the Cu-I site is in the lower energy state and that the energy difference is equal to the observed hopping activation energy. The entropy is $S = k_B\, ln\Omega$, where Ω is the multiplicity of states. If n_i is the number of Cu atoms on Cu-III interstitial sites per cell at $T = 0$ and x is the number of Cu-I atoms promoted to Cu-III site, we obtain:

$$\Omega \;\; = \left(\frac{(12N)!}{[(12-x)N]![xN]!}\right)\left(\frac{(24N)!}{[(24-n_i-x)N]![(n_i+x)N]!}\right) \tag{7.2}$$

for a large number N of unit cells. Minimizing the free energy leads to

$$\frac{x(n_i+x)}{(12-x)(24-x-n_i)} \;\; \approx e^{-\Delta/KT}, \tag{7.3}$$

where Δ is the energy difference between Cu-I and Cu-III sites. Using $\Delta = 145$ meV derived from

T_1 fitting results at room temperature, with $n_i = 4$ (corresponding to the $Cu_{14}Sb_4S_{13}$ composition) this leads to $x = 0.14$. This corresponds to Cu-I occupation of $1 - (0.14/12) = 0.99$. At 493 K, the Cu-I occupation based on the same model is reduced to 0.90. The XRD results for Cu-I in the Cu14 phase shows occupation of 0.99 at room temperature which agrees with this estimation. Also Vaqueiro et al. [164] show that the occupation in their sample drops from 0.92 at room temperature to 0.86 at 493 K, before at higher T the phases become mixed in a first-order transition. The agreement seems reasonable.

For Cu12 phase the composition corresponds to $n_i = 0$. Assuming an activation energy of 150 meV gives a room temperature Cu-I occupation of 0.88 which is much smaller than the observed 1.00 occupation. This agrees with our observation that the Cu12 NMR line amplitude drops more slowly vs. T, indicating a larger activation energy. Assuming instead an activation energy of 280 meV for Cu12 leads to $x = 0.06$ at room temperature (thus Cu-I occupation equal to 0.99), and $x = 0.54$ at 493 K (occupation of 0.95). This agrees with our XRD refinement for Cu-I in the Cu12 phase and also the reported occupation dropping to 0.95 for this phase [164] at 493 K. Thus, the fitted activation energy results, along with an estimated larger energy for Cu12, are consistent with the reported site occupations, giving further confirmation to the analysis of the NMR results. For the Cu12 phase as noted above, the activation energy is larger by a factor on order of two, however this result is still in the range observed for other superionic conductors, and a significant amount of Cu-ion mobility is to be expected at high temperatures in both of these phases. This result should be important for device design and development.

7.6 DFT Results

Density function theory (DFT) calculations were conducted using the WIEN2k package [132]. We took separation energy between core and valence states as RK_{max}= 6 Ry, the plane-wave expansion cutoff $G_{max} = 12\ Bohr^{-1}$, and $12 \times 12 \times 12$ k-points and adopted the exchange correlation functional introduced by Perdew, Burke, and Ernzerhof (PBE) [130]. The calculation was run without spin-orbit coupling or spin polarization. Density of states results are shown in Figure 7.8, for the Cu-I site, and in Figure 7.9 for the Cu-II site. Also, Figure 7.10 shows a comparison

of the full density of states and the Cu partial densities of states (for all orbital symmetries) for the two sites. The full density of states is comparable to what has been reported previously [3].

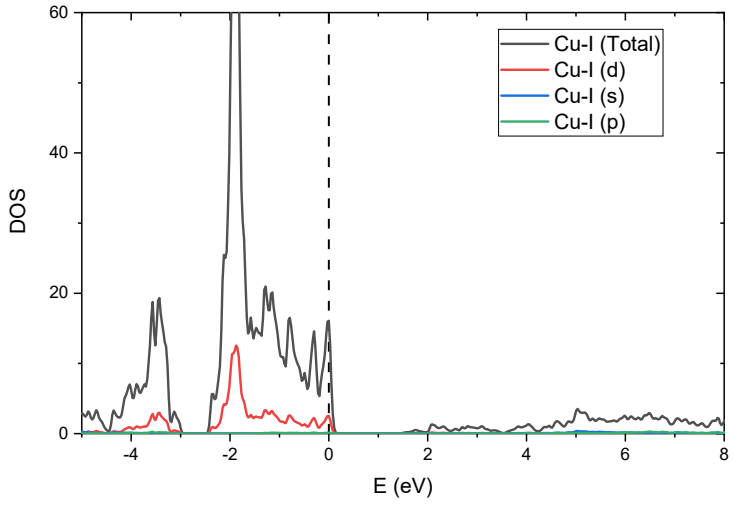

Figure 7.8: Partial density of states of Cu-I for $Cu_{12}Sb_4S_{13}$.

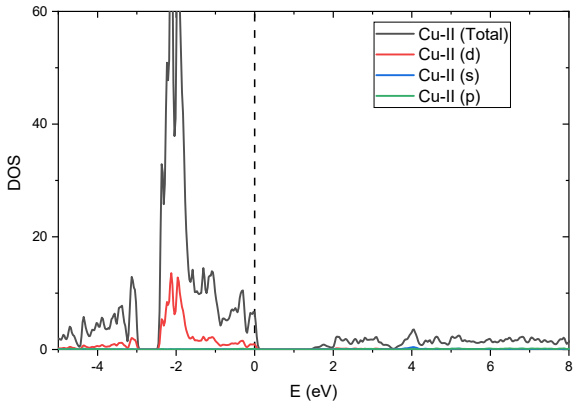

Figure 7.9: Partial density of states of Cu-II for $Cu_{12}Sb_4S_{13}$.

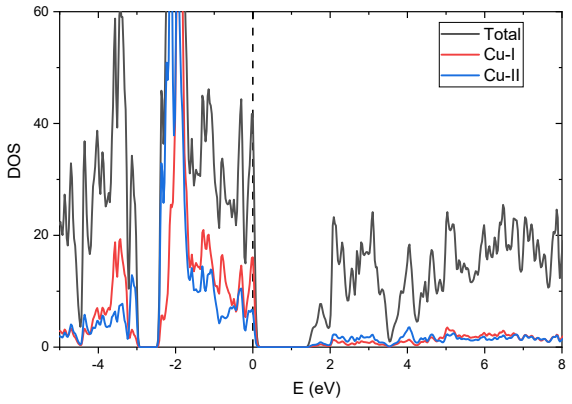

Figure 7.10: Partial density of states for Cu-I and Cu-II and total density of states for $Cu_{12}Sb_4S_{13}$.

8. IMPACT OF DOPING TETRAHEDRITE WITH RARE EARTH ELEMENTS

In this chapter, I will discuss the consequences of substitution of transition metals with 3d electrons on electronic and magnetic characteristics of the parent $Cu_{12}Sb_4S_{13}$. For this purpose, I analyzed the low-temperature experiments as well as first-principles electronic-structure calculations. Furthermore, I will report the result of substitution of Te on Sb sites.

In total, results for eight samples are described in this chapter. The samples are provided by Dr. Lu from Chongqing University and have been prepared in the following method: All doped samples were obtained by melting the stoichiometric amount of high purity elements at 923 K for 12 h, and then cooling down to room temperature. The obtained samples were annealed at 723 K for a week. Eventually, the obtained ingots were hand ground into fine powder for spark plasma sintering (SPS-625) at 673 K for 5 min under a uniaxial pressure of 45 MPa. WDS measurements was carried out for some samples in Materials Characterization Facility (MCF) at Texas A&M University. The powder X-ray diffraction (XRD) patterns of the samples were obtained with a Bruker D8 diffractometer with using CuK_α ($\lambda = 1.5418\,\text{Å}$ radiation). GSAS II software was implemented for Rietveld refinement [173].

8.1 NMR Results

8.1.1 $Cu_{10.6}Zn_{0.5}Ni_{0.9}Sb_4S_{13}$ Sample

In order to test the stoichiometric composition of this sample, an electron microprobe experiment was performed implementing wavelength dispersive specrometry (WDS) on Cameca SXFive armed with wavelength dispersive x-ray spectrometers to test composition. Measuring at 10 locations, we obtained a mean composition of $Cu_{10.6}Zn_{0.5}Ni_{0.9}Sb_4S_{13}$, with statistical fluctuation corresponding to less than 2% relative uncertainty in these values. A back-scattered image is shown in figure 8.1.

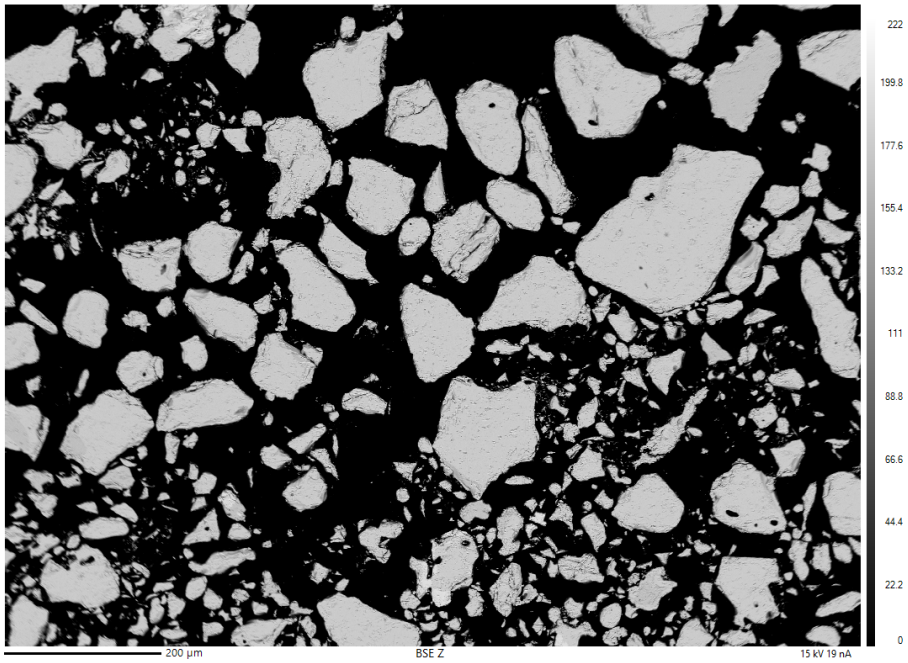

Figure 8.1: Back-scattered electron image of the $Cu_{10.6}Zn_{0.5}Ni_{0.9}Sb_4S_{13}$ sample after heat treatment (scale bar 200 μm in the bottom of the figure).

Further, to test the crystal structure parameters, we performed powder XRD measurement for this sample and the refinement parameters based on weighted profile, in the typical Rietveld refinement for $Cu_{10.6}Zn_{0.5}Ni_{0.9}Sb_4S_{13}$, as well as $Cu_{10}ZnNiSb_4S_{13}$, and $Cu_{10}Zn_2Sb_4S_{13}$ samples described later, at 290 K, Rws are 6.23%, 6.445%, and 7.32% respectively. The XRD patterns and crystallographic information are shown, in figure 8.2.

Note that Ni, Cu, and Zn atoms are next to each other in the periodic table and powder XRD typically does not have enough sensitivity to distinguish these elements. Therefore we used the unsubstituted $Cu_{12}Sb_4S_{13}$ composition to fit the lattice parameters. Full site occupations were also assumed due to small sensitivity to these parameters. The filled lattice parameters for the three samples at room temperature are $a = 10.3224\,\text{Å}$, $a = 10.3482\,\text{Å}$, and $a = 10.3781\,\text{Å}$ for $Cu_{10.6}Zn_{0.5}Ni_{0.9}Sb_4S_{13}$, $Cu_{10}ZnNiSb_4S_{13}$, and $Cu_{10}Zn_2Sb_4S_{13}$ samples respectively. There are shown in figure 8.3. The $a = 10.3781\,\text{Å}$ obtained for $Cu_{10}Zn_2Sb_4S_{13}$ sample is in good agreement with

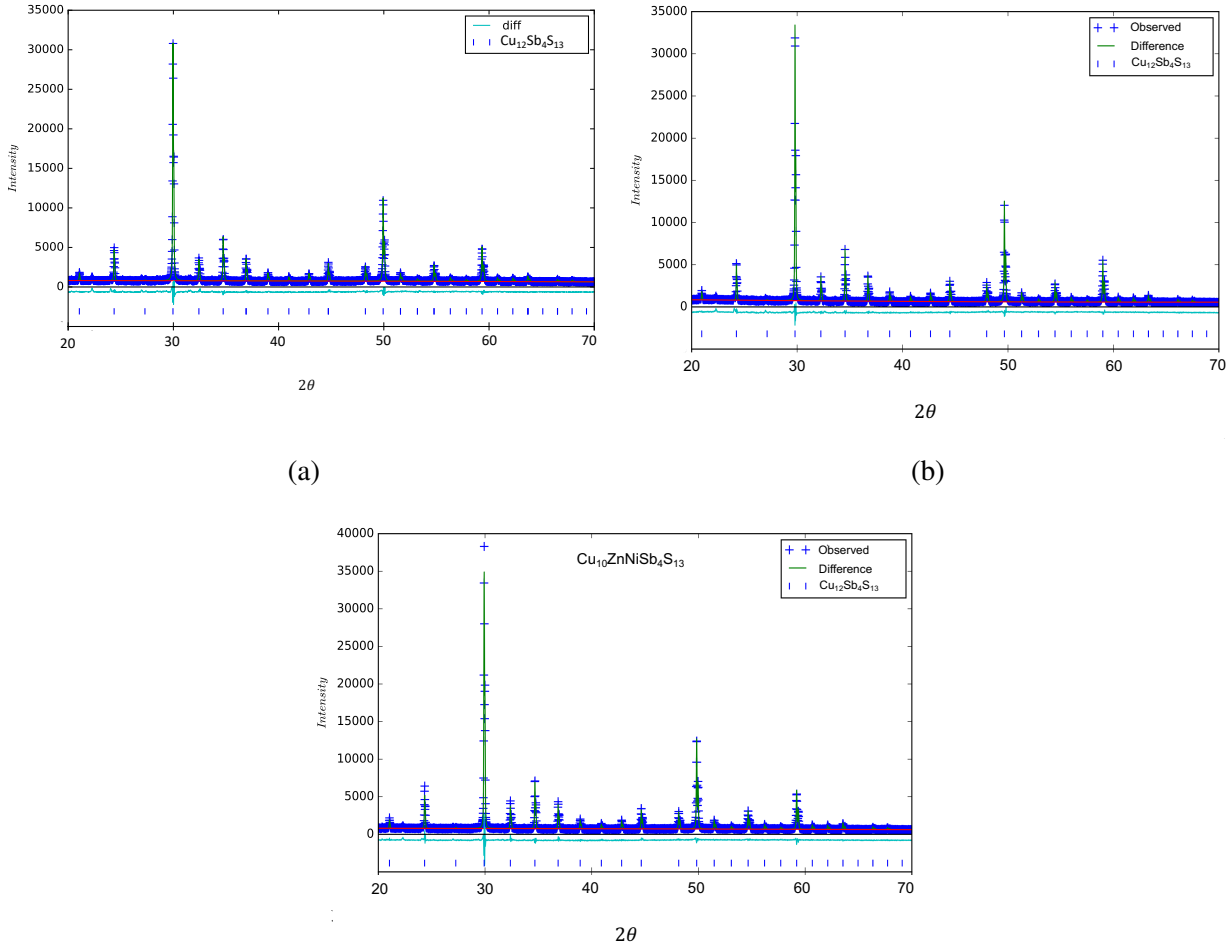

Figure 8.2: Room temperature X-ray powder diffraction data for doped tetrahedrite samples, with refined curves (green) and difference plots. The results were fitted to $Cu_{12}Sb_4S_{13}$ room temperature structure with occupation unchanged. (a) $Cu_{10.6}Zn_{0.5}Ni_{0.9}Sb_4S_{13}$ sample, Rw=6.23%, and lattice constant $a = 10.3224$ Å. (b) $Cu_{10}Zn_2Sb_4S_{13}$ sample, Rw=7.32% and lattice constant $a = 10.3781$ Å. (c) $Cu_{10}ZnNiSb_4S_{13}$ sample, Rw=6.445% and lattice constant $a = 10.3482$ Å.

$a = 10.38$ Å in reference [7] and the Zn, Ni dual-substituted materials fall between the limiting cases of Ni_2 and Zn_2 substitution, as might be expected.

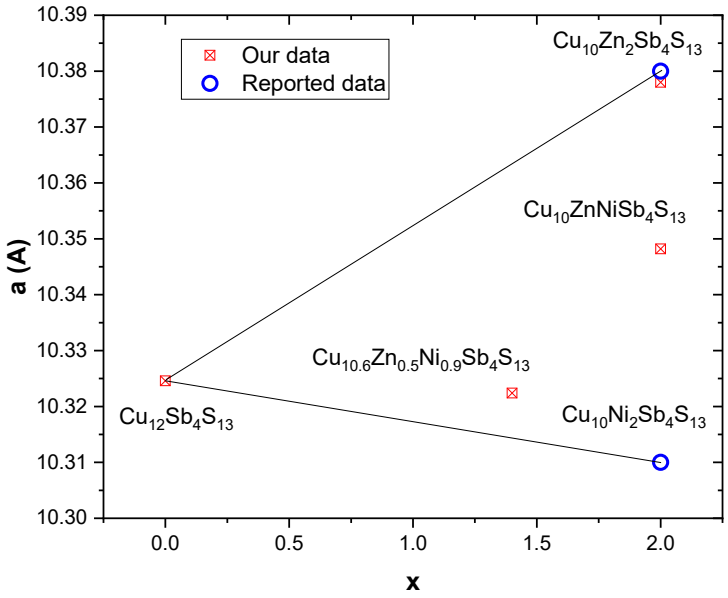

Figure 8.3: Lattice parameter for doped $Cu_{12-x}Tr_xSb_4S_{13}$ tetrahedrites. The data for $Cu_{10}Ni_2Sb_4S_{13}$ and $Cu_{10}Zn_2Sb_4S_{13}$ sample is from reference [7]. Lines show schematically the behavior of the partially substituted Zn and Ni materials.

Fig.8.4 illustrates a ^{63}Cu NMR spectrum for the $Cu_{10.6}Zn_{0.5}Ni_{0.9}Sb_4S_{13}$ sample at room temperature. There are three clear peaks giving indication of two sites, similar to undoped tetrahedrite, described in previous chapters, with the narrow peak in the middle with small ν_Q and two peaks corresponding to a larger ν_Q site.

Line-shapes were fitted as powder patterns assuming two sites. A narrow peak at the center considered to belong to site I was fitted with $K_{iso} = 930$ ppm and ν_Q= 0.9 MHz and large EFG broadening. The second line is assigned to site II and fitted with ν_Q= 19 MHz and $K_{iso} = 2000$ ppm. The peak with small EFG is assigned to Cu-I and the peak with larger EFG is assigned to Cu-II based on similarities to the unsubstituted $Cu_{12}Sb_4S_{13}$ phase. Site II has second order quadrupole

contribution in the range of this spectrum while site I has first and second order quadrupole contributions.

We further analyzed the areas under the fitted line using a custom filling routine written by members of our research group. The areas represent the signal associated with specific sites in the structure and can provide a quantitative comparison of the site occupancies. The calculation includes the appropriate spin-matrix amplitudes for the central transitions and satellites and with those factors the calculation obtains a site ratio of 1.6 for Cu-I vs Cu-II. This is somewhat larger than predicted from DFT calculation results that show Ni and Zn atoms prefer to substitute on the Cu-I sites in the $Cu_{12-x}Tr_xSb_4S_{13}$,(Tr= Ni, Zn), compositions [91]. For example substituting for 1.4 Cu-I sites-I this case would yield a ratio $6/4.6 = 1.3$. The NMR results are, thus, consistent with substitution on this site, but the ratio is enhanced for reasons not yet known, for example substitution might also cause additional promotion of Cu-I atoms to interstitial sites as discussed previously for the $Cu_{14}Sb_4S_{13}$ composition. The general result is in agreement with DFT calculation results that show Ni and Zn atoms prefer to substitute to the Cu-I sites in the $Cu_{12x}Tr_xSb_4S_{13}$,(Tr= Ni, Zn), compositions [91].

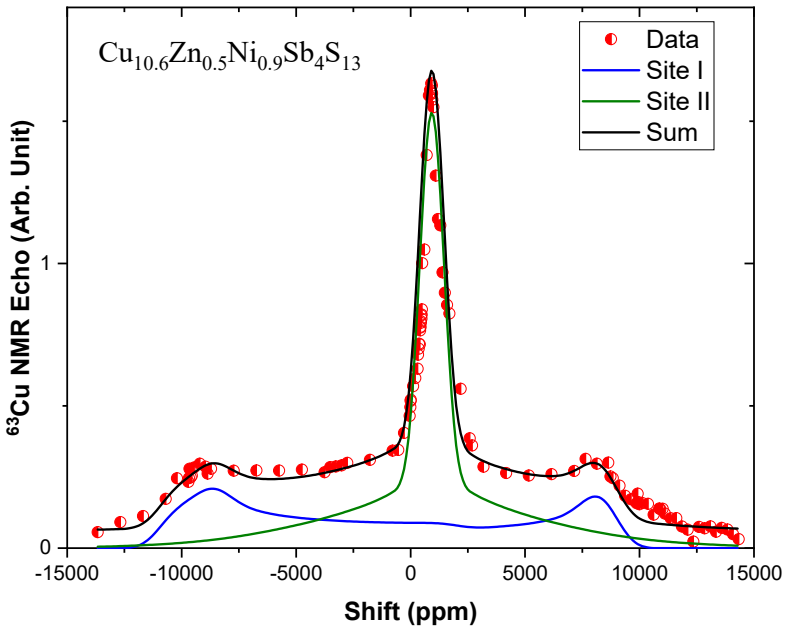

Figure 8.4: ^{63}Cu NMR spectrum for $Cu_{10.6}Zn_{0.5}Ni_{0.9}Sb_4S_{13}$ sample at room temperature with fit discussed in the text.

The EFG indicates the rate of change in electric field around the nuclei and is connected to ν_Q by $\nu_Q = \frac{9eQV_{kk}}{6I(2I-1)}$ where I is the nuclear spin and $V_{kk} = \partial V/\partial x_k \partial x_k$ is the major principal EFG tensor component, while the asymmetry parameter η is defined as $\eta = V_{ii} - V_{jj}/V_{kk}$.

The large distribution of EFGs on Cu-I (fitted to a $\nu_Q = 1.8$ MHz full-width ν_Q distribution) could be explained as due to the alloy disorder effect on the four-coordinated distorted tetrahedral sites Cu-I as expected. This can be further enhanced by the random local structural distortions (see section 8.1.4) which is a likely effect of substitution. The narrow central peak associated with Cu-I is broadened only to second order by the EFG's while the signal in the -5000 to 5000 ppm range associated with its first order satellite has first order quadrupole broadening. In our fitting very large EFG distribution was applied, however, since the second order quadrupole term is proportional to ν_Q^2/ν_L, for the central transition the broadening is masked by other inhomogeneous terms.

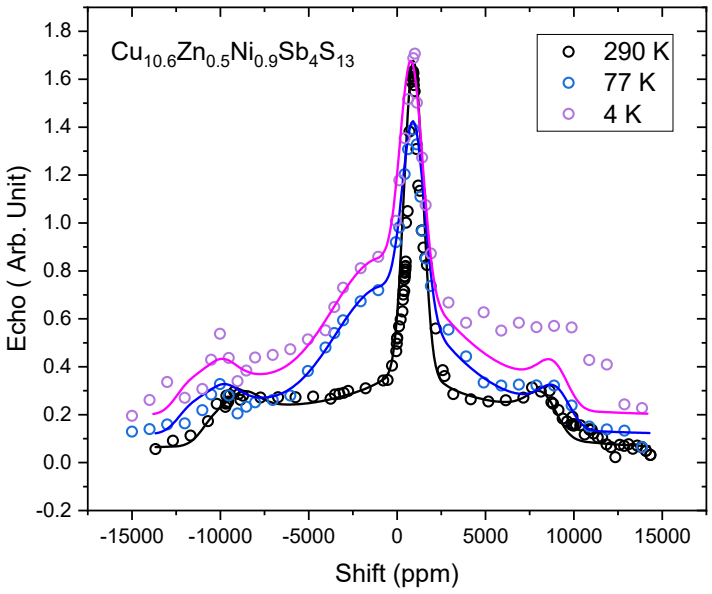

Figure 8.5: ^{63}Cu NMR line shapes for $Cu_{10.6}Zn_{0.5}Ni_{0.9}Sb_4S_{13}$ at temperatures of 4K, 77 K, and 291 K. Line shapes have been scaled for convenience to give comparable intensities at the narrow peak position. Solid curves drawn according to the model described in the text.

Fig. 8.5 shows the changes of the $Cu_{10.6}Zn_{0.5}Ni_{0.9}Sb_4S_{13}$ lineshape at lower temperatures. Due to the overall broadening due to alloy disorder and Ni magnetic moments, the low-temperature curves were not fitted to a specific set of NMR parameters. However, the most prominent change is the development of a broad peak at frequencies below the sharp peak (-4000 to 0 ppm range). The curves shown for 77 K and 4.2 K in the figure were thus generated according to a model in which a third broadened peak was added to the spectra of the two sites fitted at 290 K described above, with the Cu-I and Cu-II site parameters essentially unchanged from 290 K. The agreement appears reasonable with the third peak having a shift of -680 ppm, for both 77K and 4.2K, although at 4.2 K there are further apparent lineshape changes in the range of +10,000 ppm. The extra peak is reminiscent of the lineshape changes observed in unsubstituted $Cu_{12}Sb_4S_{13}$ (Fig. 6.3) although the ranges of shift here is larger. Based on the fact that the modified central portion of the lineshape remains unchanged going from 77 K to 4.2 K the likely conclusion is that these changes

are associated with a structural modification connected to the metal-insulator transition, which is present in the $Cu_{10.6}Zn_{0.5}Ni_{0.9}Sb_4S_{13}$ composition as well as in the unsubstituted tetrahedrite. The metal-insulator transition is discussed further in section 8.2.2.

8.1.2 $Cu_{10}ZnNiSb_4S_{13}$

This sample has a larger amount of substitution for Cu. The composition is the nominal one, although the XRD fit discussed above is in good agreement with 1:1 Zn : Ni ratio of starting composition. The lineshape is plotted in Fig. 8.6. A comparison with $Cu_{10.6}Zn_{0.5}Ni_{0.9}Sb_4S_{13}$ sample is shown in figure 8.7. In this case, the larger Ni substitution enhances the broadening so only the central- peak region was identified. We see that there is a paramagnetic broadening in low temperatures in both samples, since the lineshape becomes broader as the temperature reduces. Because of the observed broadening in the lineshape, we measured relaxation rates $(1/T_1)$ for these samples to study the magnetic behavior on this sample.

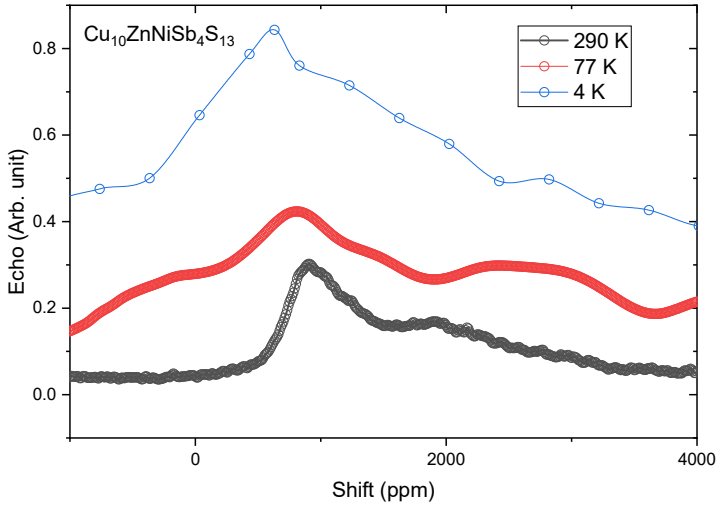

Figure 8.6: ^{63}Cu lineshape for $Cu_{10}ZnNiSb_4S_{13}$ at three temperatures. Spectra displaced upward for clarity.

The behavior of $1/T_1T$ is plotted in figure 8.8. We see that the $1/T_1T$ is relatively constant at higher temperatures in both samples and increases at low temperatures. This high temperature behavior is indicative of magnetic fluctuations, due to moments unpaired d-electron on the Ni atoms on this sample which will be discussed later. At low temperature $1/T_1T$ rises up, which is indicative of quadrupole and rattling behavior in both samples. Additional more detailed analysis of the $Cu_{10.6}Zn_{0.5}Ni_{0.9}Sb_4S_{13}$, rattling results will be given later. The $Cu_{10.6}Zn_{0.5}Ni_{0.9}Sb_4S_{13}$ sample clearly has rattling behavior at low temperatures. The enhanced low temperature$1/T_1T$ is consistent with very large thermal conductivity observed in this material.

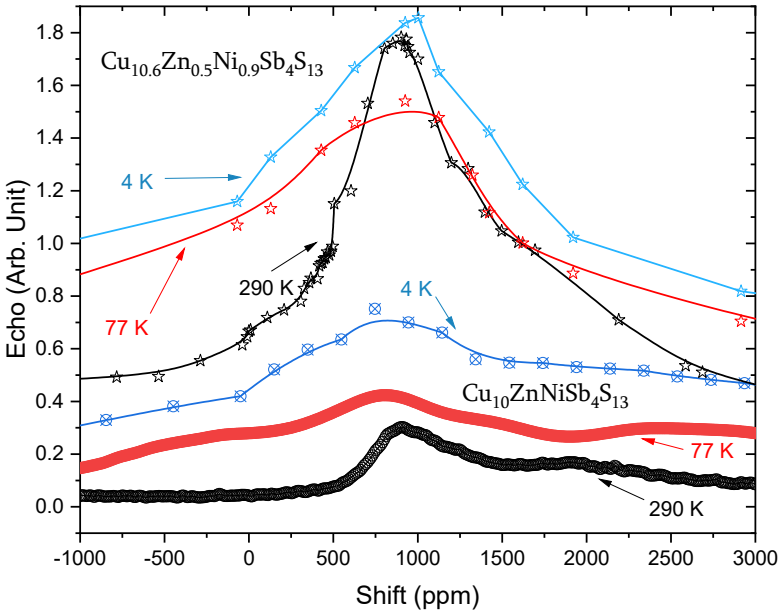

Figure 8.7: Comparison between ^{63} lineshapes for $Cu_{10}ZnNiSb_4S_{13}$ and $Cu_{10.6}Zn_{0.5}Ni_{0.9}Sb_4S_{13}$ at various temperatures with spectra displaced vertically for clarity.

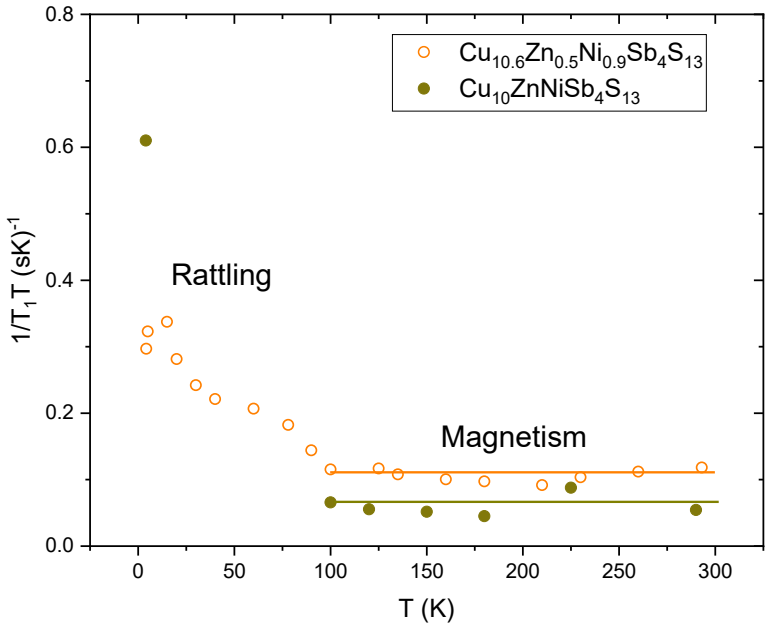

Figure 8.8: $1/T_1T$ for $Cu_{10}ZnNiSb_4S_{13}$ and $Cu_{10.6}Zn_{0.5}Ni_{0.9}Sb_4S_{13}$ versus T showing magnetic and rattling (discussed in the text) behavior. The lines exhibits the general behavior of the $1/T_1T$.

8.1.3 $Cu_{10}Ni_2Sb_4S_{13}$

The ^{63}Cu lineshapes in the $Cu_{10}Ni_2Sb_4S_{13}$ sample at three temperatures are shown in figure 8.9. In all temperatures, there is one peak with large line-width. These are presumably associated with the Cu-II site. However, a large shift to low frequencies is observed going to 4 K, a behavior which is different from that of the samples undergoing the MST. This appears to be due to the enhanced magnetic interactions in this material (section 8.2.3). Similar to other samples, the line width is increased with decreasing the temperature. This broadening is also further analyzed in section 8.2.3.

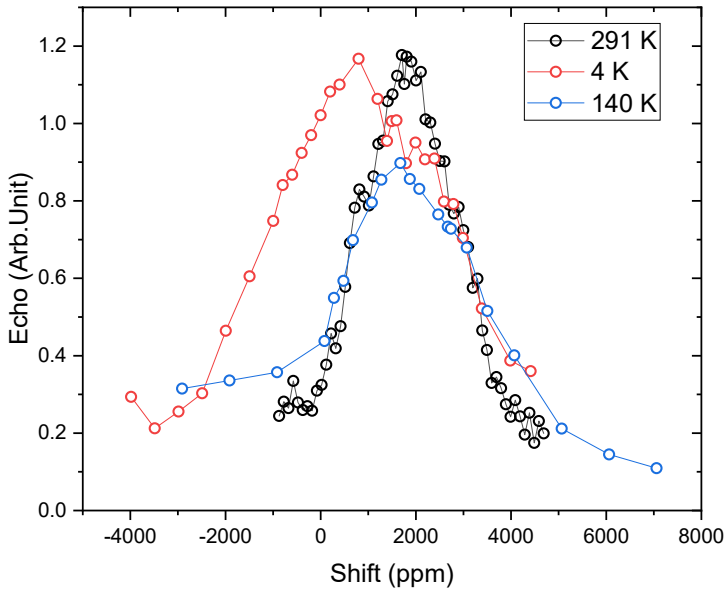

Figure 8.9: ^{63}Cu lineshapes for $Cu_{10}Ni_2Sb_4S_{13}$ at three temperatures.

8.1.4 $Cu_{10}Zn_2Sb_4S_{13}$

The ^{63}Cu NMR spectrum for the $Cu_{10}Zn_2Sb_4S_{13}$ sample at room temperature is shown in figure 8.10. A fit was done in Quadfit [144], assuming two sites based on similarities to other tetrahedrites and then further modeled using custom software to properly determine the occupation ratios. The narrow sharp peak at 980 ppm is attributed to Cu-I and fitted with ν_Q= 2.5 MHz with η= 0 and magnetic shift K_{iso} = 1033 ppm, along with its first order satellites, and the two outer peaks associated with the Cu-II sites were fitted to ν_Q= 17.0 MHz with magnetic shift K_{iso} = 1870 ppm. Thus we see that the results are similar to those of $Cu_{10.6}Zn_{0.5}Ni_{0.9}Sb_4S_{13}$: in both cases there is significant change with substitution for the Cu-I site, which has a magnetic shift of 650 ppm in unsubstituted $Cu_{12}Sb_4S_{13}$, vs 930 ppm for $Zn_{0.5}Ni_{0.9}$ substitution and 1033 ppm for Zn_2 substitution. In part this is due to the absence of Knight shift in the charge-balanced TM substituted compositions, although the change upon substitution represents only about half of the 600 ppm increase in shifts accompanying the metal-insulator transition in $Cu_{12}Sb_4S_{13}$ (chapter 6). Note that

a recent report [185] described a 950 ppm shift for a Zn_1-substituted sample, very similar to the results shown here, and below we will show that most of the substituted tetrahedrites exhibit very similar Cu-I parameters independent of composition indicating an underlying electronic behavior which is distinct from that of unsubstituted $Cu_{12}Sb_4S_{13}$. On the other hand, the Cu-II site exhibits gradual changes vs composition, with values of magnetic shift changing from a reported 2100 ppm for unsubstituted $Cu_{12}Sb_4S_{13}$ [145] to 2000 ppm ($Zn_{0.5}Ni_{0.9}$) and 1870 ppm (Zn_2).

For the two fitted lines, the extracted spectral weight ratios of sites one and two, (Cu I) / (Cu II) is 1.78. This result is somewhat larger than expected from *ab initio* calculation where suggests the Zn atoms prefer to substitute on the Cu-I sites in the $Cu_{11}ZnSb_4S_{13}$ sample [91]. In the case that Zn substitutes for 2 Cu-I sites, this leads to an expected ratio 6/4 = 1.5. Our NMR analysis is consistent with substitution on this site, however the ratio is increased. The enhanced ratio is similar to what was found for $Cu_{10.6}Zn_{0.5}Ni_{0.9}Sb_4S_{13}$ sample. This could be due to substitution causing Cu atoms on the four-fold Cu-I sites to jump into the Cu-III interstitial sites as similar to $Cu_{14}Sb_4S_{13}$ sample, discussed in the previous chapter.

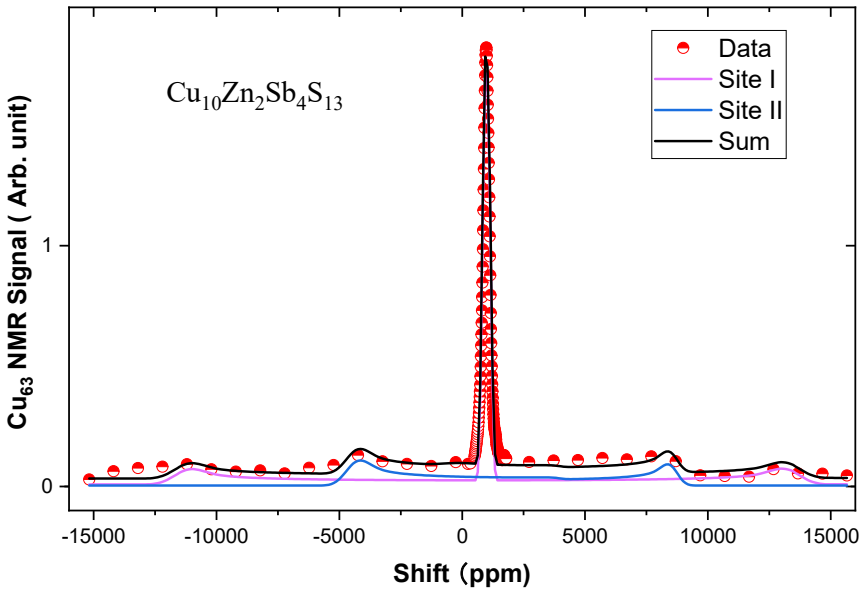

Figure 8.10: ^{63}Cu NMR spectrum in $Cu_{10}Zn_2Sb_4S_{13}$ sample at room temperature along with fitted curve.

The linearized augmented plane-wave (LAPW) method as implemented in WIEN2K [132] was used to calculate electronic band structures and densities of states for $Cu_{10}Zn_2Sb_4S_{13}$. Self-consistent calculations were carried out using the Perdew-Becke-Ernzerhof (PBE) generalized gradient approximation (GGA) for the exchange-correlation (V_{xc}) functional and plane wave basis. This calculations ran using the primitive cell of $Cu_{10}Zn_2Sb_4S_{13}$, with $10 \times 10 \times 10$ k point mesh. Periodic superstructures were used to model the structures for $Cu_{10}Zn_2Sb_4S_{13}$. In both cases, the crystal structure has space-group 121 ($I\bar{4}2m$) with Zn substituting in one case for the Cu-I site and in another case for the Cu-II site. The results are illustrated in figure 8.11b and 8.11a respectively.

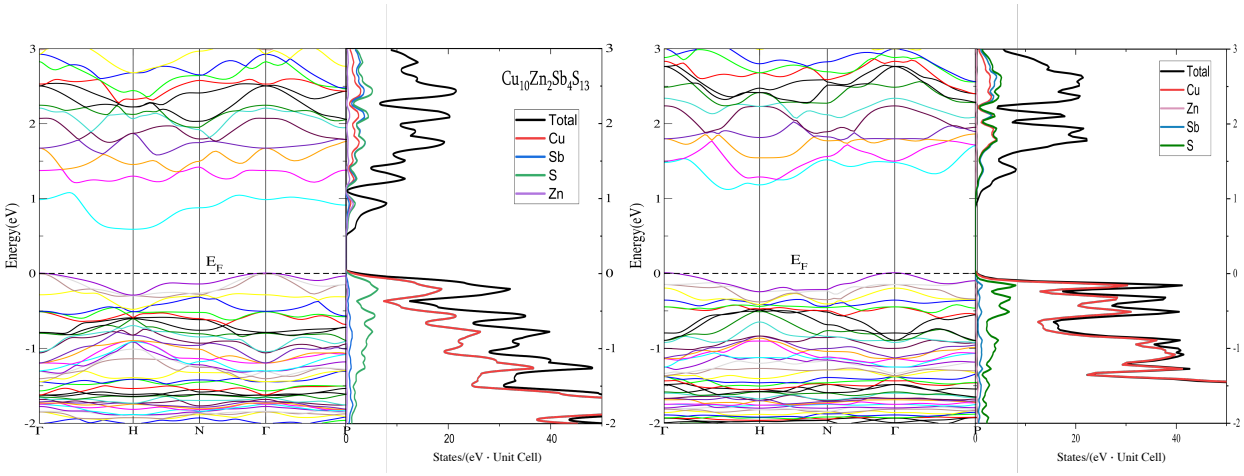

(a) (b)

Figure 8.11: Calculated electronic band structure and density of states for $Cu_{10}Zn_2Sb_4S_{13}$. a) When Zn atoms substitute on Cu-II sites. b) When Zn atoms substitute on Cu-I sites.

Our DFT calculations for $Cu_{10}Zn_2Sb_4S_{13}$ show that this sample is electrically insulating. The valence band is created by hybridizing sulfur 3p and copper 3d electrons, but with the partial density of states strongly weighted toward Cu states at the valence band edge. The Zn doped tetrahedrite has a well-developed energy gap splitting the p-d hybridized valence bands from the conduction bands of mainly sulfur and antimony's p orbitals. In the pure tetrahedrite, the Fermi level is located below the top of the valence band which makes this material an almost metallic highly doped p-type semiconductor with two unfilled holes per formula unit. Replacing two Cu atoms with Zn, will provide additional 4s electrons which fill the holes on the top of the valence band and push the Fermi level up into the band gap which results in insulating behavior. This has been previously confirmed in other reports [3] with assuming the Zn atoms substituting four fold Cu-I sites. But, to the best of my knowledge, replacing two Zn atoms in threefold Cu-II site has not been reported which is reported in figure 8.11a.

Note that in WIEN2K package, the DOS is per unit-cell and partial density of states are only from atomic spheres and it does not add up to the total density of states because there is the interstitial part which is typically 10 to 20 percents. In WIEN2K, the band gap is smaller than the

DFT results

Chemical shift	Cu-I	Cu-II
Zn on Cu-II site	877	1328
Zn on Cu-I site	771	1257

Experimental results

Chemical shift	Cu-I	Cu-II
$Cu_{10.6}Zn_{0.5}Ni_{0.9}Sb_4S_{13}$	930	1870
$Cu_{10}Zn_2Sb_4S_{13}$	1033	2000

Table 8.1: DFT calculated chemical shifts for $Cu_{10}Zn_2Sb_4S_{13}$ sample in the case Zn replaces Cu atoms on Cu-I and Cu-II sites compared to experimental results for $Cu_{10}Zn_2Sb_4S_{13}$ and $Cu_{10.6}Zn_{0.5}Ni_{0.9}Sb_4S_{13}$.

real value which could be originated from native defects in the crystal structures of this materials. The plotted DOS can be different than band structure because the WIEN2K calculated linearized augmented plane wave separately for DOS and band structure calculations which in band structure calculations the tetrahedron-method broadening applied which might make slight differences than DOS calculations due to degeneracy of two eigenvalues are on two k-points ($\Gamma - X$) or due to back-folding both eigenvalues are at Γ.

The chemical shifts in both scenarios have been calculated. Calibration of calculated ^{63}Cu chemical shifts were normalized based on the computed CuCl NMR standard and the results are provided in table 8.1. In addition the calculated EFG's are 0.64×10^{21} V/m^2 and 6.64×10^{21} V/m^2 (corresponding to $\nu_Q = 1.73$ MHz and $\nu_Q = 17.7$ MHz) . The calculated chemical shifts are somewhat different from the experimental observations described above for $Cu_{10}Zn_2Sb_4S_{13}$, as well as the similar experimental result obtained for $Cu_{10.6}Zn_{0.5}Ni_{0.9}Sb_4S_{13}$ (section 8.1.1), with the trend of Cu-I vs Cu-II shifts reversed in the calculated results vs. experiment. As was noted earlier, the experimental shifts for these two compositions also differ from those of $Cu_{12}Sb_4S_{13}$ by more than would be expected based on simple filling of the valence-band holes in a rigid-band picture. Thus although the crystal structures can be fitted rather well by assuming these compositions adopt the unchanged room-temperature $Cu_{12}Sb_4S_{13}$ structure (figure 8.2), we expect that additional random local distortions may be responsible for these differences. A likely scenario is provided in the recent observation [82] that the low-temperature insulating phase of $Cu_{12}Sb_4S_{13}$ is characterized by coherent, frozen-in Jahn-Teller distortions involving one of the S sites relative

to its surrounding Cu-I ions. The occurrence of small distortions in a random way within the nominally insulating substituted phases may also account for the differences in chemical shift observed here by modifying the electronic structure relative to the undistorted phase.

The lineshapes at lower temperatures are shown in Figure 8.12. As shown in this plot the line shapes are becoming broader as the temperature is decreased. In the analysis section, we will further discuss the full width half maximum (FWHM) of the line shape in terms of a Curie-like model, showing in the inset of the figure providing a quantitative value for magnetization impurity of the Cu atoms.

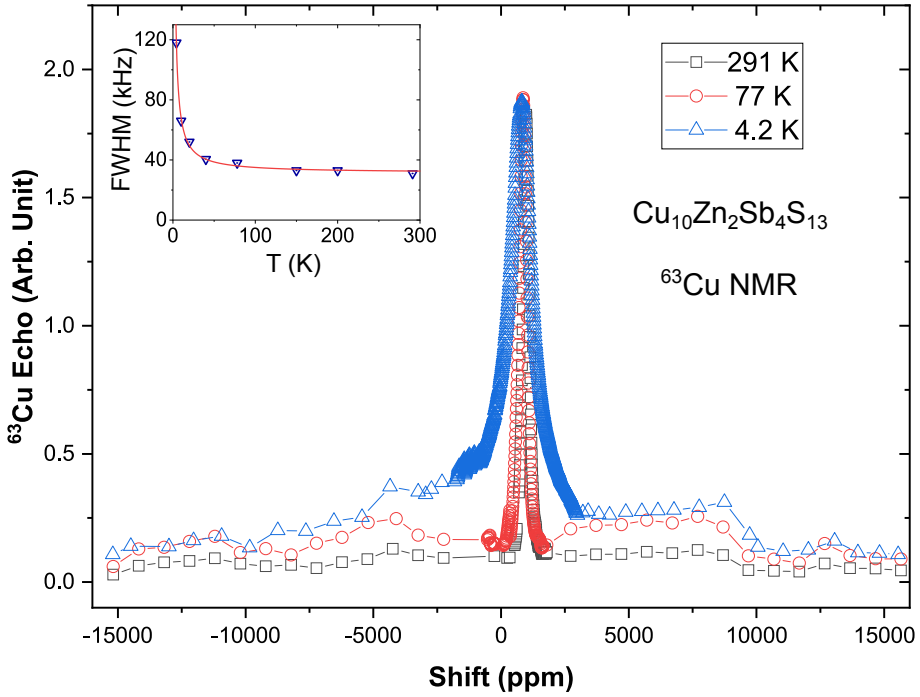

Figure 8.12: $Cu_{10}Zn_2Sb_4S_{13}$ lineshapes at different temperatures. The inset shows the FWHM of the central part of the lineshapes versus temperature and a corresponding Curie model fitting.

8.1.5 $Cu_{12-y}Sb_{4-x}Te_xS_{13}$

In natural minerals, the Sb sites in tetrahedrite can be replaced by Bi, As or Te elements. In the Te substitution case, the solid solution series continues according to the chemical structure

$Cu_{12}Sb_{4-x}Te_xS_{13}$ up to x=2. However, raising the extent of Te up to x=4 is possible but this leads to diminished Cu concentration, and generates another end member of tetrahedrite class titled as golfieldite[55] with chemical structure $Cu_{10}Te_4S_{13}$. This can be understood in terms of Cu vacancies forming spontaneously (formal composition $Cu_{10}(Vac)_2Te_4S_{13}$) to keep charge balance as the addition of the electron donor Te atoms expected what is required to balance the hole density.

The electronic band structures of the $Cu_{12}Sb_{4-x}Te_xS_{13}$ compounds [113] shows that the two sites per formula unit should be substituted to achieve semiconducting behavior i.e. for x = 2.0, and the energy gap decreases comparing to undoped tetrahedrite. Therefore, varying the Te content gradually evolve the compound from metallic to semiconducting with increasing Te content.

Figure 8.14 gives the temperature dependence of the ^{63}Cu spectra for $Cu_{12}Sb_{4-x}Te_xS_{13}$ (x= 1, 2). These are expected to be due to Cu-II. Starting at room temperature, lineshape shows rather little change as the temperature is decreased. The $1/T_1T$ behavior is also plotted in figure 8.13 with an upturn in $1/T_1T$ for x=1 sample indicating that the Cu ions remain relatively mobile for this composition.

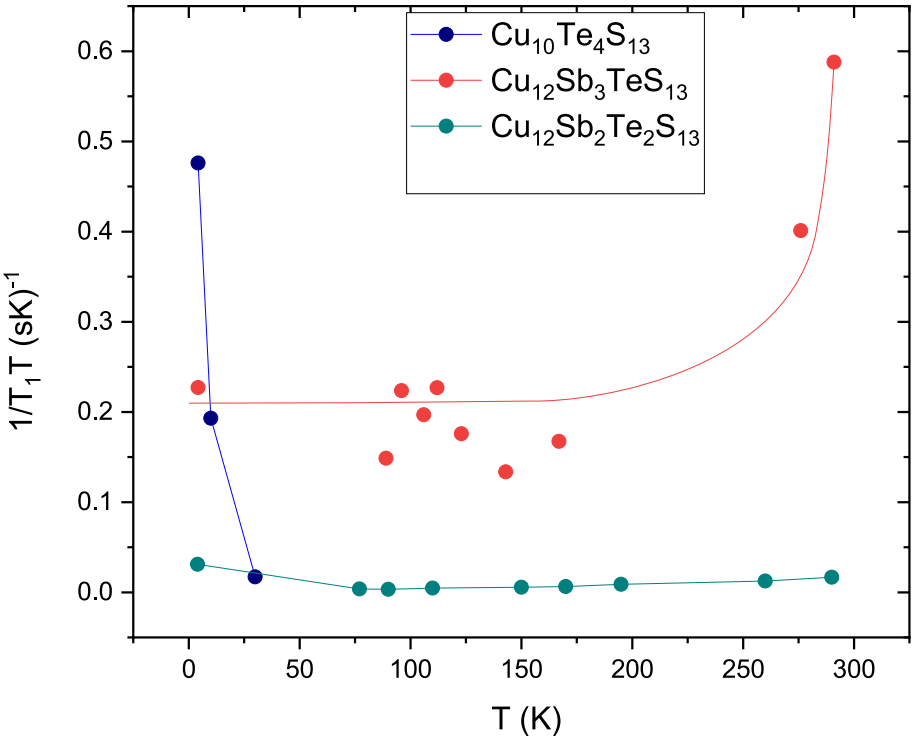

Figure 8.13: ^{63}Cu $1/T_1T$ for $Cu_{12}Sb_{4-x}Te_xS_{13}$ and $Cu_{10}Te_4S_{13}$ samples.

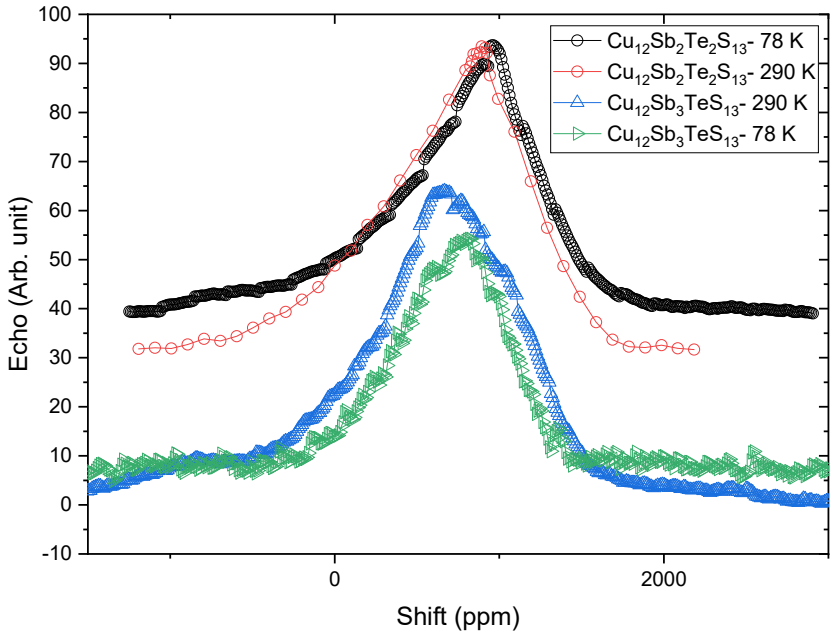

Figure 8.14: ^{63}Cu spectra for $Cu_{12}Sb_{4-x}Te_xS_{13}$ at various T.

8.1.5.1 $Cu_{10}Te_4S_{13}$

Goldfieldite, with ideal $Cu_{10}Te_4S_{13}$ chemical formula, is the tellurian end-member of the tetrahedrite-tennantite solid-solution series. As described above, it is believed that adding two Te to an undoped sample will provide enough electrons to fill the holes, and adding four Te will make a composition with two Cu vacancies with $Cu_{10}Te_4S_{13}$. XRD results confirm the presence of two defects in occupancy of three fold Cu-II sites[55] in the unit cell. Our $Cu_{10}Te_4S_{13}$ sample was synthesized by direct reaction of a stoichiometric mixture of the elements sealed under secondary vacuum in quartz ampules and we expect to see consistent behavior of lattice constant in Te rich compounds [113].

The 4K lineshape is shown in Figure 8.15. There are two obvious broad peaks which could be due to two different phases or different sites. However, at higher temperatures the signal disappears. Rapidly increasing the temperature could initiate the superionic Cu motion in this sample leading dephasing the NMR signal with no signal observed at high temperatures, however this is

very low temperature for such behavior, and the T_1 relaxation (figure 8.13) is distinct from the corresponding behavior of $Cu_{14}Sb_4S_{13}$. The singular behavior of this material suggests a need for further investigation.

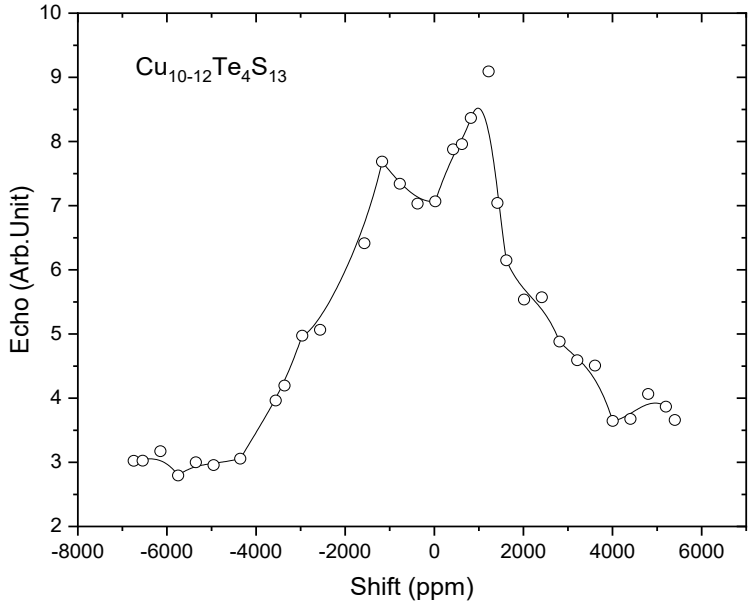

Figure 8.15: $Cu_{10-12}Te_4S_{13}$ ^{63}Cu NMR lineshape at 4K.

The $^{63}T_1$/ $^{65}T_1$ ratio at 4K is 0.89, thus indicating that the result is dominated by a quadrupole contribution and thus suggesting that rattling also is significant factor for this compound. $1/T_1T$ is plotted in figure 8.13

8.1.6 $Cu_{12-x}Mn_xSb_4S_{13}$

The ^{63}Cu lineshape of the $Cu_{12-x}Mn_xSb_4S_{13}$ sample for (x=1, 2) at 77 K is plotted in figure 8.16. The line shape is very broad for this sample which is due to the magnetic characteristics of the Mn ions in this sample. The manganese in this sample is in the Mn^{2+} ($3d^5$) high-spin configuration. However, because of the magnetic broadening as well as the usual thermal effects there is not

enough signal at high temperatures to obtain the data. The lineshape at 77 K is plotted in 8.16. The T_1 at 77 K is 40 ms.

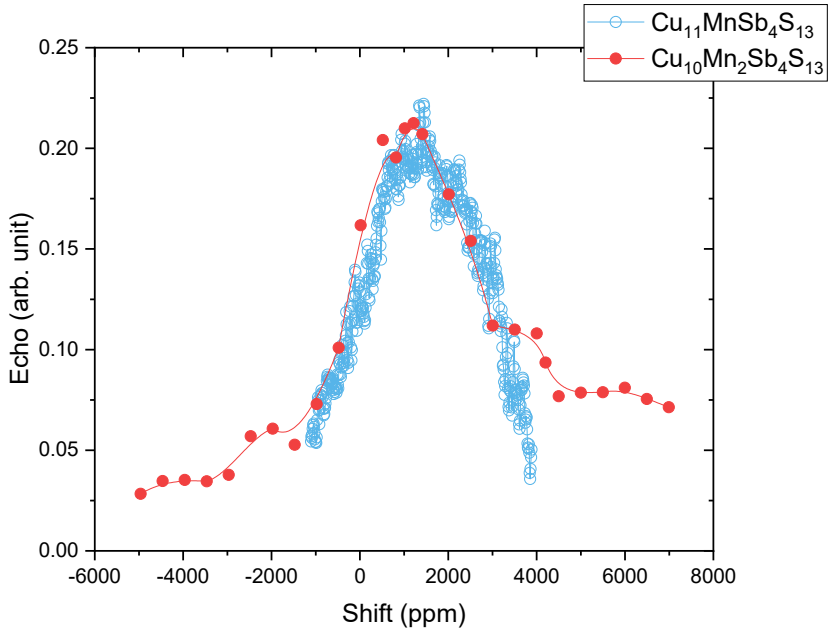

Figure 8.16: $Cu_{12-x}Mn_xSb_4S_{13}$ ($1 \leq x \leq 2$) ^{63}Cu NMR lineshapes at 77 K.

8.2 Discussion and Analysis

8.2.1 Rattling

Figure (8.5) illustrates the ^{63}Cu lineshapes of the $Cu_{10.6}Zn_{0.5}Ni_{0.9}Sb_4S_{13}$sample obtained at 4.2 K, 77 K, and 291 K. Similar spectra (not displayed) were acquired for ^{65}Cu. The spectra are superpositions of $m = -1/2 \leftrightarrows m = 1/2$ transitions of the two different sites (12e, 12d sites in the tetrahedrite structure).

A multi-exponential function $S(t) = \alpha_0(1 - \frac{2}{10}e^{(-t/T_1)} - 1.8e^{(-6t/T_1)})$ was used to fit the nuclear magnetization recovery curve similar to what was used for unsubstituted tetrahedrite. By investigating the isotopic ratio fitted of the overall relaxation rate, we found the dominance of the

quadrupole mechanism in doped samples. Within the framework of the relaxation theory, a ratio close to $\frac{^{63}T_1}{^{65}T_1} = (\frac{Q_{65}}{Q_{63}})^2 = 0.86$ can indicate the quadrupole dominance (section 6.5).

The T_1 relaxation rates for various doped samples at room temperature were measured for each isotope. Table 8.2 shows the results; for heavier Ni content, magnetic fluctuations lead to an enhanced magnetic contribution. On the other hand, we find a clear dominance of the quadrupole mechanism in $Cu_{10}Zn_2Sb_4S_{13}$, $Cu_{12}Sb_3TeS_{13}$, and $Cu_{12}Sb_3TeS_{13}$ samples. Further investigation on $\frac{^{63}T_1}{^{65}T_1}$ for $Cu_{10}Zn_2Sb_4S_{13}$ and $Cu_{10.6}Zn_{0.5}Ni_{0.9}$ at lower temperatures gives the results shown on the inset of figure 8.17. The overall behavior of the relaxation times indicates the dominance of the quadrupole mechanism for these compositions in all temperatures.

290 K	$^{63}T_1$ (ms)	$^{65}T_1$ (ms)	$^{63}T_1/^{65}T_1$	M/Q
$Cu_{10.6}Zn_{0.5}Ni_{0.9}Sb_4S_{13}$	18.4	19	0.96	Q
$Cu_{10}Zn_2Sb_4S_{13}$	180	207	0.83	Q
$Cu_{10}ZnNiSb_4S_{13}$	63	57	1.11	M
$Cu_{10}Ni_2Sb_4S_{13}$	3.86	3.27	1.18	M
$Cu_{12}Sb_3TeS_{13}$	5.85	6.34	0.92	Q
$Cu_{12}Sb_2Te_2S_{13}$	231	258	0.9	Q

Table 8.2: Spin lattice relaxation times and dominance of magnetic and quadrupole contributions in doped tetrahedrites at room temperature based on observed isotropic ratio.

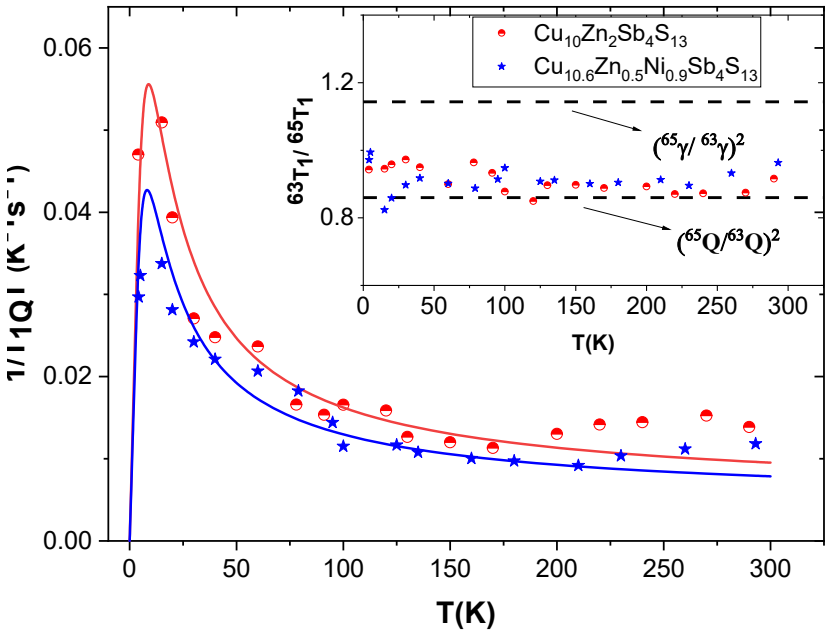

Figure 8.17: Quadrupole NMR relaxation rate for ^{63}Cu in substituted tetrahedrite samples compared with the fitted anharmonic model (solid curve) for Cu-II site in $Cu_{10.6}Zn_{0.5}Ni_{0.9}Sb_4S_{13}$ and $Cu_{10}Zn_2Sb_4S_{13}$ samples. Inset is $^{63}T_1/^{65}T_1$.

I used the same method explained in section 6.6 to study the anharmonicity. The fitted curves are shown in figure 8.17 and the fits parameters are $\beta = 45$, $\omega_{00} = 22\ K$, $\Gamma_0 = 3.2\ K$ and $\omega_0 Re(\Pi) = -(6\ K)^2$, while the fitting results for $Cu_{10.6}Zn_{0.5}Ni_{0.9}Sb_4S_{13}$ are $\beta = 47$, $\omega_{00} = 19.35\ K$, $\Gamma_0 = 0.51\ K$ and $\omega_0 Re(\Pi) = -(1.0\ K)^2$, these corresponding to anharmonic potential wells given by,

$$V_{Zn_{0.5}Ni_{0.9}}(x) = (-7.6\ \text{J/m}^2)\ x^2 + (2.02 \times 10^{22}\ \text{J/m}^4)\ x^4 \tag{8.1}$$

$$V_{Zn_2}(x) = (-9.4\ \text{J/m}^2)\ x^2 + (2.84 \times 10^{22}\ \text{J/m}^4)\ x^4. \tag{8.2}$$

Our measurements of the rattling characteristic were also analyzed to get the fitted potential. These result in room-temperature thermal parameters for the Cu-II of 0.029 Å^2 and 0.034 Å^2, corre-

sponding to room temperature rms displacements of 0.17 Å and 0.18 Å for $Cu_{10}Zn_2Sb_4S_{13}$ and $Cu_{10.6}Zn_{0.5}Ni_{0.9}Sb_4S_{13}$ respectively. This compares to our value 0.14 Å (section 6.6) which was discussed before for $Cu_{12}Sb_4S_{13}$. The fitted potential and a comparison with $Cu_{12}Sb_4S_{13}$ is shown in figure 8.18. The larger displacement of the Cu-II leads to more phonon dispersion and larger thermal conductivity κ which consequently leads to larger figure of merit. The result show a larger rattling for both of these compounds as compared to what we obtained for undoped $Cu_{12}Sb_4S_{13}$ sample.

Our results show that there is largest amount of rattling for $Zn_{0.5}Ni_{0.9}$ sample which agrees with lowest thermal conductivity observed [3] in this material. This points to the conclusion that the rattling is the main effect controlling the scattering of phonons. The lattice constants for $Cu_{12}Sb_4S_{13}$ and $Zn_{0.5}Ni_{0.9}$ samples are almost identical (figure 8.3) therefore, this indicates that the larger rattling in $Zn_{0.5}Ni_{0.9}$ sample is due to electronic effects of the neighbor bonds in Cu-II sites. This is somewhat different from the conclusion [69] that it is the space provided locally by the atomic cage that controls the rattling. Note that displacement of Cu-II is slightly smaller than obtained from XRD in the reference [67], however, we know that XRD and neutron scattering are susceptible to static disorder defects. Thus, the NMR technique can be particularly useful in deconvoluting these effects since it is sensitive specifically to dynamical effects. We found 0.17 Å and 0.18 Å for $Cu_{10}Zn_2Sb_4S_{13}$ and $Cu_{10.6}Zn_{0.5}Ni_{0.9}Sb_4S_{13}$ which is very comparable to the *ab initio* result for undoped sample [78] and it does show that there is enhanced rattling for Zn doped materials.

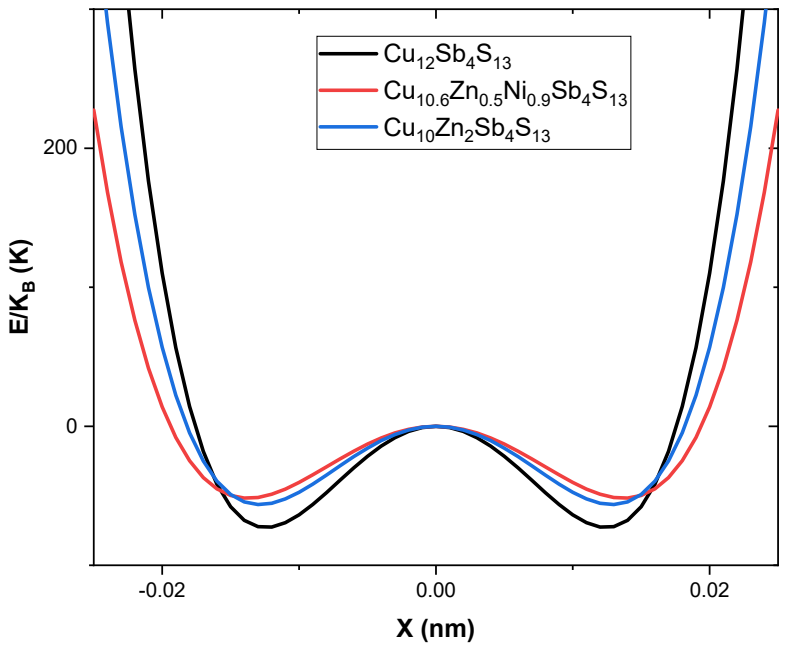

Figure 8.18: Fitted 1D double-well potential for Cu-I site in $Cu_{10}Zn_2Sb_4S_{13}$ and $Cu_{10.6}Zn_{0.5}Ni_{0.9}Sb_4S_{13}$ samples and compared with result obtained for $Cu_{12}Sb_4S_{13}$ sample.

These results are in good agreements with low thermal conductivity observed in these materials and indicates that rattling is the main reason for low thermal conductivity in tetrahedrites.

8.2.2 MST and Atomic Motion

The temperature dependence of the total shift obtained by finding the center of gravity for each spectrum and the result is displayed in figure 8.19, for which a significant contribution is the Knight shift (K) which is correlated to the local spin susceptibility detected by the nucleus. These data were measured on the Cu-I peak of the NMR spectra for the various samples as shown. In Te, Mn, Zn and Ni doped and Zn, Ni co-doped teterahedrite samples, as the temperature increases, the peak at a common shift position near 950 ppm stays constant with width decreasing. While Cu-I is in the metallic phase of the undoped $Cu_{12}Sb_4S_{13}$ and known to show a negative Knight shift above the Metal Semiconductor Transition because of the core polarization mechanism (chapter 6), it is reasonable that this peak should have a more positive shift in the charge-balanced Mn, Zn,

Te, and Cu rich as well as Zn-Ni co-doped sample vs. unsubstituted $Cu_{12}Sb_4S_{13}$ due to reduced K assuming substitution reduces the carrier density in each case.

The results demonstrate that the phase transition is absent in most of these doped and co-doped samples. However, in $Cu_{10.6}Zn_{0.5}Ni_{0.9}Sb_4S_{13}$ there is still a slight change of shift observed which indicates that the MST is not completely suppressed in this sample. Note that slight change at the MST still occurs at the same temperature as $Cu_{12}Sb_4S_{13}$. The unchanging T_c for partial tetrahedrite substitution was previously seen in magnetic susceptibility measurements [108], and the NMR results confirm that this is a bulk phenomenon, not tied, for example, to a minority phase of unsubstituted tetrahedrite within the samples. Since substitution induces large changes in carrier density, this result indicates that the transition is not driven by electronic features such as Fermi surface nesting. Rather, it appears that the entropy of random local distortions, which can become frozen into a regular configuration at low temperatures in unsubstituted $Cu_{12}Sb_4S_{13}$, is the dominant driving force for this transformation.

As shown in figure 8.19, the undoped sample in the metallic state has a total shift $\Delta f = \delta_{ch} + K$ of approximately 600 ppm and considering that the Zn_2 sample is charge balanced, the total shift change between pure tetrahedrite and Zn_2 tetrahedrite (which shift is mainly a chemical shift) is around 300 ppm.

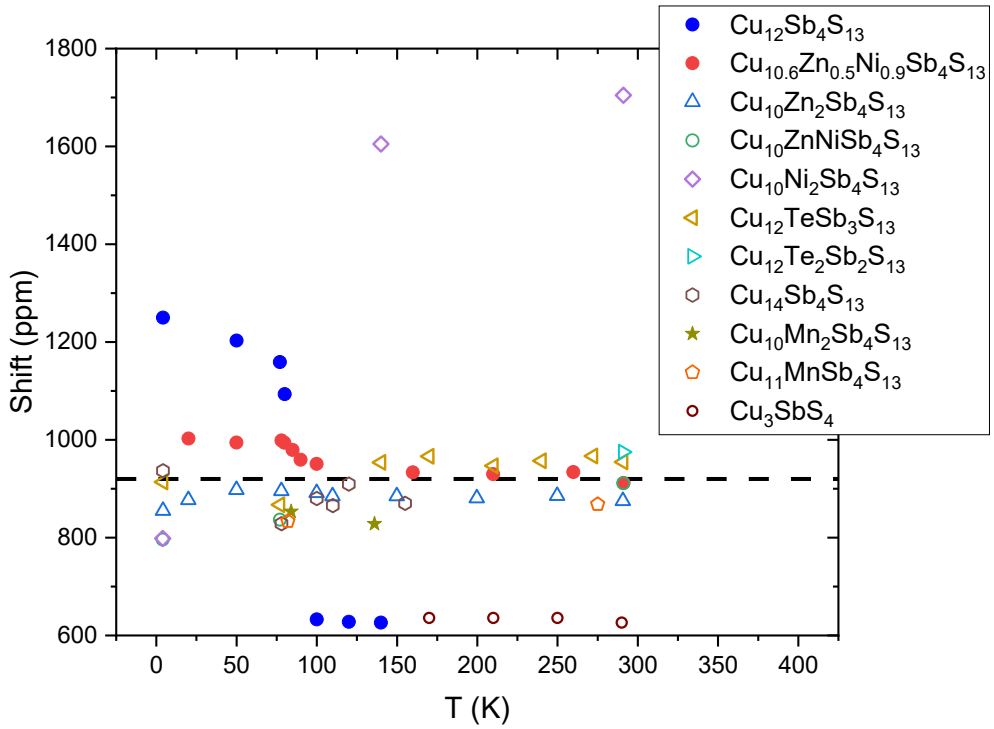

Figure 8.19: The ^{63}Cu NMR shifts of the Cu-I site for various dopants vs temperature. A schematic dashed line is drawn to show the common shift position.

Figure 8.13 show the $1/T_1T$ for Te doped samples. From the observed behavior we conclude that $Cu_{12}Sb_3TeS_{13}$ exhibits slow ionic motion below room temperature since $1/T_1T$ is strongly enhanced at high temperatures in much the same way as $Cu_{12}Sb_4S_{13}$ and $Cu_{14}Sb_4S_{13}$ samples (chapter 7).On the other hand, for $Cu_{12}Sb_2Te_2S_{13}$ the constant $1/T_1T$ indicates that Cu ions become relatively immobilized. We also find that the signal amplitude has not decreased based on increasing t_{delay}. These indicates that ionic motion is reduce as the substitution of Te increases in the sample. This indicates a larger activation energy required for hopping in heavily doped samples. Indeed, in all Zn and Ni-doped samples we find that the NMR echo signal is observed essentially unchanged at temperatures to room temperature, in contrast to the disappearance of the echo signal in $Cu_{12}Sb_4S_{13}$ and $Cu_{14}Sb_4S_{13}$ (chapter 7). The NMR technique is sensitive to to dynamics on a time-scale of 100 μs, and thus these results indicate the absence of even very slow hopping at am-

bient temperatures, an important issue for potential thermoelectric device stability and design. We conclude that the activation energy is increased to a value significantly larger than the 280 meV estimated for $Cu_{12}Sb_4S_{13}$.

8.2.3 Magnetism

The ^{63}Cu lineshape for undoped tetrahederite $Cu_{12}Sb_4S_{13}$, at low temperatures, has enhanced broadening (Figure 6.3) which is consistent with the presence of dilute paramagnetic moments. To estimate the maximum defect density, we note that increase in line breadth relative to 77 K is approximately 1000 ppm (full-width half maximum), and use established relations [186] for dipole broadening due to dilute paramagnetic moments. Assuming 2 μ_B local moments, this gives a defect concentration 0.0014 per Cu ion. This matches previous results [149] indicating a nonmagnetic configuration for $Cu_{12}Sb_4S_{13}$, with holes in the Cu d-based valence band remaining itinerant rather than forming localized Cu^{2+} moments, and does not appear to be compatible with fully-magnetic Cu-II ions [187], although a singlet configuration for site-II below T_c remains possible, and would still allow observation of the site-I resonance.

Figure 8.12 shows the ^{63}Cu line shape of $Cu_{10}Zn_2Sb_4S_{13}$ at different temperatures. The line shapes are slightly asymmetric, however, the full width at half maximum (FWHM) obtained from the line widths is 308 ppm (31 kHz) at room temperature, increasing as T is lowered. We recorded the FWHM as a measure of the broadening of the line shapes (inset of figure 8.12). These FWHMs were fitted to a Curie-like model, FWHM $\propto \frac{C}{T} + B$, where B is a temperature dependent background. The NMR linewidths due to dilute magnetic impurities can be calculated [188] when the NMR broadening is significantly impacted by random dipole field due to the impurity spins. In this theory, the spectra's width is proportional to the average spin moment which provides a Curie-like contribution to the linewidth. Based on this model, the FWHM, $\Delta\nu$, due to substitutional defects with spin $\overrightarrow{S}$ and density f, can be given as

$$\Delta\nu = \frac{2}{\sqrt{3^5}} \frac{\mu_0 \mu_B \gamma_n g f}{V} \langle S_z(T) \rangle \tag{8.3}$$

where, $\langle S_z(T)\rangle = \frac{\mu_B g^2 J(J+1)B}{3k_B T}$ is the average moment, and V the volume per formula unit. We fixed $g = 2$. Our fits show an impurity concentration of $f = 0.058$ per formula unit in the Zn_2 sample. These must be either due to some small density of impurity atoms or a small percentage of the Cu being intrinsically magnetic in which case since there are 10 Cu atoms per unit that corresponds to $f = 0.0058$ of the relative fraction of the Cu are being magnetic. This is slightly larger than approximate limiting value obtained for pure tetrahedrite (above) which also corresponds to a very small fraction of the dilute moments. This places a significant limit on the possible density of magnetic Cu^{2+} ions and shows that only a small number of Cu to be magnetic. The same Curie behavior observed in magnetic susceptibility [102], and confirm that the defects are randomly distributed in the sample.

FWHM results were also fitted for other samples, as shown in fig. 8.20. In some cases only a few points were used for the fitting, however the results provide a useful estimate of the content and behavior of the local moments in these samples.

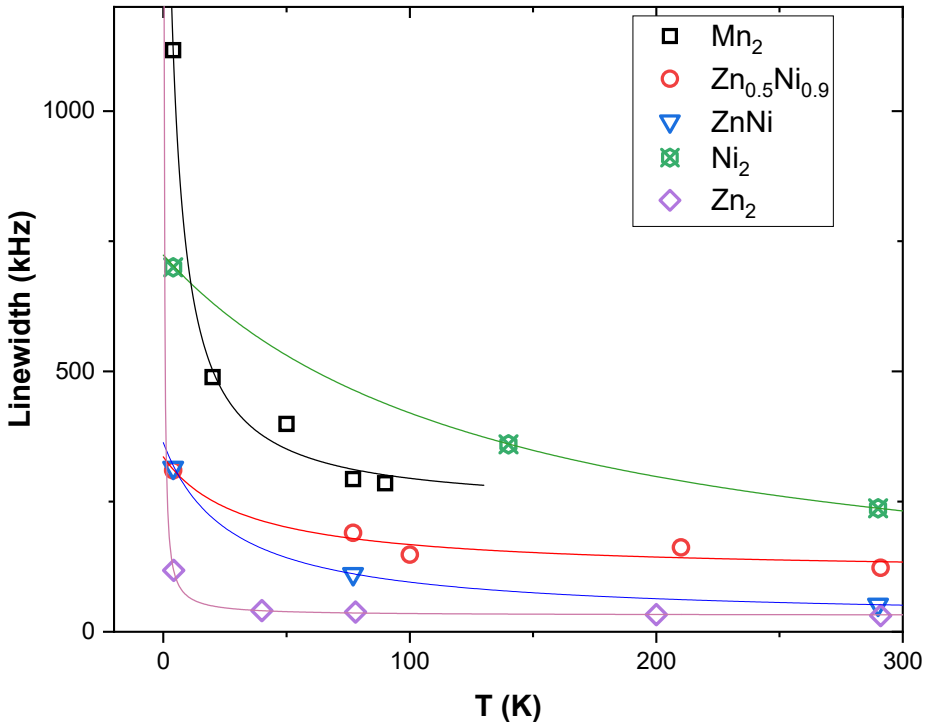

Figure 8.20: FWHM vs temperature for tetrahedrite samples as shown, along with Curie-type curves described in text.

The ^{63}Cu spectra in Mn_2 samples shows a similar increase in broadening in low temperatures and implementing the Curie model for FWHM, yields an impurity concentration of f = 0.29 per formula unit. This is derived with considering $J = 5/2$ in equation 8.3, in accordance with reported bulk susceptibility results [65] pointing a moment per Mn in this range. The fitted Néel temperature is 8K, also in reasonable agreement with the result from bulk susceptibility obtained in this work. However, considering $J = 1$ leads to an impurity concentration of f = 0.55.

The same analyses applied to the ^{63}Cu spectra in $Zn_{0.5}Ni_{0.9}$, ZnNi, Ni_2 samples, implementing the Curie-Weiss model for FWHM, yields an impurity concentration of f = 0.112, 0.147 and 15.4 per Cu ion, respectively, with T_c = -33, -27, -133 K. Note that we fixed $J = 1$ in accordance with previously established results [91, 88] from bulk susceptibility indicating a moment of this size per Ni. The fitted Néel temperatures for the $Zn_{0.5}Ni_{0.9}$ and ZnNi substituted samples are

also in excellent agreement with the value of $\sim$ 30K obtained for a Ni1-substituted sample [88], which helps to validate the dilute-moment approach used here for NMR linewidths. For $Zn_{0.5}Ni_{0.9}$ and ZnNi substitution the moment densities correspond to 1.3 and 1.5 per formula unit, in good agreement with the known compositions of these samples within the approximations inherent in this method. This provides confirmation that these moments are distributed uniformly throughout the materials. Also the results correspond to random dipole magnetic fields due to these ions as the dominant local-magnetic effect sensed by the Cu nuclei, which tends to rule out any significant exchange-related polarization of carriers in the valence band, as would be expected for a magnetic semiconductor.

The situation is different for the Ni_2 sample, for which the analysis used here indicates an unphysically large moment density. In part this may be because the dilute-moment approximation of equation (8.3) is not completely valid, but the enhanced local fields also point to the influence of electron-mediated interactions for this composition XRD results.

XRD results (figure 8.3) shows that increasing the Ni content, will decrease the lattice constant from $a = 10.3224\,\text{Å}$ to $a = 10.31\,\text{Å}$ confirming that Ni are being substituted into the Cu sites. However, Ni moments apparently interact more directly in the concentrated-Ni sample, a result shown also by the distinct T_1 for Ni_2.

The $1/T_1$ results are shown in figure 8.21. As previously demonstrated (Table 8.2) the dominant process for the relaxation in this case is magnetic fluctuations, however the temperature dependence in this case is distinct, with approximately constant $1/T_1$ (rather than $1/T_1T$). This is the behavior expected [189] for strongly coupled local moments, for which case the fluctuation spectrum is proportional to the exchange frequency, and hence independent of the temperature.

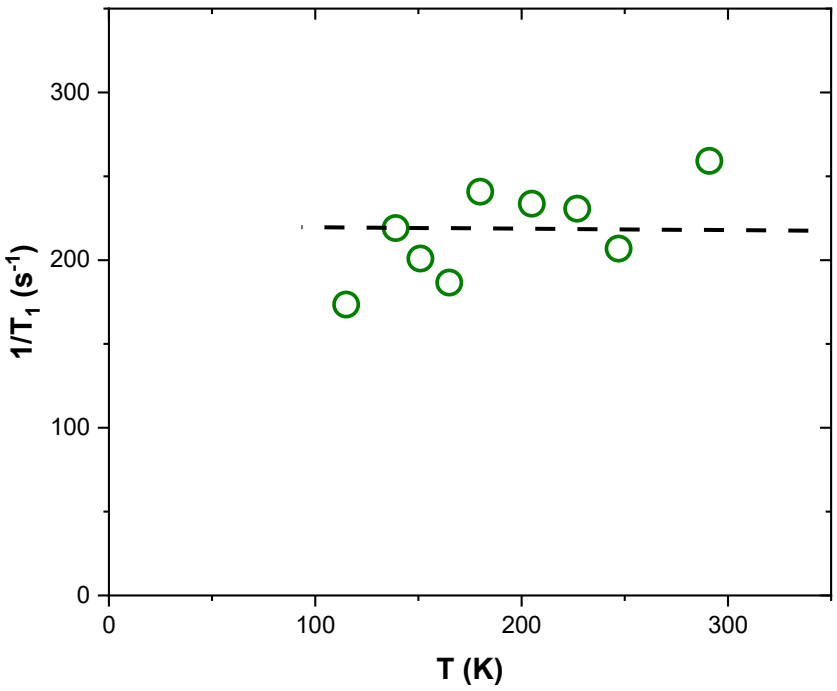

Figure 8.21: ^{63}Cu T_1 for $Cu_{10}Ni_2Sb_4S_{13}$ sample vs. temperature. Dashed line shows T-independent behavior corresponding to exchange-coupled fluctuating local moments.

The Curie-Weiss method applied to the lineshapes of $Cu_{10}Mn_2Sb_4S_{13}$ at low temperatures gave $f = 0.54$ per formula unit. While in principle the method may detect the moments on Cu as well as Mn, certainly the number is less than the expected 2 per formula unit, this might show that all the manganese ions are not magnetic. It is also possible that the result corresponds to clustering of the Mn ions, effectively reducing the apparent moment sensed through NMR linewidths. Further studies might help to clarify this situation.

8.3 Shifts

The temperature dependent shifts for all samples are shown in Fig. 8.19. In our results, we find that all the shifts for substituted samples are about the same, excluding the strongly magnetic Ni_2. Among these shifts, it seems most likely that the common shift value corresponds to a chemical

shift, with the Knight shift due to charge carriers giving a much smaller contribution. A simple model for such behavior [179] is to assume a parabolic band edge. In this case, it is easy to show that the Knight shift is expected to vary vs conduction electron density as $n^{1/3}$. The Te_1 and Te_2 materials provide a good example: with the approximate 300 ppm difference between unsubstituted $Cu_{12}Sb_4S_{13}$ and Te_2 assumed to result from the reduction of K to zero in the charge-balanced Te_2, Te_1 with half the reduction of carriers would be expected to exhibit a Knight shift differing by 240 ppm from that of Te_2. This also sets the scale for the variation in Knight shift that might be expected for the different compositions observed here. The much more uniform set of observed shift is unlikely to result from the combination of different values of Knight shifts and chemical shift for each compound. Rather, we assume that the observed shift of about 950 ppm corresponds to a distinct chemical shift for substituted tetrahedrites, with rather small added Knight shifts. Generally in semiconducting materials of this type it is often observed that native defects can be spontaneously formed in order to take advantage of the electronic energy gained by locating ε_f at the bandgap; a good example is provided by the spontaneous vacancies appearing in $Cu_{10}Te_4S_{13}$ as described above. Thus the common set of shifts observed here seems likely to correspond to a reduction in carrier density in these materials according to such a mechanism.

As it mentioned above, making an approximation that the DOS has a parabolic band-edge behavior with $g(\varepsilon) \propto \sqrt{\varepsilon}$ then the Knight shift is $K \propto n^{\frac{1}{3}}$. This is the model that was just introduced for the other materials explaining small amount of Knight shift in charge balanced tetrahedrites. This can be modeled as Ni impurity band can hold two empty states per Ni and 1.8 in total for $Ni_{0.9}$ and substituting Zn will provide 0.5 electrons [91], considering unsubstituted tetrahedrite with two unfilled holes in valence band makes the $Zn_{0.5}Ni_{0.9}$ sample to have $n = 2.4 - 1.8 = 0.6$ charge carriers. A simple comparison with $Cu_{12}Sb_4S_{13}$ tetrahedrite in metallic state with $K_{Cu_{12}} = 300$ ppm $\frac{K_{Zn_{0.5}Ni_{0.9}}}{K_{Cu_{12}}} = 0.3^{\frac{1}{3}}$ leads to $K = 200$ ppm, which makes the total shift of 700 ppm which implication is the same as in the other materials in which the Knight shift also appears to be smaller than predicted.

Our DFT calculations (figure 8.11) show that the band-edge in the case of Zn_2 doping, similar

to undoped tertahedrite, is still dominated strongly by Cu d-orbital electrons. Therefore the Cu NMR Knight shift still should be a good measure of the hole density. This tend to rule out a significant rearrangement of states at the band edge as an alternative explanation of the uniformly small Knight shift. We are in the process of calculating the results for Te doped sample to compare and make more assertive analysis.

There has been uncertainty about the effect of Ni substitution, with indications that substitution of Ni atoms also will fills the hole states in the valence band similar to Zn or Te, although with the expected valence it is also suggested that substitution of nickel will add holes and introduce additional unoccupied states at the top of the valence band (based on impurity band model explained above), or perhaps the effect is one of an increase in the effective mass [102, 190, 88]. It is also suspected from electronic resistivity measurements that the number of charge carriers is reduced as the number of Ni dopants increases [91], although it has been very difficult to obtain the carrier density in a more direct way by Hall measurements [102]. For relatively small Ni substitution in the ZnNi and $Zn_{0.5}Ni_{0.9}$ samples, the uniform shifts observed here point to small carrier density in these materials. More precisely, the results are an indication that the electron density of states at ε_f is small, which could correspond either to ε_f moving to the edge of the valence band, or to the formation of a pseudogap such as might be associated with Ni-related states appearing at the top of the valence band.

The Ni_2 result is quite different, as seen in Fig. 8.19. Here the NMR shifts are large, and out of the range of the shifts of the other substituted materials. Generally, this seems to indicate a distinct electronic behavior for the case of Ni_2, which as noted above also exhibits more strongly magnetic behavior than the other materials. This appears to confirm the suggestion [102] that ε_f in this case should be located in a band of Ni-based states positioned above the valence band. Similar concentration-dependent behavior was recently indicated based on transport measurements in Fe-substituted tetrahedrites [191] which apparently exhibit hopping conductivity within a Fe-based impurity band for cases of larger Fe substitution. Note also the contrast with Mn-substituted materials, which have NMR shifts (figure 8.19) in line with those of the other nonmagnetic tetrahedrites,

despite the expected large moments for Mn.

9. SUMMARY AND CONCLUSIONS*

In summary, from investigations of $^{63}\mathrm{Cu}$ and $^{65}\mathrm{Cu}$ NMR in unsubstituted $Cu_{12}Sb_4S_{13}$, we found that above the metal-insulator T_c, which is accompanied by a large Knight shift change, there is a progressive loss of the $Cu_{12}Sb_4S_{13}$ signal and dominance of the Cu_3SbS_4 phase at high temperatures. The Cu-II site exhibits a large reduction in electric field gradient (EFG), while Cu-I changes from a very small EFG/high symmetry configuration to a lower symmetry arrangement at room temperature. This shows that there is a change in the local atomic environments at these temperatures, probably corresponding to the development of a static split-site condition. DFT calculations confirmed that the low-EFG configuration corresponds to the undistorted configuration identified by crystallography. The T_1 displays the presence of a strong quadrupole relaxation mechanism both above and below T_c. Analysis indicates that anharmonic rattling type motion is the main reason for this behavior. A double well anharmonic potential provides a good fit for the data, providing a measure of the rattling amplitude, and indicating that the dynamical behavior persists below T_c.

In a set of Cu NMR measurements on $Cu_{12+x}Sb_4S_{13}$ tetrahedrites, we identified the NMR signatures of the phase segregation into Cu-poor ($x \approx 0$) and Cu-rich ($x \lesssim 2$) phases. The temperature-independent line-shape for the Cu-rich phase indicates the suppression of the phase transition for this phase. Also by observation of the NMR line shapes, combined with analysis of T_2 and T_1 relaxation behavior, we obtain a measure of Cu-ion dynamics in these phases at low temperatures. We find that the Cu ions are particularly mobile in the Cu-rich phase, with a fitted activation energy of 145 meV for ion hopping. The $x \approx 0$ phase exhibits a larger barrier for ionic motion, however in both phases we find that there is a significant rate of ionic motion at temperatures below room

*Part of this section is reprinted with permission from N. Ghassemi, Y. Tian, X. Lu, Y. Yan, X. Zhou, and J. H. Ross Jr, "*Copper-Ion Dynamics and Phase Segregation in Cu-Rich Tetrahedrite: an NMR Study,* The Journal of Physical Chemistry C, vol. 124, no. 7, pp. 3973-3979, 2020. Copyright (2020) American Chemical Society.

*Part of this section is reprinted with permission from N. Ghassemi, X. Lu, Y. Tian, E. Conant, Y. Yan, X. Zhou, and J. H. Ross Jr, "*Structure Change and Rattling Dynamics in $Cu_{12}Sb_4S_{13}$ Tetrahedrite: an NMR Study,*" ACS applied materials & interfaces, vol. 10, no. 42, pp. 36010-36017, 2018. Copyright (2018) American Chemical Society.

temperature.

We performed Cu NMR measurement of various substituted tetrahedrites including $Cu_{10.6}Zn_{0.5}Ni_{0.9}Sb_4S_{13}$, $Cu_{10}ZnNiSb_4S_{13}$, $Cu_{10}Ni_2Sb_4S_{13}$, $Cu_{10}Zn_2Sb_4S_{13}$, $Cu_{11}MnSb_4S_{13}$, $Cu_{10}Mn_2Sb_4S_{13}$, and $Cu_{12}Sb_{4-x}Te_xS_{13}$ compositions. DFT calculations were also used to model chemical shifts and explore changes in partial DOS for analyzing the results. By modeling the spectra of Zn and Ni substituted materials we found information about the changes in symmetry and electronic behavior in these materials. We observed that all doped materials have similar chemical shift for the Cu-I site which indicates distinct behavior from unsubstituted $Cu_{12}Sb_4S_{13}$. We discussed the results in terms of random local distortions. We also find that a lack of Knight shift for most of the substituted tetrahedrites indicates the importance of native defects or generation of a pseudo gap structure.

We observed that most of the lineshapes exhibit magnetic broadening at low temperatures. Magnetic moment analysis based on the NMR lineshapes agrees with the previously proposed local moment for Ni substitution in low concentrations. On the other hand, Ni_2 spectra analysis indicates more strongly interacting moments with a distinct electronic behavior. We also found that rattling is the main effect controlling the scattering of phonons in Zn-Ni substituted materials and this was confirmed by largest rattling behavior observed in Zn, Ni co-doped sample. Our results indicate that this is not simply tied to expansion of lattice. A lack of Cu-ionic motion was observed in all substituted materials except in $Cu_{12}Sb_3TeS_{13}$, and the MST is suppressed in almost all of the doped materials.

REFERENCES

[1] X. Zhang and L.-D. Zhao, "Thermoelectric materials: Energy conversion between heat and electricity," *Journal of Materiomics*, vol. 1, no. 2, pp. 92–105, 2015.

[2] N. Ghassemi, X. Lu, Y. Tian, E. Conant, Y. Yan, X. Zhou, and J. H. Ross Jr, "Structure Change and Rattling Dynamics in $Cu_{12}Sb_4S_{13}$ Tetrahedrite: an NMR Study," *ACS applied materials & interfaces*, vol. 10, no. 42, pp. 36010–36017, 2018.

[3] X. Lu, D. T. Morelli, Y. Xia, F. Zhou, V. Ozolins, H. Chi, X. Zhou, and C. Uher, "High performance thermoelectricity in earth-abundant compounds based on natural mineral tetrahedrites," *Advanced Energy Materials*, vol. 3, no. 3, pp. 342–348, 2013.

[4] W. Lai, Y. Wang, D. T. Morelli, and X. Lu, "From bonding asymmetry to anharmonic rattling in $Cu_{12}Sb_4S_{13}$ tetrahedrites: When lone-pair electrons are not so lonely," *Advanced Functional Materials*, vol. 25, no. 24, pp. 3648–3657, 2015.

[5] A. F. May, O. Delaire, J. L. Niedziela, E. Lara-Curzio, M. A. Susner, D. L. Abernathy, M. Kirkham, and M. A. McGuire, "Structural phase transition and phonon instability in $Cu_{12}Sb_4S_{13}$," *Physical Review B*, vol. 93, no. 6, p. 064104, 2016.

[6] Y. Xia, V. Ozolins, and C. Wolverton, "Microscopic Mechanisms of Glass-Like Lattice Thermal Transport in Cubic $Cu_{12}Sb_4S_{13}$ Tetrahedrites," *arXiv preprint arXiv:2004.07343*, 2020.

[7] K. Suekuni, K. Tsuruta, T. Ariga, and M. Koyano, "Thermoelectric properties of mineral tetrahedrites $Cu_{10}Tr_2Sb_4S_{13}$ with low thermal conductivity," *Applied Physics Express*, vol. 5, no. 5, p. 051201, 2012.

[8] M. H. Levitt, *Spin dynamics: basics of nuclear magnetic resonance*. John Wiley & Sons, 2013.

[9] C.-S. Lue, *A Nuclear Magnetic Resonance Probe of Fe-V-A1 Intermetallics*. PhD thesis, Texas A & M University, 1999.

[10] S. Kitagawa, T. Sekiya, S. Araki, T. C. Kobayashi, K. Ishida, T. Kambe, T. Kimura, N. Nishi-

moto, K. Kudo, and M. Nohara, "Suppression of nonmagnetic insulating state by application of pressure in mineral tetrahedrite $Cu_{12}Sb_4S_{13}$," *Journal of the Physical Society of Japan*, vol. 84, p. 093701, 2015.

[11] T. J. Seebeck, *Ueber den Magnetismus der galvanischen Kette*. 1822.

[12] J. C. Peltier, "Nouvelles expériences sur la caloricité des courants électrique," *Ann. Chim. Phys*, vol. 56, no. 371, pp. 371–386, 1834.

[13] G. S. Nolas, J. Sharp, and J. Goldsmid, *Thermoelectrics: basic principles and new materials developments*, vol. 45. Springer Science & Business Media, 2013.

[14] G. J. Snyder, "Eric. s. toberer, complex thermoelectric materials," *Nature. Mater*, vol. 7, pp. 105–114, 2008.

[15] T. M. Tritt, "Thermoelectric phenomena, materials, and applications," *Annual review of materials research*, vol. 41, pp. 433–448, 2011.

[16] H. E. Katz and T. O. Poehler, *Innovative thermoelectric materials: polymer, nanostructure and composite thermoelectrics*. World Scientific, 2016.

[17] N. W. Ashcroft and N. D. Mermin, "Solid state physics (saunders college, philadelphia, 1976)," *Appendix N*, vol. 166, 2010.

[18] T. C. Harman and J. M. Honig, "Thermoelectric and thermomagnetic effects and applications," *1967, 377 P. MCGRAW-HILL INC., NEW YORK, N. Y.$ 17. 50*, 1967.

[19] T. M. Tritt, *Thermal conductivity: theory, properties, and applications*. Springer Science & Business Media, 2005.

[20] G. A. Slack and S. Galginaitis, "Thermal conductivity and phonon scattering by magnetic impurities in cdte," *Physical Review*, vol. 133, no. 1A, p. A253, 1964.

[21] G. Mahan and J. O. Sofo, "The best thermoelectric," *Proceedings of the National Academy of Sciences*, vol. 93, no. 15, pp. 7436–7439, 1996.

[22] H. Wang, A. Charoenphakdee, K. Kurosaki, S. Yamanaka, and G. J. Snyder, "Reduction of thermal conductivity in pbte: Tl by alloying with tlsbt e 2," *Physical Review B*, vol. 83, no. 2, p. 024303, 2011.

[23] Q. Zhang, H. Wang, W. Liu, H. Wang, B. Yu, Q. Zhang, Z. Tian, G. Ni, S. Lee, K. Esfarjani, *et al.*, "Enhancement of thermoelectric figure-of-merit by resonant states of aluminium doping in lead selenide," *Energy & Environmental Science*, vol. 5, no. 1, pp. 5246–5251, 2012.

[24] Y. Pei, H. Wang, and G. J. Snyder, "Band engineering of thermoelectric materials," *Advanced materials*, vol. 24, no. 46, pp. 6125–6135, 2012.

[25] L.-D. Zhao, H. Wu, S. Hao, C.-I. Wu, X. Zhou, K. Biswas, J. He, T. P. Hogan, C. Uher, C. Wolverton, *et al.*, "All-scale hierarchical thermoelectrics: MgTe in PbTe facilitates valence band convergence and suppresses bipolar thermal transport for high performance," *Energy & Environmental Science*, vol. 6, no. 11, pp. 3346–3355, 2013.

[26] H. Wang, Z. M. Gibbs, Y. Takagiwa, and G. J. Snyder, "Tuning bands of PbSe for better thermoelectric efficiency," *Energy & Environmental Science*, vol. 7, no. 2, pp. 804–811, 2014.

[27] W. Liu, X. Tan, K. Yin, H. Liu, X. Tang, J. Shi, Q. Zhang, and C. Uher, "Convergence of conduction bands as a means of enhancing thermoelectric performance of n-type $Mg_2Si_{1-x}Sn_x$ solid solutions," *Physical review letters*, vol. 108, no. 16, p. 166601, 2012.

[28] A. F. Ioffe, "Semiconductor thermoelements and thermoelectric cooling," 1957.

[29] G. J. Snyder and E. S. Toberer, "Complex thermoelectric materials," in *materials for sustainable energy: a collection of peer-reviewed research and review articles from Nature Publishing Group*, pp. 101–110, World Scientific, 2011.

[30] H. Ehrenreich, *Advances in research and applications*. Elsevier, 1996.

[31] X. Zhou, P.-a. Zong, X. Chen, J. Tao, and H. Lin, "The structure of filled skutterudites and the local vibration behavior of the filling atom," *Physica B: Condensed Matter*, vol. 507, pp. 131–133, 2017.

[32] B. Sales, D. Mandrus, and R. K. Williams, "Filled skutterudite antimonides: a new class of thermoelectric materials," *Science*, vol. 272, no. 5266, pp. 1325–1328, 1996.

[33] X. Shi, J. Yang, J. R. Salvador, M. Chi, J. Y. Cho, H. Wang, S. Bai, J. Yang, W. Zhang,

and L. Chen, "Multiple-filled skutterudites: high thermoelectric figure of merit through separately optimizing electrical and thermal transports," *Journal of the American Chemical Society*, vol. 133, no. 20, pp. 7837–7846, 2011.

[34] D. M. Rowe, *CRC handbook of thermoelectrics*. CRC press, 2018.

[35] N. Wang, H. Chen, H. He, W. Norimatsu, M. Kusunoki, and K. Koumoto, "Enhanced thermoelectric performance of Nb-doped $SrTiO_3$ by nano-inclusion with low thermal conductivity," *Scientific reports*, vol. 3, p. 3449, 2013.

[36] J. R. Sootsman, D. Y. Chung, and M. G. Kanatzidis, "New and old concepts in thermoelectric materials," *Angewandte Chemie International Edition*, vol. 48, no. 46, pp. 8616–8639, 2009.

[37] G. Chen, M. Dresselhaus, G. Dresselhaus, J.-P. Fleurial, and T. Caillat, "Recent developments in thermoelectric materials," *International materials reviews*, vol. 48, no. 1, pp. 45–66, 2003.

[38] B. Poudel, Q. Hao, Y. Ma, Y. Lan, A. Minnich, B. Yu, X. Yan, D. Wang, A. Muto, D. Vashaee, *et al.*, "High-thermoelectric performance of nanostructured bismuth antimony telluride bulk alloys," *Science*, vol. 320, no. 5876, pp. 634–638, 2008.

[39] J. L. Blackburn, A. J. Ferguson, C. Cho, and J. C. Grunlan, "Carbon-nanotube-based thermoelectric materials and devices," *Advanced Materials*, vol. 30, no. 11, p. 1704386, 2018.

[40] Y. Pei, X. Shi, A. LaLonde, H. Wang, L. Chen, and G. J. Snyder, "Convergence of electronic bands for high performance bulk thermoelectrics," *Nature*, vol. 473, no. 7345, pp. 66–69, 2011.

[41] Z. Chen, Z. Jian, W. Li, Y. Chang, B. Ge, R. Hanus, J. Yang, Y. Chen, M. Huang, G. J. Snyder, *et al.*, "Lattice dislocations enhancing thermoelectric PbTe in addition to band convergence," *Advanced materials*, vol. 29, no. 23, p. 1606768, 2017.

[42] K. Biswas, J. He, I. D. Blum, C.-I. Wu, T. P. Hogan, D. N. Seidman, V. P. Dravid, and M. G. Kanatzidis, "High-performance bulk thermoelectrics with all-scale hierarchical architectures," *Nature*, vol. 489, no. 7416, pp. 414–418, 2012.

[43] G. Dennler, R. Chmielowski, S. Jacob, F. Capet, P. Roussel, S. Zastrow, K. Nielsch, I. Opahle, and G. K. Madsen, "Are binary copper sulfides/selenides really new and promising thermoelectric materials?," *Advanced Energy Materials*, vol. 4, no. 9, p. 1301581, 2014.

[44] P. Qiu, X. Shi, and L. Chen, "Thermoelectric properties of $Cu_{2-\delta}X$ (X= S, Se, and Te)," in *Materials Aspect of Thermoelectricity*, pp. 303–330, CRC Press, 2016.

[45] E. J. Skoug, J. D. Cain, and D. T. Morelli, "High thermoelectric figure of merit in the Cu_3SbSe_4-Cu_3SbS_4 solid solution," *Applied Physics Letters*, vol. 98, no. 26, p. 261911, 2011.

[46] J. Fan, W. Carrillo-Cabrera, L. Akselrud, I. Antonyshyn, L. Chen, and Y. Grin, "New monoclinic phase at the composition Cu_2SnSe_3 and its thermoelectric properties," *Inorganic chemistry*, vol. 52, no. 19, pp. 11067–11074, 2013.

[47] E. J. Skoug, J. D. Cain, and D. T. Morelli, "Thermoelectric properties of the Cu_2SnSe_3–Cu_2GeSe_3 solid solution," *Journal of alloys and compounds*, vol. 506, no. 1, pp. 18–21, 2010.

[48] R. Amatya and R. Ram, "Trend for thermoelectric materials and their earth abundance," *Journal of electronic materials*, vol. 41, no. 6, pp. 1011–1019, 2012.

[49] J. Majzlan, S. Kiefer, J. Herrmann, M. Števko, J. Sejkora, M. Chovan, T. Lánczos, M. Lazarov, A. Gerdes, F. Langenhorst, *et al.*, "Synergies in elemental mobility during weathering of tetrahedrite [(Cu,Fe,Zn)12 $(Sb,As)_4S_{13}$]: Field observations, electron microscopy, isotopes of cu, c, o, radiometric dating, and water geochemistry," *Chemical Geology*, vol. 488, pp. 1–20, 2018.

[50] S. Kasap and P. Capper, *Springer handbook of electronic and photonic materials*. Springer, 2017.

[51] R. Chetty, A. Bali, and R. C. Mallik, "Tetrahedrites as thermoelectric materials: an overview," *Journal of Materials Chemistry C*, vol. 3, no. 48, pp. 12364–12378, 2015.

[52] E. Makovicky and S. Karup-Møller, "Exploratory studies on substitution of minor elements in synthetic tetrahedrite part I. subst. by Fe, Zu, Co, Ni, Mn, Cr, V, and Pb. unit-cell param-

eter changes on subst. & the struct. role of Cu* O2* O+," *Neues Jahrbuch Fur Mineralogie-Abhandlungen*, vol. 167, no. 1, pp. 89–123, 1994.

[53] P. Levinsky, C. Candolfi, A. Dauscher, B. Lenoir, and J. Hejtmanek, "Thermoelectric properties of magnesium-doped tetrahedrite $Cu_{12-x}Mg_xSb4\,S13$," *Journal of Electronic Materials*, vol. 48, no. 4, pp. 1926–1931, 2019.

[54] D. P. Kumar, R. Chetty, O. Femi, K. Chattopadhyay, P. Malar, and R. Mallik, "Thermoelectric properties of bi doped tetrahedrite," *Journal of Electronic Materials*, vol. 46, no. 5, pp. 2616–2622, 2017.

[55] A. G. Trudu and U. Knittel, "Crystallography, mineral chemistry and chemical nomenclature of goldfieldite, the tellurian member of the tetrahedrite solid-solution series," *The Canadian Mineralogist*, vol. 36, no. 4, pp. 1115–1137, 1998.

[56] N. E. Johnson, J. R. Craig, and J. D. Rimstidt, "Compositional trends in tetrahedrite," *The Canadian Mineralogist*, vol. 24, no. 2, pp. 385–397, 1986.

[57] A. P. Gonçalves, E. B. Lopes, M. F. Montemor, J. Monnier, and B. Lenoir, "Oxidation studies of $Cu_{12}Sb_{3.9}Bi_{0.1}S_{10}Se3$ tetrahedrite," *Journal of Electronic Materials*, vol. 47, no. 5, pp. 2880–2889, 2018.

[58] H. Yang, M.-C. Record, Z. Aliev, and P. Boulet, "Stability investigation of se-and te-substituted tetrahedrite," *Journal of Electronic Materials*, pp. 1–11, 2020.

[59] B. J. Wuensch, "The crystal structure of tetrahedrite, $Cu_{12}Sb_4S_{18}$," *Zeitschrift für Kristallographie-Crystalline Materials*, vol. 119, no. 1-6, pp. 437–453, 1964.

[60] G. A. Slack, "New materials and performance limits for thermoelectric cooling," *CRC handbook of thermoelectrics*, pp. 407–440, 1995.

[61] D. G. Cahill and R. O. Pohl, "Thermal conductivity of amorphous solids above the plateau," *Physical review B*, vol. 35, no. 8, p. 4067, 1987.

[62] D. G. Cahill and R. O. Pohl, "Lattice vibrations and heat transport in crystals and glasses," *Annual review of physical chemistry*, vol. 39, no. 1, pp. 93–121, 1988.

[63] C. Uher, *Materials aspect of thermoelectricity*. CRC press, 2016.

[64] A. Pfitzner, M. Evain, and V. Petricek, "$Cu_{12}Sb_4S_{13}$: A temperature-dependent structure investigation," *Acta Crystallographica Section B: Structural Science*, vol. 53, no. 3, pp. 337–345, 1997.

[65] R. Chetty, P. K. DS, G. Rogl, P. Rogl, E. Bauer, H. Michor, S. Suwas, S. Puchegger, G. Giester, and R. C. Mallik, "Thermoelectric properties of a Mn substituted synthetic tetrahedrite," *Physical Chemistry Chemical Physics*, vol. 17, no. 3, pp. 1716–1727, 2015.

[66] E. Lara-Curzio, A. F. May, O. Delaire, M. A. McGuire, X. Lu, C.-Y. Liu, E. D. Case, and D. T. Morelli, "Low-temperature heat capacity and localized vibrational modes in natural and synthetic tetrahedrites," *Journal of Applied Physics*, vol. 115, no. 19, p. 193515, 2014.

[67] K. Suekuni, C. H. Lee, H. I. Tanaka, E. Nishibori, A. Nakamura, H. Kasai, H. Mori, H. Usui, M. Ochi, T. Hasegawa, *et al.*, "Retreat from stress: Rattling in a planar coordination," *Advanced Materials*, vol. 30, no. 13, p. 1706230, 2018.

[68] J. Li, M. Zhu, D. L. Abernathy, X. Ke, D. T. Morelli, and W. Lai, "First-principles studies of atomic dynamics in tetrahedrite thermoelectrics," *APL Materials*, vol. 4, no. 10, p. 104811, 2016.

[69] D. Braun and W. Jeitschko, "Preparation and structural investigations of antimonides with the $LaFe_4P_{12}$ structure," *Journal of the Less Common Metals*, vol. 72, no. 1, pp. 147–156, 1980.

[70] A. Abou El Ela and N. Abdelmohsen, "Electrical properties of AgTiSe2 semiconductor in the liquid state," *Acta Physica Academiae Scientiarum Hungaricae*, vol. 52, no. 2, pp. 123–128, 1982.

[71] D. Morelli, V. Jovovic, and J. Heremans, "Intrinsically minimal thermal conductivity in cubic $I-V-VI_2$ semiconductors," *Physical review letters*, vol. 101, no. 3, p. 035901, 2008.

[72] E. J. Skoug and D. T. Morelli, "Role of lone-pair electrons in producing minimum thermal conductivity in nitrogen-group chalcogenide compounds," *Physical review letters*, vol. 107, no. 23, p. 235901, 2011.

[73] X. Lu and D. T. Morelli, "Tetrahedrites: earth-abundant thermoelectric materials with in-

trinsically low thermal conductivity," in *Materials aspect of thermoelectricity*, pp. 487–502, CRC Press, 2016.

[74] G. A. Slack, "The thermal conductivity of nonmetallic crystals," in *Solid state physics*, vol. 34, pp. 1–71, Elsevier, 1979.

[75] S. Ganesan, "Temperature variation of the grüneisen parameter in magnesium oxide," *Philosophical Magazine*, vol. 7, no. 74, pp. 197–205, 1962.

[76] C. Dun, N. Holzwarth, Y. Li, W. Huang, and D. L. Carroll, "$Cu_2ZnSnS_xO_{4-x}$ and $Cu_2ZnSnS_xSe_{4-x}$: First principles simulations of optimal alloy configurations and their energies," *Journal of Applied Physics*, vol. 115, no. 19, p. 193513, 2014.

[77] X. Fan, E. D. Case, X. Lu, and D. T. Morelli, "Room temperature mechanical properties of natural-mineral-based thermoelectrics," *Journal of materials science*, vol. 48, no. 21, pp. 7540–7550, 2013.

[78] F. Zhou, W. Nielson, Y. Xia, V. Ozoliņš, *et al.*, "Lattice anharmonicity and thermal conductivity from compressive sensing of first-principles calculations," *Physical review letters*, vol. 113, no. 18, p. 185501, 2014.

[79] D. I. Nasonova, V. Y. Verchenko, A. A. Tsirlin, and A. V. Shevelkov, "Low-temperature structure and thermoelectric properties of pristine synthetic tetrahedrite $Cu_{12}Sb_4S_{13}$," *Chemistry of Materials*, vol. 28, no. 18, pp. 6621–6627, 2016.

[80] T. Suzuki, H. Goto, I. Ishii, Y. Noguchi, S. Kamikawa, K. Suekuni, H. I. Tanaka, and T. Takabatake, "Elastic softening in the tetrahedrite $Cu_{12}Sb_4S_{13}$," *Physics Procedia*, vol. 75, pp. 443–446, 2015.

[81] H. I. Tanaka, K. Suekuni, K. Umeo, T. Nagasaki, H. Sato, G. Kutluk, E. Nishibori, H. Kasai, and T. Takabatake, "Metal–Semiconductor Transition Concomitant with a Structural Transformation in Tetrahedrite $Cu_{12}Sb_4S_{13}$," *Journal of the Physical Society of Japan*, vol. 85, no. 1, p. 014703, 2016.

[82] S. O. Long, A. V. Powell, S. Hull, F. Orlandi, C. C. Tang, A. R. Supka, M. Fornari, and P. Vaqueiro, "Jahn–Teller Driven Electronic Instability in Thermoelectric Tetrahedrite," *Ad-*

vanced Functional Materials, 2020.

[83] M. L. Johnson and R. Jeanloz, "A brillouin-zone model for compositional variation in tetrahedrite," *American Mineralogist*, vol. 68, no. 1-2, pp. 220–226, 1983.

[84] R. Pattrick, G. Van Der Laan, D. Vaughan, and C. Henderson, "Oxidation state and electronic configuration determination of copper in tetrahedrite group minerals by L-edge X-ray absorption spectroscopy," *Physics and Chemistry of Minerals*, vol. 20, no. 6, pp. 395–401, 1993.

[85] F. Di Benedetto, G. Bernardini, C. Cipriani, C. Emiliani, D. Gatteschi, and M. Romanelli, "The distribution of Cu (II) and the magnetic properties of the synthetic analogue of tetrahedrite: $Cu_{12}Sb_4S_{13}$," *Physics and chemistry of minerals*, vol. 32, no. 3, pp. 155–164, 2005.

[86] E. Makovicky and B. J. Skinner, "Studies of the sulfosalts of copper; VII, Crystal structures of the exsolution products $Cu_{12.3}Sb_4S_{13}$ and $Cu_{13.8}Sb_4S_{13}$ of unsubstituted synthetic tetrahedrite," *The Canadian Mineralogist*, vol. 17, no. 3, pp. 619–634, 1979.

[87] N. Mozgova, V. Mikučionis, V. Valiukenas, A. Tsepin, and A. Orliukas, "Some electrical properties of fahlore $Cu_{10}(Zn,Fe)_2(As,Sb)_4S_{13}$," *Physics and Chemistry of Minerals*, vol. 15, no. 2, pp. 171–172, 1987.

[88] S. Tippireddy, R. Chetty, M. H. Naik, M. Jain, K. Chattopadhyay, and R. C. Mallik, "Electronic and thermoelectric properties of transition metal substituted tetrahedrites," *The Journal of Physical Chemistry C*, vol. 122, no. 16, pp. 8735–8749, 2018.

[89] J. Heo, R. Ravichandran, C. F. Reidy, J. Tate, J. F. Wager, and D. A. Keszler, "Design meets nature: tetrahedrite solar absorbers," *Advanced Energy Materials*, vol. 5, no. 7, p. 1401506, 2015.

[90] J. Heo, G. Laurita, S. Muir, M. A. Subramanian, and D. A. Keszler, "Enhanced thermoelectric performance of synthetic tetrahedrites," *Chemistry of Materials*, vol. 26, no. 6, pp. 2047–2051, 2014.

[91] K. Suekuni, Y. Tomizawa, T. Ozaki, and M. Koyano, "Systematic study of electronic and magnetic properties for $Cu_{12-x}TM_xSb_4S_{13}$ (TM = Mn, Fe, Co, Ni, and Zn) tetrahedrite,"

Journal of Applied Physics, vol. 115, no. 14, p. 143702, 2014.

[92] D. P. Kumar, R. Chetty, P. Rogl, G. Rogl, E. Bauer, P. Malar, and R. C. Mallik, "Thermoelectric properties of Cd doped tetrahedrite: $Cu_{12-x}Cd_xSb_4S_{13}$," *Intermetallics*, vol. 78, pp. 21–29, 2016.

[93] Y. Bouyrie, C. Candolfi, J.-B. Vaney, A. Dauscher, and B. Lenoir, "High Temperature Transport Properties of Tetrahedrite $Cu_{12-x}M_xSb_{4-y}Te_yS13$ (M= Zn, Ni) Compounds," *Journal of Electronic Materials*, vol. 45, no. 3, pp. 1601–1605, 2016.

[94] T. Barbier, S. Rollin-Martinet, P. Lemoine, F. Gascoin, A. Kaltzoglou, P. Vaqueiro, A. V. Powell, and E. Guilmeau, "Thermoelectric Materials: A New Rapid Synthesis Process for Nontoxic and High-Performance Tetrahedrite Compounds," *Journal of the American Ceramic Society*, vol. 99, no. 1, pp. 51–56, 2016.

[95] Y. Bouyrie, S. Sassi, C. Candolfi, J.-B. Vaney, A. Dauscher, and B. Lenoir, "Thermoelectric properties of double-substituted tetrahedrites $Cu_{12-x}Co_xSb_{4-y}Te_yS13$," *Dalton Transactions*, vol. 45, no. 17, pp. 7294–7302, 2016.

[96] K. Suekuni, K. Tsuruta, M. Kunii, H. Nishiate, E. Nishibori, S. Maki, M. Ohta, A. Yamamoto, and M. Koyano, "High-performance thermoelectric mineral $Cu_{12-x}Ni_xSb_4S_{13}$ tetrahedrite," *Journal of Applied Physics*, vol. 113, no. 4, p. 043712, 2013.

[97] A. P. Gonçalves, E. B. Lopes, B. Villeroy, J. Monnier, C. Godart, and B. Lenoir, "Effect of Ni, Bi and Se on the tetrahedrite formation," *RSC advances*, vol. 6, no. 104, pp. 102359–102367, 2016.

[98] D. I. Nasonova, I. A. Presniakov, A. V. Sobolev, V. Y. Verchenko, A. A. Tsirlin, Z. Wei, E. V. Dikarev, and A. V. Shevelkov, "Role of iron in synthetic tetrahedrites revisited," *Journal of Solid State Chemistry*, vol. 242, pp. 62–69, 2016.

[99] A. Güler, C. Boyraz, D. Shulgin, G. Mozzhukhin, and B. Rameev, "Synthesis & characterization of tetrahedrite compounds for thermoelectric applications," in *2016 9th International Kharkiv Symposium on Physics and Engineering of Microwaves, Millimeter and Submillimeter Waves (MSMW)*, pp. 1–4, IEEE, 2016.

[100] A. Guler, S. Ballikaya, C. Boyraz, C. Okay, D. Shulgin, and B. Rameev, "Thermoelectric properties and EPR analysis of Fe doped $Cu_{12}Sb_4S_{13}$," *Journal of Solid State Chemistry*, vol. 269, pp. 547–552, 2019.

[101] S.-Y. Kim, J.-H. Pi, G.-E. Lee, and I.-H. Kim, "Synthesis of Fe-Doped Tetrahedrites $Cu_{12-x}Fe_xSb_4S_{13}$ and Characterization of Their Thermoelectric Properties,"

[102] X. Lu, D. T. Morelli, Y. Xia, and V. Ozolins, "Increasing the thermoelectric figure of merit of tetrahedrites by co-doping with nickel and zinc," *Chemistry of Materials*, vol. 27, no. 2, pp. 408–413, 2015.

[103] T. Barbier, P. Lemoine, S. Gascoin, O. I. Lebedev, A. Kaltzoglou, P. Vaqueiro, A. V. Powell, R. I. Smith, and E. Guilmeau, "Structural stability of the synthetic thermoelectric ternary and nickel-substituted tetrahedrite phases," *Journal of Alloys and Compounds*, vol. 634, pp. 253–262, 2015.

[104] S. Harish, D. Sivaprahasam, M. Battabyal, and R. Gopalan, "Phase stability and thermoelectric properties of $Cu_{10.5}Zn_{1.5}Sb_4S_{13}$ tetrahedrite," *Journal of Alloys and Compounds*, vol. 667, pp. 323–328, 2016.

[105] K. Tatsuka *et al.*, "Composition variation and polymorphism of tetrahedrite in the Cu-Sb-S system below 400°C," 1973.

[106] F. Di Benedetto, G. P. Bernardini, D. Borrini, C. Emiliani, C. Cipriani, C. Danti, A. Caneschi, D. Gatteschi, and M. Romanelli, "Crystal chemistry of tetrahedrite solid-solution: EPR and magnetic investigations," *The Canadian Mineralogist*, vol. 40, no. 3, pp. 837–847, 2002.

[107] R. Seal, E. J. Essene, and W. C. Kelly, "Tetrahedrite and tennantite; evaluation of thermodynamic data and phase equilibria," *The Canadian Mineralogist*, vol. 28, no. 4, pp. 725–738, 1990.

[108] Y. Kosaka, K. Suekuni, K. Hashikuni, Y. Bouyrie, M. Ohta, and T. Takabatake, "Effects of Ge and Sn substitution on the metal–semiconductor transition and thermoelectric properties of $Cu_{12}Sb_4S_{13}$ tetrahedrite," *Physical Chemistry Chemical Physics*, vol. 19, no. 13, pp. 8874–

8879, 2017.

[109] R. A. Pattrick and A. Hall, "Silver substitution into synthetic zinc, cadmium, and iron tetrahedrites," *Mineralogical Magazine*, vol. 47, no. 345, pp. 441–451, 1983.

[110] L. Huang, Y. Wang, C. Zhu, R. Xu, J. Li, J. Zhang, D. Li, Z. Wang, L. Wang, C. Song, *et al.*, "Preparation and enhanced thermoelectric performance of Pb-doped tetrahedrite $Cu_{12-x}Pb_xSb_4S_{13}$," *Journal of Alloys and Compounds*, vol. 769, pp. 478–483, 2018.

[111] X. Lu and D. Morelli, "The effect of Te substitution for Sb on thermoelectric properties of tetrahedrite," *Journal of electronic materials*, vol. 43, no. 6, pp. 1983–1987, 2014.

[112] Y. Bouyrie, C. Candolfi, S. Pailhes, M. Koza, B. Malaman, A. Dauscher, J. Tobola, O. Boisron, L. Saviot, and B. Lenoir, "From crystal to glass-like thermal conductivity in crystalline minerals," *Physical Chemistry Chemical Physics*, vol. 17, no. 30, pp. 19751–19758, 2015.

[113] Y. Bouyrie, C. Candolfi, V. Ohorodniichuk, B. Malaman, A. Dauscher, J. Tobola, and B. Lenoir, "Crystal structure, electronic band structure and high-temperature thermoelectric properties of Te-substituted tetrahedrites $Cu_{12}Sb_{4-x}Te_xS_{13}$ $(0.5 \leq x \leq 2.0)$," *Journal of Materials Chemistry C*, vol. 3, no. 40, pp. 10476–10487, 2015.

[114] Y. Bouyrie, C. Candolfi, A. Dauscher, B. Malaman, and B. Lenoir, "Exsolution Process as a Route toward Extremely Low Thermal Conductivity in $Cu_{12}Sb_{4-x}Te_xS_{13}$ Tetrahedrites," *Chemistry of Materials*, vol. 27, no. 24, pp. 8354–8361, 2015.

[115] B. Wuensch, Y. Takeuchi, and W. Nowacki, "Refinement of the crystal structure of binnite, $Cu_{12}As_4S_{13}$," *Zeitschrift für Kristallographie-Crystalline Materials*, vol. 123, no. 1-6, pp. 1–20, 1966.

[116] E. Makovicky, L. Karanović, D. Poleti, T. Balić-Žunić, and W. H. Paar, "Crystal structure of copper-rich unsubstituted tennantite, $Cu_{12.5}As_4S_{13}$," *The Canadian Mineralogist*, vol. 43, no. 2, pp. 679–688, 2005.

[117] S. Karup-Møller and E. Makovicky, "Exploratory studies of element substitutions in synthetic tetrahedrite. Part II. Selenium and tellurium as anions in Zn-Fe tetrahedrites," *N. jb. miner. mh*, vol. 9, no. 9, pp. 385–399, 1999.

[118] Y. Zhang, V. Ozolins, D. Morelli, and C. Wolverton, "Prediction of new stable compounds and promising thermoelectrics in the Cu–Sb–Se system," *Chemistry of Materials*, vol. 26, no. 11, pp. 3427–3435, 2014.

[119] X. Lu, D. T. Morelli, Y. Wang, W. Lai, Y. Xia, and V. Ozolins, "Phase Stability, Crystal Structure, and Thermoelectric Properties of $Cu_{12}Sb_4S_{13-x}Se_x$ Solid Solutions," *Chemistry of Materials*, vol. 28, no. 6, pp. 1781–1786, 2016.

[120] Y. Yan, H. Wu, G. Wang, X. Lu, and X. Zhou, "High thermoelectric performance balanced by electrical and thermal transport in tetrahedrites $Cu_{12+x}Sb_4S_{12}Se$," *Energy Storage Materials*, vol. 13, pp. 127–133, 2018.

[121] J. Wang, M. Gu, Y. Bao, X. Li, and L. Chen, "Quick fabrication and thermoelectric properties of $Cu_{12}Sb_4S_{13}$ tetrahedrite," *Journal of Electronic Materials*, vol. 45, no. 4, pp. 2274–2277, 2016.

[122] A. Gonçalves, E. B. Lopes, J. Monnier, J. Bourgon, J. Vaney, A. Piarristeguy, A. Pradel, B. Lenoir, G. Delaizir, M. Pereira, *et al.*, "Fast and scalable preparation of tetrahedrite for thermoelectrics via glass crystallization," *Journal of Alloys and Compounds*, vol. 664, pp. 209–217, 2016.

[123] P. Levinsky, J.-B. Vaney, C. Candolfi, A. Dauscher, B. Lenoir, and J. Hejtmánek, "Electrical, Thermal, and Magnetic Characterization of Natural Tetrahedrites–Tennantites of Different Origin," *Journal of Electronic Materials*, vol. 45, no. 3, pp. 1351–1357, 2016.

[124] M. Telkes, "Thermoelectric power and electrical resistivity of minerals," *American Mineralogist: Journal of Earth and Planetary Materials*, vol. 35, no. 7-8, pp. 536–555, 1950.

[125] X. Lu and D. T. Morelli, "Natural mineral tetrahedrite as a direct source of thermoelectric materials," *Physical Chemistry Chemical Physics*, vol. 15, no. 16, pp. 5762–5766, 2013.

[126] U. Chalapathi, B. Poornaprakash, and S.-H. Park, "Growth and properties of Cu_3SbS_4 thin films prepared by a two-stage process for solar cell applications," *Ceramics International*, vol. 43, no. 6, pp. 5229–5235, 2017.

[127] B. Bradlyn, L. Elcoro, J. Cano, M. Vergniory, Z. Wang, C. Felser, M. Aroyo, and B. A.

Bernevig, "Topological quantum chemistry," *Nature*, vol. 547, no. 7663, pp. 298–305, 2017.

[128] A. Pfitzner and S. Reiser, "Refinement of the crystal structures of Cu_3PS_4 and Cu_3SbS_4 and a comment on normal tetrahedral structures," *Zeitschrift für Kristallographie-Crystalline Materials*, vol. 217, no. 2, pp. 51–54, 2002.

[129] W. Kohn and L. J. Sham, "Self-consistent equations including exchange and correlation effects," *Physical review*, vol. 140, no. 4A, p. A1133, 1965.

[130] J. P. Perdew, K. Burke, and M. Ernzerhof, "Generalized gradient approximation made simple," *Physical review letters*, vol. 77, no. 18, p. 3865, 1996.

[131] P. Hohenberg and W. Kohn, "Inhomogeneous electron gas," *Physical review*, vol. 136, no. 3B, p. B864, 1964.

[132] P. Blaha, K. Schwarz, F. Tran, R. Laskowski, G. K. Madsen, and L. D. Marks, "Wien2k: An APW + lo program for calculating the properties of solids," *The Journal of Chemical Physics*, vol. 152, no. 7, p. 074101, 2020.

[133] P. Novak, "Calculation of hyperfine field in WIEN2k," *energy*, vol. 2, p. 9, 2006.

[134] R. Laskowski and P. Blaha, "Calculating NMR chemical shifts using the augmented plane-wave method," *Physical Review B*, vol. 89, no. 1, p. 014402, 2014.

[135] K. Koch and S. Cottenier, "Analysis of an Electric-Field Gradient (EFG): the EFG-switch in LAPW2," 2011.

[136] G. C. Carter, L. H. Bennett, and D. Kahan, "Metallic shifts in NMR. A review of the theory and comprehensive critical data compilation of metallic materials. Part I. Review chapters NMR tables, evaluated knight shifts in metals together with other solid state and nuclear properties," tech. rep., National Standard Reference Data System, 1977.

[137] M. L. Buffon, G. Laurita, N. Verma, L. Lamontagne, L. Ghadbeigi, D. L. Lloyd, T. D. Sparks, T. M. Pollock, and R. Seshadri, "Enhancement of thermoelectric properties in the Nb–Co–Sn half-heusler/heusler system through spontaneous inclusion of a coherent second phase," *Journal of Applied Physics*, vol. 120, no. 7, p. 075104, 2016.

[138] N. Bloembergen and T. Rowland, "On the nuclear magnetic resonance in metals and alloys,"

Acta metallurgica, vol. 1, no. 6, pp. 731–746, 1953.

[139] C. P. Slichter, *Principles of magnetic resonance*, vol. 1. Springer Science & Business Media, 2013.

[140] B. H. Toby and R. B. Von Dreele, "*GSAS-II*: the genesis of a modern open-source all purpose crystallography software package," *Journal of Applied Crystallography*, vol. 46, pp. 544–549, Apr 2013.

[141] P. Vaqueiro, G. Guélou, A. Kaltzoglou, R. I. Smith, T. Barbier, E. Guilmeau, and A. V. Powell, "The Influence of Mobile Copper Ions on the Glass-Like Thermal Conductivity of Copper-Rich Tetrahedrites," *Chemistry of Materials*, vol. 29, no. 9, pp. 4080–4090, 2017.

[142] G. Carter, L. Bennett, and D. Kahan, "Metallic shifts in NMR," *Progress in Materials Science*, vol. 20, pp. 1 – 2, 1976.

[143] R. K. Harris and E. D. Becker, "NMR Nomenclature: Nuclear Spin Properties and Conventions for Chemical Shifts—IUPAC Recommendations," *Journal of Magnetic Resonance*, vol. 156, pp. 323–326, 2002.

[144] T. Kemp and M. Smith, "Quadfit—A New Cross-Platform Computer Program for Simulation of NMR Line Shapes from Solids with Distributions of Interaction Parameters," *Solid State Nuclear Magnetic Resonance*, vol. 35, pp. 243 – 252, 2009.

[145] T. Matsui, H. Matsuno, H. Kotegawa, H. Tou, K. Suekuni, T. Hasegawa, H. I. Tanaka, and T. Takabatake, "First-order metal–semiconductor transition triggered by rattling transition in tetrahedrite $Cu_{12}Sb_4S_{13}$: Cu-nuclear magnetic resonance studies," *Journal of the Physical Society of Japan*, vol. 88, no. 5, p. 054710, 2019.

[146] S. Kitagawa, T. Sekiya, S. Araki, T. C. Kobayashi, K. Ishida, T. Kambe, T. Kimura, N. Nishimoto, K. Kudo, and M. Nohara, "Suppression of nonmagnetic insulating state by application of pressure in mineral tetrahedrite $Cu_{12}Sb_4S_{13}$," *Journal of the Physical Society of Japan*, vol. 84, no. 9, p. 093701, 2015.

[147] K. E. Sakaie, C. P. Slichter, P. Lin, M. Jaime, and M. B. Salamon, "^{139}La Spectrum and Spin-Lattice Relaxation Measurements of $La_{2/3}Ca_{13}Mn_3$ in the Paramagnetic State," *Phys.*

Rev. B, vol. 59, pp. 9382–9391, Apr 1999.

[148] T. Bastow, J. Lehmann-Horn, and D. Miljak, "^{121,123}Sb and ^{75}As NMR and NQR investigation of the tetrahedrite ($Cu_{12}Sb_4S_{13}$)–tennantite ($Cu_{12}As_4S_{13}$) system and other metal arsenides," *Solid state nuclear magnetic resonance*, vol. 71, pp. 55–60, 2015.

[149] X. Lu, W. Yao, G. Wang, X. Zhou, D. Morelli, Y. Zhang, H. Chi, S. Hui, and C. Uher, "Band structure engineering in highly degenerate tetrahedrites through isovalent doping," *J. Mater. Chem. A*, vol. 4, pp. 17096–17103, 2016.

[150] T. Suzuki, H. Goto, I. Ishii, Y. Noguchi, S. Kamikawa, K. Suekuni, H. I. Tanaka, and T. Takabatake, "Elastic softening in the tetrahedrite $Cu_{12}Sb_4S_{13}$," *Physics Procedia*, vol. 75, pp. 443 – 446, 2015.

[151] W. Lai, Y. Wang, D. T. Morelli, and X. Lu, "From bonding asymmetry to anharmonic rattling in $Cu_{12}Sb_4S_{13}$ tetrahedrites: When lone-pair electrons are not so lonely," *Advanced Functional Materials*, vol. 25, pp. 3648–3657, 2015.

[152] Y. Wang, H. Lin, T. Das, M. Hasan, and A. Bansil, "Topological insulators in the quaternary chalcogenide compounds and ternary famatinite compounds," *New Journal of Physics*, vol. 13, no. 8, p. 085017, 2011.

[153] C. T. Crespo, "Microscopic optical absorption, analysis, and applications of famatinite cu3sbs4," *The Journal of Physical Chemistry C*, vol. 120, no. 15, pp. 7959–7965, 2016.

[154] K. Schwarz, P. Blaha, and G. Madsen, "Electronic structure calculations of solids using the wien2k package for material sciences," *Computer Physics Communications*, vol. 147, no. 1, pp. 71 – 76, 2002.

[155] W. Gou, Y. Li, J. Chi, J. H. Ross Jr., M. Beekman, and G. S. Nolas, "NMR Study of Slow Atomic Motion in $Sr_8Ga_{16}Ge_{30}$ Clathrate," *Phys. Rev. B*, vol. 71, p. 174307, May 2005.

[156] A. Abragam, *The Principles of Nuclear Magnetism*. Oxford science publications, 1961.

[157] B. S. Shastry and E. Abrahams, "What Does the Korringa Ratio Measure?," *Phys. Rev. Lett.*, vol. 72, pp. 1933–1936, Mar 1994.

[158] T. Dahm and K. Ueda, "NMR Relaxation and Resistivity from Rattling Phonons in Py-

rochlore Superconductors," *Phys. Rev. Lett.*, vol. 99, p. 187003, Oct 2007.

[159] B. H. Suits and C. P. Slichter, "Nuclear-quadrupole-resonance study of the 145-K charge-density-wave transition in $NbSe_3$," *Phys. Rev. B*, vol. 29, pp. 41–51, Jan 1984.

[160] X. Zheng, S. Y. Rodriguez, and J. H. Ross Jr., "NMR Relaxation and Rattling Phonons in the Type-I $Ba_8Ga_{16}Sn_{30}$ Clathrate," *Phys. Rev. B*, vol. 84, p. 024303, Jul 2011.

[161] S. Chin, S. Janecek, and E. Krotscheck, "An arbitrary order diffusion algorithm for solving schrödinger equations," *Computer Physics Communications*, vol. 180, no. 9, pp. 1700 – 1708, 2009.

[162] K. Suekuni, C. H. Lee, H. I. Tanaka, E. Nishibori, A. Nakamura, H. Kasai, H. Mori, H. Usui, M. Ochi, T. Hasegawa, M. Nakamura, S. Ohira-Kawamura, T. Kikuchi, K. Kaneko, H. Nishiate, K. Hashikuni, Y. Kosaka, K. Kuroki, and T. Takabatake, "Retreat from stress: Rattling in a planar coordination," *Advanced Materials*, vol. 30, p. 1706230, 2018.

[163] N. Ghassemi, Y. Tian, X. Lu, Y. Yan, X. Zhou, and J. H. Ross Jr, "Copper-Ion Dynamics and Phase Segregation in Cu-Rich Tetrahedrite: an NMR Study," *The Journal of Physical Chemistry C*, vol. 124, no. 7, pp. 3973–3979, 2020.

[164] P. Vaqueiro, G. Guelou, A. Kaltzoglou, R. I. Smith, T. Barbier, E. Guilmeau, and A. V. Powell, "The influence of mobile copper ions on the glass-like thermal conductivity of copper-rich tetrahedrites," *Chemistry of Materials*, vol. 29, no. 9, pp. 4080–4090, 2017.

[165] K. Tatsuka and N. Morimoto, "Tetrahedrite stability relations in the cu-sb-s system," *Economic Geology*, vol. 72, no. 2, pp. 258–270, 1977.

[166] K. Suekuni, K. Tsuruta, T. Ariga, and M. Koyano, "Thermoelectric properties of mineral tetrahedrites $Cu_{10}Tr_2Sb_4S_{13}$ with low thermal conductivity," *Applied Physics Express*, vol. 5, p. 051201, may 2012.

[167] Y. Yan, H. Wu, G. Wang, X. Lu, and X. Zhou, "High thermoelectric performance balanced by electrical and thermal transport in tetrahedrites $Cu_{12+x}Sb_4S_{12}Se$," *Energy Storage Materials*, vol. 13, pp. 127 – 133, 2018.

[168] M. K. Jana and K. Biswas, "Crystalline solids with intrinsically low lattice thermal conduc-

tivity for thermoelectric energy conversion," *ACS Energy Letters*, vol. 3, no. 6, pp. 1315–1324, 2018.

[169] S. Munjal and N. Khare, "Advances in resistive switching based memory devices," *Journal of Physics D: Applied Physics*, vol. 52, p. 433002, aug 2019.

[170] D. Brinkmann, "NMR studies of superionic conductors," *Progress in Nuclear Magnetic Resonance Spectroscopy*, vol. 24, no. 6, pp. 527–552, 1992.

[171] S. Hull, "Superionics: Crystal structures and conduction processes," *Reports on Progress in Physics*, vol. 67, no. 7, p. 1233, 2004.

[172] X.-P. Tang, U. Geyer, R. Busch, W. L. Johnson, and Y. Wu, "Diffusion mechanisms in metallic supercooled liquids and glasses," *Nature*, vol. 402, no. 6758, p. 160, 1999.

[173] B. H. Toby and R. B. Von Dreele, "Gsas-ii: the genesis of a modern open-source all purpose crystallography software package," *Journal of Applied Crystallography*, vol. 46, no. 2, pp. 544–549, 2013.

[174] J. Boyce, J. Mikkelsen, and B. Huberman, "Are the prefactor anomalies in superionic conductors due to 1-d effects?," *Solid State Communications*, vol. 29, no. 6, pp. 507 – 510, 1979.

[175] T. Eguchi, C. Marinos, J. Jonas, B. Silbernagel, and A. Thompson, "High pressure nmr study of the prefactor anomaly in the lithium intercalation compound $Li_{0.94}TiS_2$," *Solid State Communications*, vol. 38, no. 10, pp. 919 – 922, 1981.

[176] D. W. Bullett and W. G. Dawson, "Bonding relationships in some ternary and quarternary phosphide and tetrahedrite structures: $(Ag_6M_4P_{12})m_{6'}$, $Cu_{12+x}Sb_4S_{13}$ and $Cu_{14-x}Sb_4S_{13}$, $Ln_6Ni_6P_{17}$," *Journal of Physics C: Solid State Physics*, vol. 19, pp. 5837–5847, oct 1986.

[177] X.-M. Chen and T. C. Mak, "Metal-betaine interactions. part 17: A study of intradimer Cu··· Cu distance variation in copper (II) betaine complexes containing $[Cu_2(\text{carboxylato}-O,O')_4L_2]^{n+}$ species," *Structural Chemistry*, vol. 4, no. 4, pp. 247–259, 1993.

[178] P. K. Mehrotra and R. Hoffmann, "Copper (I)-copper (I) interactions. Bonding relationships

in d^{10}-d^{10} systems," *Inorganic Chemistry*, vol. 17, no. 8, pp. 2187–2189, 1978.

[179] A. A. Sirusi and J. H. Ross, "Chapter Three - Recent NMR Studies of Thermoelectric Materials," *Annual Reports on NMR Spectroscopy*, vol. 92, pp. 137 – 198, 2017.

[180] Y. Zha, V. Barzykin, and D. Pines, "Nmr and neutron-scattering experiments on the cuprate superconductors: A critical re-examination," *Phys. Rev. B*, vol. 54, pp. 7561–7574, Sep 1996.

[181] Y. Wang, W. D. Richards, S. P. Ong, L. J. Miara, J. C. Kim, Y. Mo, and G. Ceder, "Design principles for solid-state lithium superionic conductors," *Nature materials*, vol. 14, no. 10, p. 1026, 2015.

[182] A. A. Sirusi, S. Ballikaya, C. Uher, and J. H. Ross Jr., "Low-Temperature Structure and Dynamics in Cu_2Se," *J. Phys. Chem. C*, vol. 119, pp. 20293–20298, sep 2015.

[183] A. A. Sirusi, S. Ballikaya, J.-H. Chen, C. Uher, and J. H. Ross Jr, "Band Ordering and Dynamics of $Cu_{2-x}Te$ and $Cu_{1.98}Ag_{0.2}Te$," *The Journal of Physical Chemistry C*, vol. 120, no. 27, pp. 14549–14555, 2016.

[184] J. P. Yesinowski, H. D. Ladouceur, A. P. Purdy, and J. B. Miller, "Electrical and ionic conductivity effects on magic-angle spinning nuclear magnetic resonance parameters of CuI," *The Journal of chemical physics*, vol. 133, no. 23, p. 234509, 2010.

[185] T. Matsui, H. Matsuno, H. Kotegawa, H. Tou, K. Suekuni, T. Hasegawa, H. I. Tanaka, and T. Takabatake, "Precursor of Metal–Semiconductor Transition in Tetrahedrite Probed by Cu-NMR," in *Proceedings of the International Conference on Strongly Correlated Electron Systems (SCES2019)*, p. 011075, 2020.

[186] C. S. Lue, J. H. Ross Jr., K. D. D. Rathnayaka, D. G. Naugle, S. Y. Wu, and W.-H. Li, "Superparamagnetism and magnetic defects in Fe_2VAl and Fe_2VGa," *Journal of Physics: Condensed Matter*, vol. 13, p. 1585, 2001.

[187] D. I. Nasonova, V. Y. Verchenko, A. A. Tsirlin, and A. V. Shevelkov, "Low-Temperature Structure and Thermoelectric Properties of Pristine Synthetic Tetrahedrite $Cu_{12}Sb_4S_{13}$," *Chemistry of Materials*, vol. 28, pp. 6621–6627, 2016.

[188] R. Walstedt and L. Walker, "Nuclear-resonance line shapes due to magnetic impurities in metals," *Physical Review B*, vol. 9, no. 11, p. 4857, 1974.

[189] J. Chi, Y. Li, F. Vagizov, V. Goruganti, and J. H. Ross Jr, "NMR and Mössbauer study of spin-glass behavior in $FeAl_2$," *Physical Review B*, vol. 71, no. 2, p. 024431, 2005.

[190] S. Battiston, C. Fanciulli, S. Fiameni, A. Famengo, S. Fasolin, and M. Fabrizio, "One step synthesis and sintering of Ni and Zn substituted tetrahedrite as thermoelectric material," *Journal of Alloys and Compounds*, vol. 702, pp. 75–83, 2017.

[191] D. Weller, G. Kunkel, A. Ochs, D. Morelli, and M. E. Anderson, "Observation of n-type behavior in Fe-doped tetrahedrite at low temperature," *Materials Today Physics*, vol. 7, pp. 1–6, 2018.

APPENDIX A

RLC CIRCUIT SET UP

To perform the the NMR spectroscopy for various frequencies, I needed to change the calibrate the RLC circuit in order to attain the desired resonant frequency. This required the following equations for NMR coil sample holder based on an impedance matching principle. I figure (A.1)

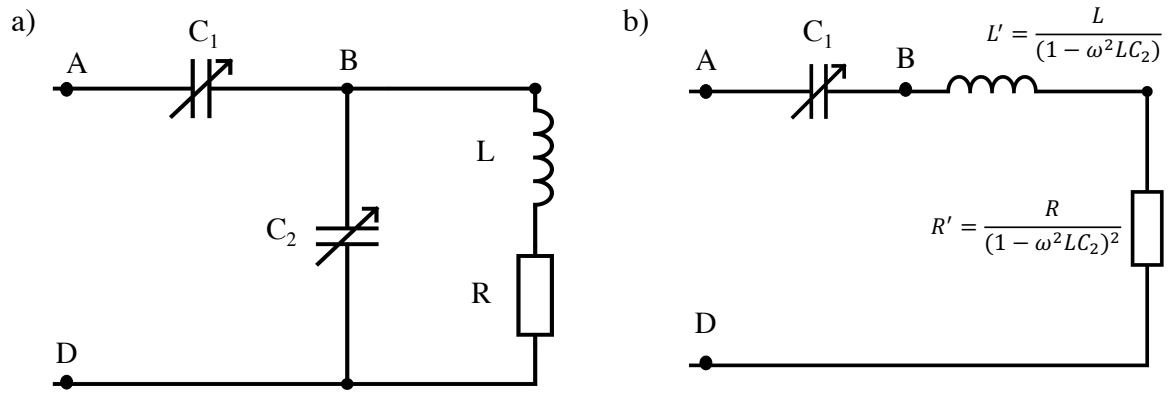

Figure A.1: a) The NMR probe's circuit. b) The corresponding circuit of impedance matching of the after ignoring the small contributions.

$$\begin{aligned} Z_{AD} &= Z_{BD} + \frac{1}{i\omega C_1} = \frac{1}{i\omega C_2 + 1/(R + i\omega L)} + \frac{1}{i\omega C_1} \\ &= \frac{R}{(1-\omega^2 LC_2)^2 + (RC_2\omega)^2} + i\omega \frac{L(1 - LC_2\omega^2) - R^2 C_2}{(1-\omega^2 LC_2)^2 + (RC_2\omega)^2} + \frac{1}{i\omega C_1}. \end{aligned} \quad \text{(A.1)}$$

On the other hand, $C_2 R^2$, $(RC_2\omega)^2 \ll 1$ and could be neglected, hence, equation (A.1) could be simplified to

$$Z_{AD} = \frac{R}{(1-\omega^2 LC_2)^2} + i\omega\frac{L}{(1-\omega^2 LC_2)} + \frac{1}{i\omega C_1}. \quad \text{(A.2)}$$

The corresponding equivalent circuit regarding to equation (A.2) is displayed in figure A.1, in which R' and L' are $\frac{R}{(1-\omega^2 LC_2)^2}$ and $\frac{L}{(1-\omega^2 LC_2)}$, respectively.

In order to fulfill the impedance matching requirement, R' should be set to 50 Ω, which is the characteristic impedance of the connecting coaxial cable. In addition, by tuning C_2 at a specified frequency

$$R' = \frac{R}{(1-\omega^2 LC_2)^2} = 50\Omega$$
$$C_2 = \frac{1-\sqrt{R/50}}{\omega^2 L}. \quad \text{(A.3)}$$

To acquire series resonance in figure (A.1.b)), C_1 should be set according to the following

$$C_1 = \frac{1-\omega^2 LC_2}{L\omega^2} = \frac{\sqrt{R/50}}{L\omega^2} \quad \text{(A.4)}$$

From equations (A.3) and (A.4), we can find the following quantities

$$\frac{\sqrt{R/50}}{C_1} = \frac{1-\sqrt{R/50}}{C_2}$$
$$R = \frac{50\Omega}{(1+C_2/C_1)^2} \quad \text{(A.5)}$$
$$L = \frac{1-\sqrt{R/50}}{C_2\omega^2} \quad \text{(A.6)}$$

L could also be expressed based on C_1 as

$$L = \frac{\sqrt{R/50}}{C_1\omega^2} \tag{A.7}$$

and finally the effective Q value of the coil could be expressed as

$$Q = \frac{\omega L}{R}. \tag{A.8}$$

By combining equations (A.5) and (A.8), the Q value can be expressed based on C_1, C_2, and ω as

$$Q = \frac{1 + C_2/C_1}{50C_1\omega}. \tag{A.9}$$

In our probe in the lab, C_1 and C_2 varied from 1 to 10 pF. When the impedance matching condition satisfied, we were able to acquire L and R of the coil by estimating the values of C_1 and C_2, and consequently, Q value was obtained.